Journal of
Materials Chemistry A

ROYAL SOCIETY
OF CHEMISTRY

REVIEW

View Article Online
View Journal

Cite this: DOI: 10.1039/d0ta12465f

Recent advances in photocatalytic degradation of plastics and plastic-derived chemicals

Zenglin Ouyang,†[a] Yang Yang,†[a] Chen Zhang,*[a] Shumin Zhu,*[b] Lei Qin,[a] Wenjun Wang,[a] Donghui He,[a] Yin Zhou,[a] Hanzhuo Luo[a] and Fanzhi Qin[a]

Plastic products, used in almost all aspects of daily life because of their low cost, durability, and portability, can be broken down into micro- and nano-scale plastics, thereby increasing the risk of human ingestion. Common plastic additives (polybrominated diphenyl ethers, nonylphenols, phthalic acid esters, *etc.*) will continue to be released into the environment during the aging and decomposition process, leading to an immeasurable and lasting negative impact on the environment. Recently, photocatalytic technology has been recognized as one of the promising proposals to degrade environmental organic pollutants, including plastics and plastic-derived chemicals. However, there are no systematic reviews on the photocatalytic degradation of plastics and plastic-derived chemicals in the current literature. Herein, the photocatalytic degradation of plastic fragments and major plastic-derived chemicals, including phthalic acid ester plasticizers, nonylphenol antioxidants, bisphenol A plasticizer and brominated flame retardants, is systematically investigated. And we reviewed the process and mechanism of photocatalytic degradation of these pollutants. The outlook section, offering insights into the future directions and prospects of photocatalytic degradation of plastics and plastic-derived chemicals, will be highlighted with the aim of overcoming the present limitations by exploiting more efficient photocatalysts and exploring creative application methods.

Received 25th December 2020
Accepted 8th May 2021

DOI: 10.1039/d0ta12465f

rsc.li/materials-a

1 Introduction

With the rapid development of an industrial society, the use of plastic products is rising. The production of plastics reached almost 58 million tons in Europe in 2019, while global plastic production was close to 370 million tons. More than half of the plastics produced are made in Asia, and the proportion of plastics produced in China even reached 30%.[1,2] The global plastic production is expected to double in the next 20 years.[3] The mass production of plastic products and the short service

Zenglin Ouyang received his BS in environmental engineering from Jiangxi University of Science and Technology in 2018. He is currently a postgraduate student under the supervision of Chen Zhang at the College of Environmental Science and Engineering, Hunan University, China. His current research interests include fabrication of nanomaterials and their catalysis applications in energy and environment fields.

Yang Yang received his BS from Changsha University of Science & Technology in 2016. Currently, he is a PhD candidate under the supervision of Prof. Guangming Zeng in the College of Environmental Science and Engineering, Hunan University, China. His current research interests are mainly focused on the utilization of advanced oxidation processes for water treatment.

---

[a] College of Environmental Science and Engineering, Key Laboratory of Environmental Biology and Pollution Control, Hunan University, Ministry of Education, Changsha 410082, PR China. E-mail: zhangchen@hnu.edu.cn

[b] Key Laboratory of Building Safety and Energy Efficiency, Ministry of Education, Department of Water Engineering and Science, College of Civil Engineering, Hunan University, Changsha, 410082, PR China. E-mail: zshuminwater@163.com

† These authors contributed equally to this article.

life of many plastic products have caused serious environmental and management problems.[4,5] Only 6% to 26% of plastics are recycled; 21–42% of them end up in landfills; and others are discharged into the environment through a variety of pathways.[3] Plastics are semi-synthetic or synthetic organic polymeric materials, and are widely used in modern life.[2,6] Most of them are difficult to degrade and can exist in the environment for a century because of their corrosion resistance.[6,7] Nowadays, plastic pollution is recognized as an environmental burden; for example, microplastics (MPs) are ubiquitously distributed in the marine environment, accounting for approximately 92% of global marine plastic debris.[8] They are similar to persistent organic pollutants (POPs), and have become a kind of persistent pollutant. In the ocean, the plastic degradation cycle is very long, and it would be almost impossible to remove plastics from the ocean.[9] The components of waste plastics can also be transferred to agricultural products, animals, and eventually into the human body.[10] Nowadays, plastic debris can be found in various environmental compartments such as sediments,[11,12] soils,[13] air,[14] oceans[15] and remote areas such as the Arctic and Antarctic,[16,17] and mountain-tops.[18] The environmental consequences of plastic solid waste are visible in the ever-increasing levels of global plastic pollution both on land and in the oceans,[19–23] which implies that the entire planet is under the pressure of plastic-related environmental problems (Fig. 1).

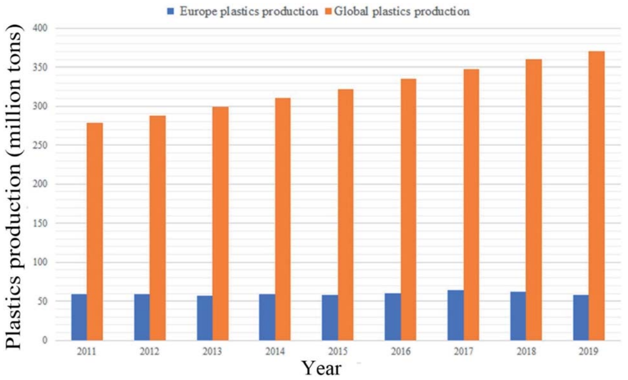

Fig. 1 Global and Europe plastic production data (data from Plastics Europe).

In addition to plastic itself, plastic-derived chemicals also pose a huge threat to the environment. Plastics are made by polymerizing various monomers and other substances such as phthalates (PAEs), bisphenol A (BPA), anti-ultraviolet radiation stabilizers, *etc.*[24] These substances endow plastics with many special physical properties such as rigidity, elasticity, UV stability and color.[25] However, many of them have been identified as being endocrine disruptors or toxic substances such as PAEs, BPA and polybrominated diphenyl ethers (PBDEs). Meanwhile, because the bonds between them and the polymer molecules are very weak, they are easily released from the plastic over time, leading to huge environmental risks.[25–27]

In view of the harmfulness of plastic waste, it is necessary to take effective measures to remove them from the environment. The existing methods for removal of MPs from water or wastewater include physical methods such as mechanical, thermal, and chemical methods such as catalytic, ozonation and photo-oxidative degradation. Relatively few studies advocate advanced technologies like bacterial oxidation and membrane bioreactors that could remove MPs from aqueous media, because they are usually expensive and time-consuming with high energy requirements. Fortunately, investigations have confirmed that photocatalytic technology is an efficient and viable way to degrade polymeric materials.[28,29] Compared with other methods, more efficient and precise transformations are allowed for photocatalytic technology.

Since 1972, when Fujishima and Honda found that a titanium dioxide (TiO_2) electrode irradiated with ultra-violet (UV) radiation could split H_2O into H_2 and O_2,[30] great attention has been paid to semiconductor photocatalysis and many achievements have been made in various fields including bacterial inactivation, reduction of heavy metal ions, and removal and degradation of organic pollutants in an air/aqueous phase.[31–38] Photocatalysis is an eco-friendly and sustainable technology for degrading organic pollutants, which can directly utilize solar energy and does not require exogenous electrical energy or chemical reagents.[39–43] When the photon energy irradiated on the semiconductor is higher than the band gap of the

Chen Zhang is currently an associate professor of Environmental Science and Engineering at Hunan University. He obtained his PhD in Environmental Engineering from Hunan University in 2017. The research interests of his group include fabrication of nanomaterials and their catalysis applications in energy and environment fields, and thermo-chemical conversion of biomass into clean energy and value-added chemicals.

Shumin Zhu is an assistant professor at the College of Civil Engineering at Hunan University, China. Dr Zhu obtained her PhD from the College of Environmental Science and Engineering at Tongji University in 2019. Her research focuses on UV based advanced oxidation processes, water disinfection and disinfection by-products. Her interests also include the kinetics and mechanisms of removal of organic micropollutants from water.

photocatalyst, the electrons (e^-) located in the valence band (VB) will be excited, transitioning from the top of the VB to the bottom of the conduction band (CB), leaving holes (h^+) on the VB, which causes electron–hole separation. The photogenerated carriers will then be transferred to the surface of the semiconductor for a series of reactions. In photocatalytic degradation of plastics and plastic-derived chemicals, the h^+ produced by photocatalysis can directly oxidize plastics, and some free radicals formed by the reaction of e^- and h^+ with O_2 or H_2O, such as hydroxyl and superoxide radicals, can also degrade plastics and plastic-derived chemicals.[29] For example, the main materials involved in the photocatalytic BPA degradation are photogenerated holes and hydroxyl radicals.[44] They are degraded into small molecules of organic matter or eventually into CO_2 and H_2O.

If photocatalytic technology can use plastic as a feedstock for energy production, it can realize both the degradation of plastics and the purpose of energy generation. Up to now, there has been almost no comprehensive review of photocatalytic degradation of plastics and plastic-derived chemicals. The purpose of our work is to (i) describe the size effects of macroplastics, MPs and nanoplastics (NPs) and the hazard analysis of the chemicals derived from plastics, (ii) give a detailed description of photocatalytic degradation of plastics and (iii) place emphasis on research into photocatalytic degradation of several kinds of plastic-derived chemical which are often detected in the environment, including PAEs, BPA, brominated flame retardants (BFRs) and nonylphenols (NP).[45] Finally, significant perspectives are proposed in view of the current challenges and opportunities in photocatalytic degradation of plastics and plastic-derived chemicals.

2 Plastics as persistent pollutants

Plastics are artificial long-chain polymeric materials, with additives added during the manufacturing processes. Considering the types of monomer in the polymer, plastics can be divided into many types including polyvinylchloride (PVC), polypropylene (PP), polyethylene terephthalate (PET), polyethylene (PE), polystyrene (PS), polybutylene terephthalate (PBT), polyurethane (PUR) and nylons. Those added additives include flame retardants, stabilizers, plasticizer, fillers and pigments, which can make the final products have good performance.[46] Plastic debris in the environment can be degraded to form small particles or fragments after sunlight irradiation, biodegradation and weathering. The plastic debris after degradation can be divided into macro-plastics (>25 mm), meso-plastics (5–25 mm), MPs (0.1–5 mm), and NPs (<100 nm).[3] And MPs can be divided into primary and secondary MPs on the basis of their origin: (i) primary MPs mainly originate from some personal care products,[47] and (ii) secondary MPs come from the macro-plastic cracking process which involves a combination of physical and chemical action including mechanical disintegration, oxidation, photodegradation and hydrolytic degradation.[48] MPs can be divided into granules, foams, fragments and fibers.[49] They are widespread in the marine environment and account for more than 90% of the global marine plastic waste.[50]

Most plastics are eventually discharged into the environment due to poor management or landfilled, and a few are recycled.[3,51] The life process of plastics in the environment can be seen in Fig. 2.

2.1 Macroplastics

Large plastics have caused severe pollution to the global coastlines, and freshwater and marine systems. This issue has attracted widespread attention since the 1990s.[52] The main impact of large plastics is biological entanglement and ingestion.

Entanglement mainly involves some plastic ropes and fishing nets.[53] Globally, approximately 6.4 million tons of fishing lines are intentionally or accidentally abandoned and lost in the ocean. They will follow the waves and continue to entangle marine organisms, which has a great negative impact on marine life.[54] Entanglement can cause great harm to organisms, such as blockage of the intestine, and organ damage caused by leaching toxins.[55,56] Besides, entanglement can also cause much physical harm to creatures, such as external wounds,[57] dermal wounds[58,59] and even death.[60–62]

In addition to entanglement, ingestion of plastic debris by marine organisms has attracted increasing attention. In 340 previous reports, at least 13 110 individual organisms from 208 species were affected by plastic ingestion.[53] Seabird species often ingest plastic by mistake, because they hardly regurgitate undigested hard material including plastics.[6] The earliest records of plastic-containing birds date back to 1962.[63] The foraging strategy usually causes incidents of plastics ingestion. For example, Day *et al.*[64] proposed that dipping and surface-seizing seabirds had a lower frequency of plastic uptake than pursuit-diving birds. The little auk could easily ingest plastics because it has difficulty in distinguishing small new plastic debris from zooplankton.[65] A recent review estimated that the amount of plastics consumed by green turtles increased significantly between 1985 and 2012.[66] Investigations have found that the plastics ingested by turtles are usually transparent or white; this may be because they mistake plastics for jellyfish.[67] Some plastics are similar in color to their prey and will catch the attention of hunters. Therefore, color is also an important factor leading to the ingestion of plastic by organisms. Parakeet auklets (*Aethia psittacula*) living on the coast of Alaska mainly consumed some dark plastic particles, which have a close resemblance to the light brown color crustaceans they forage.[68] Debris ingested by marine organisms may be digested or accumulated in the gastrointestinal tract, resulting in physical damage such as abrasion, obstruction and inflammation.[69,70] Although lethal effects are caused by ingestion, the lethal effects are less than in the case of entanglement.[9]

2.2 Microplastics and nanoplastics

Plastic debris in the environment can degrade to particles or small fragments after sunlight irradiation, biodegradation, and weathering. Small pieces of plastic can be classified into two

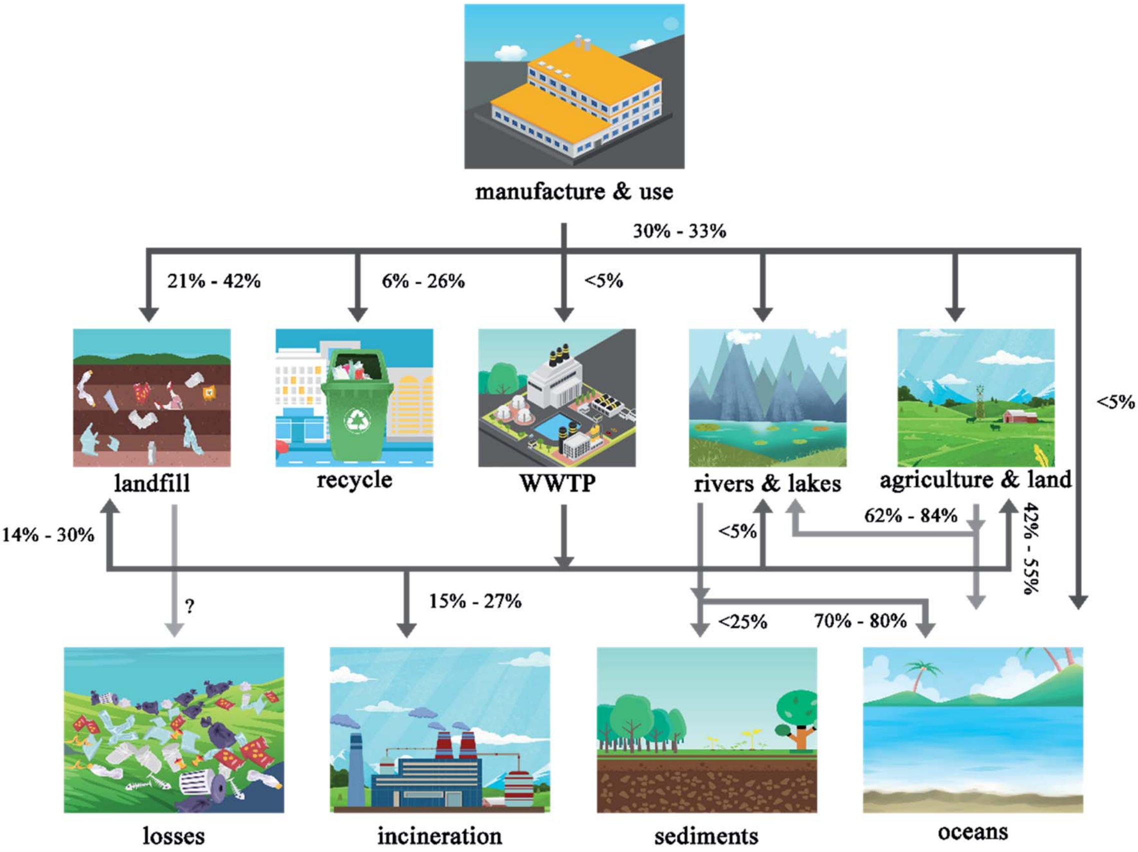

Fig. 2 Estimates of plastic loading and transport pathways in the environment. The different transparency arrows represent the direction of plastics moving from a given compartment to a subsequent compartment.

categories: MPs (<5 mm)[71,72] and NPs (<1000 nm).[73,74] In as early as the 1970s, it was reported that microscale plastic particles were detected in the environment.[75] Since MPs and NPs are widely distributed in the environment, the potential harm to living organisms has attracted more and more attention.

It is estimated that about 0.8–2.5 million tons of MPs enter the marine environment each year.[76] The use of sludge as an agricultural fertilizer has considerable economic advantages, so it has been promoted in some developed regions. In North America and Europe, half of the sludge is used for agricultural production, and about 0.044–0.3 million tons and 0.063–0.43 million tons of MPs in sludge are put into farmlands in North America and Europe, respectively, every year.[77] About 0.25 million tons of plastic debris floats on the ocean, and the plastics that enter the food chain adversely affect humans and marine organisms.[78]

Primary MPs are specifically manufactured to be within the micrometer size range. For example, plastic beads used in personal care products are denoted as primary MPs.[47] MPs appearing in the environment are mainly derived from household products and industrial processes,[79,80] including medicine as drug vectors,[81] cosmetics and facial cleansers.[82] Even though modern wastewater treatment measures can remove more than 90% of the MPs in wastewater, the treated wastewater still has a large number of MPs due to their huge amount.[83,84] Secondary MPs come from cracking of larger plastics. This process involves a combination of physical and chemical reactions including mechanical disintegration, oxidation, photodegradation and hydrolytic degradation.[48] Plastics are affected by high temperatures and UV radiation, which will trigger chemical changes, making them more fragile and more likely to fragment. UV radiation from sunlight can oxidize the polymer matrix, causing chemical bonds to break.[85] A combination of mechanical forces such as wave action, abrasion and turbulence make plastics susceptible to fragmentation.[85] However, research on NPs is still in its infancy, compared to research on other nanomaterials.[86–89] Studies have confirmed that the degradation of plastic particles will not stop at the micron level, but they will be further degraded to the nano level, forming NPs.[48]

MPs and NPs pose a huge threat to the health of various organisms including humans. Mattsson *et al.*[90] proved that NPs can penetrate the blood–brain barrier of fish and reduce the survival of aquatic zooplankton, thus causing behavioural disorders. The absorption and accumulation of PS MPs in zebrafish and their toxic effects on the liver were studied.[91] The results showed that after exposure for 1 week, MPs with a 20 μm diameter accumulated in the gut and fish gills, while MPs with a diameter of 5 μm were detected in the gut, fish gills and liver. Histopathological analysis showed that both 70 nm and 5 μm PS

MPs caused lipid accumulation and inflammation in fish liver. The results of Della *et al.*[92] showed that the accumulation of 1–50 μg mL^{-1} amine polystyrene (PS–NH$_2$) in sea urchin embryos would lead to changes in embryo toxicity and gene expression. When PS NPs and MPs are at high levels, they could cause the death of zooplankton organisms such as the marine copepod *Tigriopus japonicas*.[93] The potential hazards and risks of MPs and NPs in terms of human health have also attracted attention. The side effects of NPs in the human body include inflammation and activation of reactive oxygen species production, and the side effects of polymer nanoparticles in the human body include cytotoxicity, inflammation and activation of the production of reactive oxygen species. Iwona *et al.*[94] verified that mucin interacts with amine-modified 57 nm PS nanoparticles, and mucin could aggregate and induce intestinal epithelial cell death.

Oral inhalation, absorption by skin, ingestion during the use of plastic products, or inadvertent contact with plastic are all possible ways to access NPs.[48] There are three main ways that NPs enter the human body, gastrointestinal (GI) tract ingestion, oral inhalation into the lungs and absorption by the skin (Fig. 3a). Due to the daily diet requirements, the most important way for NPs to enter the human body is through ingestion, according to the current cognitive level. An experimental investigation shows that when brewing steeping a single plastic teabag at brewing temperature (95 °C), billions of NPs and tens of billions of MPs are released into a cup of tea.[95] The lungs have a large specific surface area, which can transport nanosized inhaled particles to the blood system and distribute them throughout the body. The treated sludge containing plastic particles is used as an agricultural fertilizer, but after the sludge dried, the wind can transfer and distribute the plastic particles, and human beings can absorb the distributed plastic particles through the lungs.[96] In addition, people can inhale MPs and NPs through the transport of sea salt aerosols (which are generated from wave action) containing polymer particles.[97] Plastic particles can also enter the human body through the skin through contact with air or water contaminated by plastic particles and many personal care products containing NPs. For instance, Vogt *et al.*[98] studied the effect of nanoparticles on improving the immune ability through transdermal administration and verified that among the nanoparticles of different sizes (40 nm, 750 nm and 1500 nm), fluorescent PS particles with 40 nm diameter could be taken up by the high-density Langerhans cells around the hair follicles and appeared in the human skin perifollicular tissue.

2.3 Plastic-derived chemicals

Chemical additives leached from plastic materials can also affect the health of human and other organisms (Fig. 3b). In the process of manufacturing plastics, chemicals such as stabilizers, pigments and plasticizers are often added to improve the performance of the final products, such as stability and flexibility.[48] The common additives used in different types of polymeric material packaging mainly include flame retardants, acid scavengers, plasticizers, antioxidants, heat and light stabilizers, thermal stabilizers, pigments, lubricants, slip compounds and antistatic agents. Each of them plays a different role in the final plastic products.[4] For example, BPA and PAEs are used as anti-ultraviolet radiation stabilizers.[24] Thousands of substances have been used for such purposes so far; however, some of them, mutagenic and carcinogenic materials for instance,[99] penetrate into the environment during their life cycle, and when exposed to organisms, they can cause acute toxicity or endocrine disorders.[48] The macromolecules of plastic materials are formed by chemical reactions between the respective monomers. During the degradation or decomposition of plastics, polymer monomers such as styrene monomers are easily released from the plastic matrices.[100] Microplastic materials such as PS, PE, PC (polycarbonate), and silicone have been shown to leach NP and

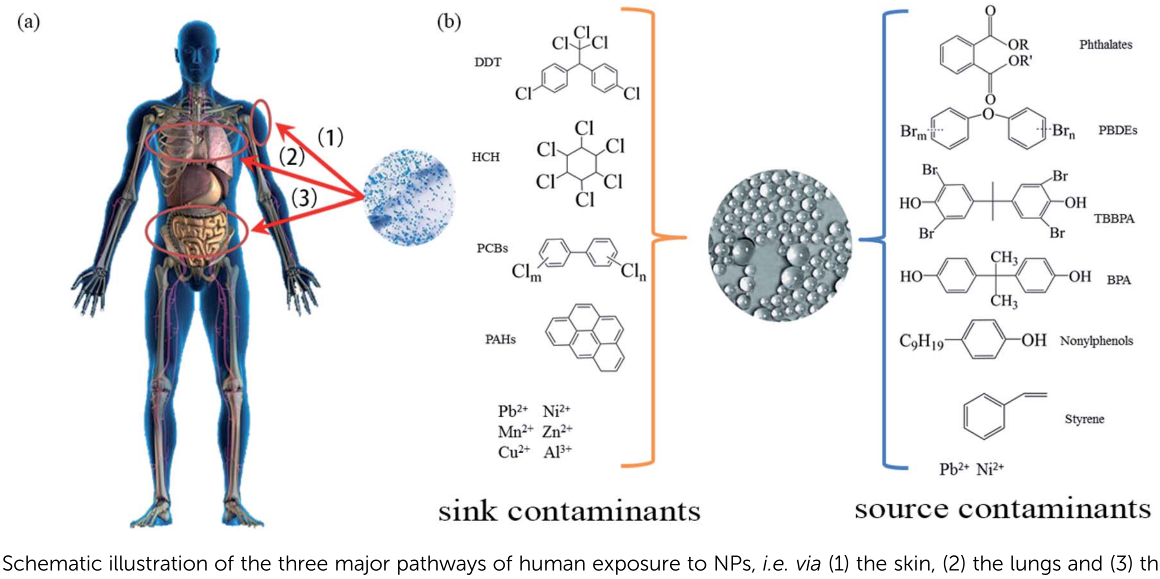

Fig. 3 (a) Schematic illustration of the three major pathways of human exposure to NPs, *i.e. via* (1) the skin, (2) the lungs and (3) the gastrointestinal (GI) tract. (b) Contaminants that are associated with plastic debris in the environment.

BPA.[101] BPA is a typical example of a leaching monomer that is used for the production of certain PC and epoxy resins.[48] It is a typical endocrine disruptor,[102] and has adverse effects on the human body such as reproductive and developmental effects as well as causing some metabolic diseases, due to its estrogenic activity.[48]

In addition to releasing additives added during the manufacture process of plastics, plastics can also absorb some toxic compounds from the environment (Fig. 3b) such as heavy metals and POPs.[103,104] PS, PP, PVC and PE possess strong adsorption for hexachlorocyclohexanes, chlorinated benzenes, polycyclic aromatic hydrocarbons (PAHs) and dichlorodiphenyltrichloroethanes (DDTs).[105] For instance, the concentration of polychlorinated biphenyls (PCBs) in microplastic particles is millions of orders of magnitude higher than that in the surrounding water environment.[79] These POPs are toxic, hydrophobic, bio-accumulative and persistent in the environment, and they also have the potential for long-distance transportation.[106] Thus, plastics with POPs have been detected worldwide. The highest value of organochloride pesticides and PCBs detected along the Portuguese coast reached 200 ng g^{-1} and 450 ng g^{-1}, respectively.[107] Organic chlorine compounds in PE pellet samples from 30 beaches in 17 countries were analyzed. The concentrations of PCBs and DDTs in pellets from the US coast are very high, and high levels of HCHs (pesticides) are also detected in pellets from southern Africa.[108]

3 Photocatalytic degradation of plastics

Photocatalytic technology shows excellent performance in the degradation of pollutants, including plastics. Plastics are difficult to degrade due to their low water solubility, complex structure and non-biodegradability. Also, as mentioned in Section 2, the presence of plastics and MPs in the environment brings about many negative effects. The recycling of plastics has aroused interest because "white pollution" not only pollutes the environment but is also a waste of resources. Therefore, careful management is needed to minimize the environmental impact of plastic waste. As mentioned in the "Introduction", the existing methods for removal of MPs from water or wastewater include physical methods, chemical methods and advanced technologies. These methods all have shortcomings, and photocatalysis has gradually been proven to be an effective method for plastic degradation. When the semiconductor absorbs light with $E \geq E_g$, the e^- located in the VB are transferred into the CB, leaving behind h^+. Both species react with H_2O, OH^- and O_2 adsorbed in the surface of the semiconductor to generate reactive oxygen species such as hydroxyl and superoxide radicals. These species initiate the plastic degradation process, leading to chain breaking, branching, crosslinking and finally, complete mineralization into H_2O and CO_2. There are few studies on photocatalytic degradation of plastics; thus, it will be very necessary and meaningful to summarize these studies (Table 1).

Photocatalytic degradation of MPs has recently been reported. Tofa *et al.*[28] investigated the photodegradation of microplastic residues of LDPE by ZnO nanorods. The results showed that many low molecular weight compounds were formed like peroxides, hydroperoxides and carbonyl and unsaturated groups. These new compounds led to cavities, cracks and wrinkles on the surface of residues (Fig. 4a–d). And the carbonyl index (CI) showed a 30% increase. The initial vinyl and carbonyl values of 0.51 and 0.71 indicate the presence of inherent chromophoric groups which are the primary initiators for the degradation. Based on all the results obtained in this study, they proposed the following degradation pathway for the LDPE film:

$$(-CH_2-CH_2-)_n + {}^{\bullet}OH^- \rightarrow (-{}^{\bullet}CH-CH_2-)_n + H_2O \tag{1}$$

$$(-{}^{\bullet}CH-CH_2-)_n + O_2 \rightarrow (-CH_2-HCOO^{\bullet}-CH_2-)_n \tag{2}$$

$$(-CH_2-HCOO^{\bullet}-CH_2-)_n + (-CH_2-CH_2-)_n \rightarrow (-CH_2-HCOOH-CH_2-)_n + (-{}^{\bullet}CH-CH_2-)_n \tag{3}$$

$$(-CH_2-HCOOH-CH_2-)_n \rightarrow (-CH_2-HCO^{\bullet}-CH_2-)_n + {}^{\bullet}OH^- \tag{4}$$

$$(-CH_2-HCO^{\bullet}-CH_2-)_n \rightarrow \text{carbonyl groups} \tag{5}$$

Norrish type I

$$(-CH_2-CO-CH_2-)_n \rightarrow (-CH_2-CO^{\bullet})_n + ({}^{\bullet}CH_2-CH_2)_n \tag{6}$$

Norrish type II

$$(-CH_2-CO-CH_2-)_n \rightarrow (-CH_2-CO)_n + ({}^{\bullet}CH_2{=}CH)_n \tag{7}$$

$$(-CH_2-HCO) + (-CH_2-COOH) + (-CH_2-CO-CH_2) \rightarrow CO_2 + H_2O \tag{8}$$

The generated superoxide and hydroxyl radicals from the photocatalyst initiate the cleavage of long polymeric chains to generate low molecular weight polyethylene alkyl radicals (eqn (1)). Subsequently (eqn (2)–(4)), peroxy radicals are generated with O_2 incorporation, followed by hydroperoxide group formation by the abstraction of H atoms from the polymeric chains. The hydroperoxide groups continuously react with alkoxy radicals to generate species containing vinyl and carbonyl groups (eqn (6) and (7)), which in turn leads to chain cleavage. Furthermore, they investigated the performance of plasmonic platinum/zinc oxide (ZnO–Pt) nanorods in the photodegradation of LDPE film. The presence of the Pt nanoparticle surface plasmon resonance effect enhanced the Pt loaded ZnO nanorod light absorption in the visible region greatly, while the ZnO nanorods had a strong ability to absorb UV light but a weak ability to absorb visible light (Fig. 4h). Meanwhile, ZnO–Pt showed a considerable reduction in the recombination of photo-generated h^+ and e^- compared to ZnO nanorod samples from the PL spectrum (Fig. 4i). Formation of peroxides, hydroperoxides, and unsaturated groups during the degradation process caused the degradation of the LDPE films. Several

Table 1 Photocatalytic degradation of different kinds of plastic[a]

Substrates	Photocatalysts	Experimental details	Experimental results	Ref.
LDPE microplastic residues	ZnO	A 50 W dichroic halogen lamp in ambient air was used for visible light illumination (≈60–70 klux); 175 h illumination; LDPE film of size 1 cm × 1 cm; 20 mM ZnO	The CI and VI showed a 30% increase; formation of new functional groups like hydroperoxide carbonyl and unsaturated groups during the photodegradation; cracks and spots could be found on the LDPE film after photodegradation	28
LDPE fragmented MPs	Pt/ZnO	A 50 W dichroic halogen lamp in ambient air was used for visible light illumination (≈60–70 klux); 175 h illumination; LDPE film in commercial use, with a thickness of 50 microns; ZnO–Pt substrates, with an average diameter and length of 960 μm, having dimensions of 2.5 cm × 0.75 cm, as the photocatalysts	The VI and the CI increased by 15% and 13%; several cracks, wrinkles and cavities of varying sizes were detected all over the photodegraded films as a result of the newly formed volatile organic compounds and oxygenated groups	29
HDPE MPs	C, N–TiO_2	200 mg of MPs and 200 mg of the photocatalyst added to 50 mL of a buffer solution with 50 h of continuous stirring; a 50 W LED lamp with emission in the visible spectrum and 50 h of continuous stirring at 300 rpm	Low pH and low temperature have a combined effect on MP degradation; at pH 3 and 0 °C, the mean mass loss after 50 h of irradiation was 71.77 ± 1.88%; the degradation rate constant, *k*, reached 0.0237	109
HDPE MPs	N–TiO_2	A 27 W fluorescent lamp with constant light emissions in the visible spectrum at room temperature for 20 h	The first order kinetic constant was calculated to be 12.2×10^{-4} h^{-1} and 38.2 ± 3.7 h^{-1} in solid and aqueous media	111
PE MPs	Hydroxy-rich ultrathin BiOCl	A circulating water system under a 250 W Xe lamp; 1 g L^{-1} of micron grade plastic (PE-S) or 10 g L^{-1} of millimeter grade plastic was dispersed in 100 mL of an aqueous solution; 1 g L^{-1} of the photocatalyst was added	The PE MPs catalyzed by BiOCl-1 with light displayed 5.38% mass loss, which was 134 and 24 times higher than that obtained with only light (0.04%) and BiOCl with light (0.22%)	118
PE and PP	ZrO_2, TiO_2	Under a sun simulator and under real sunlight for 20 hours; PE and PP films of size 1.5 cm × 1.5 cm; 10 000 ppm ZrO_2, TiO_2	The CIs of the original PE and PP were 0.0090 and 0.0072. The average CIs of PE and PP treated with ZrO_2 under a sun simulator and under real sunlight were 0.0244, 0.0382, 0.0149 and 0.0190; the average CIs of PE and PP treated with TiO_2 under the sun simulator and under real sunlight were 0.0226, 0.0260, 0.0112 and 0.0124; ZrO_2 could cause higher photocatalytic degradation than nano-TiO_2	112
PLA, PET and PUR	CdS/CdO_x	0.5 μM CdS QDs irradiated for 4 h at 25 °C with simulated solar light (AM 1.5G, 100 mW cm^{-2});	Photo-reforming of PUR, PET and PLA generated H_2 with activities of 0.85 ± 0.28, 3.42 ± 0.87 and 64.3 ± 14.7	113

Table 1 (*Contd.*)

Substrates	Photocatalysts	Experimental details	Experimental results	Ref.
		solution volume was 2 mL for 10 M aq. NaOH in a sealed photoreactor (internal volume of 7.91 mL) under anaerobic conditions; 50 mg mL^{-1} PLA, 25 mg mL^{-1} PET, 25 mg mL^{-1} PUR	$mmol_{H_2}$ g_{Cds}^{-1} h^{-1}, respectively. PLA in NaOH hydrolyzed to sodium lactate, which was oxidized to an alkalinity-induced pyruvate-based compound or pyruvate, PET hydrolyzed to terephthalate, ethylene glycol and isophthalate, while photo-oxidation produced formate, glycolate, ethanol, acetate and lactate, and PUR firstly hydrolyzed to aliphatic and aromatic components, where the aromatic constituent remained intact during PR, while the aliphatic components were photo-oxidized to pyruvate, acetate, formate and lactate	
PE and PVC	Pt/TiO_2	500 W Xe lamp, 10 h irradiation; 300 mg Pt/TiO_2; 150 mg PE and PVC, 30 mL deionized water	Photo-reforming of PE and PVC generated H_2 with activities of 0.015 and 0.031 $mmol_{H_2}$ g_{cat}^{-1} h^{-1} in 5 M aq. NaOH	114
PET and PLA	$CN_x\|Ni_2P$	Ultrasonicated $CN_x\|Ni_2P$ 2 wt% (3.2 mg), polymer (50 mg), aq. KOH (1 M or 10 M, 2 mL), sealed photoreactor (internal volume 7.91 mL); under anaerobic conditions, simulated solar light (AM 1.5G, 100 mW cm^{-2}, 25 °C)	H_2 conversion reached 6.7 ± 0.8% for PLA and 24.5 ± 3.3% for PET at higher pH (10 M KOH); the results showed that H_2 was generated continuously for 6 consecutive days, the photocatalytic activity reached 4.13 ± 0.40 $mmol_{H_2}$ g_{Cds}^{-1} h^{-1}, conversion was 5.15 ± 0.72% and external quantum yield was 2.17 ± 0.38% in real-world PET water bottle degradation; PET hydrolyzed to its monomers – ethylene glycol and terephthalate – or soluble oligomer fragments, and PLA hydrolyzed to lactate during pretreatment, which was then oxidized primarily to CO_3^{2-} and small quantities of acetate, formate, and other unidentified products	115
PET	$MoS_2/Cd_xZn_{1-x}S$	10 mg $MoS_2/Cd_xZn_{1-x}S$; 60 mL of the PET substrate solution; a 300 W Xe lamp with AM 1.5G was used as the light source; under anaerobic conditions	4.3 wt% MoS_2 in $MoS_2/Cd_xZn_{1-x}S$ exhibited the best H_2 evolution rate of 15.90 mmol g^{-1} h^{-1}; PET was eventually oxidized to small-molecule organic compounds, such as methanol, formate, methanol, ethanol and acetate	116
PP	$NiAl_2O_4$	A metal halide lamp of 350 W was used as the	Weight loss of PP-LDPE was 12.5% and 10% with NB	117

Table 1 (*Contd.*)

Substrates	Photocatalysts	Experimental details	Experimental results	Ref.
		source of visible light; PP film of size 3 cm × 3 cm; 30 mg of $NiAl_2O_4$; DMSO as solvent (20 mL)	spinel and NA spinel, respectively	

[a] MPs: microplastics; LDPE: low-density polyethylene; HDPE: high-density polyethylene; PE: polyethylene; PP: polypropylene; HDPE MPs: high-density polyethylene microplastics; PLA: polylactic acid; PET: polyethylene terephthalate; PUR: polyurethane; PVC: polyvinyl chloride; PE MPs: polyethylene microplastics; PR: photo-reforming; NB spinel: $NiAl_2O_4$ prepared *via* a hydrothermal route; NA spinel: $NiAl_2O_4$ prepared *via* a co-precipitation method.

cracks, wrinkles and cavities of varying sizes were detected all over the photodegraded films as a result of the newly formed volatile organic compounds and oxygenated groups. After photodegradation for 175 hours, compared with ZnO, ZnO–Pt made the film decompose to produce deeper wrinkles and cavities (Fig. 4e–g). The vinyl index (VI) and the CI which indirectly quantify the degree of degradation increased by 15% and 13%, respectively, indicating that the ZnO–Pt plasmonic photocatalysts have a better degradation efficiency compared to the bare ZnO.[29] These studies have shown that photocatalytic technology can be used to degrade MPs, but it has not achieved complete degradation. In order to achieve complete degradation, Ariza-Tarazona *et al.*[109] used mussels as a doping source to synthesize C, N–TiO_2 to explore the effect of temperature and pH on the degradation of HDPE MPs. The research results confirmed that a lower pH environment ($pH = 3$) was conducive to the formation of hydroperoxide in the photooxidation process, and the photocatalytic reaction under low temperature conditions could promote the fragmentation of the surface area of the MPs. At pH 3 and 0 °C, the highest degradation rate was obtained and the mean mass loss of HDPE MPs was 71.77 ± 1.88% after 50 h of irradiation, almost 6 times that at pH 3 and 40 °C. A comparison of the results under different experimental conditions revealed that the values of mass loss were in accordance with CI values, and 206% of the CI of HDPE MPs after photocatalysis at pH 3 and 0 °C. These results indicated that pH and temperature had a synergistic effect on photocatalytic degradation of HDPE MPs.

TiO_2 is also widely investigated because of its great features such as environmental benignity, good stability, and outstanding optical and electronic properties.[110] Ariza-Tarazona *et al.*[111] used two N–TiO_2 based photocatalysts for degradation of HDPE MPs. The one synthesized using the extrapallial fluid of saltwater mussels showed more sustainable performance and an outstanding capacity for mass loss of HDPE MPs in both aqueous and solid environments. Also, another N–TiO_2 photocatalyst, made from the conventional sol–gel route, showed good capacity for mass loss of HDPE MPs in an aqueous environment. Bandara *et al.*[112] compared the degradation of PP and PE by TiO_2 and ZrO_2 in a THF medium using nanoparticle suspensions. Analysis of the plastics' morphology during the degradation process found that the damage done by ZrO_2 to PE and PP was greater than that done by TiO_2 to PE and PP. The CI was used to assess the degradation of plastics indirectly. Under the optimal experimental conditions, TiO_2 nanoparticle suspension treated PP and PE samples exhibited lower degradation than that observed after ZrO_2 treatment under both sets of treatment conditions, with 95% confidence (Fig. 4j and k). This was because ZrO_2 had a mesoporous structure, higher band gap and stronger capability for stabilizing oxygen vacancies.

Photo-reforming (PR) can be carried out under ambient pressure and temperature, using sunlight as an energy source, and produces fuel-cell-grade H_2. Plastic is a valuable material that contains abundant chemical feedstocks and energy. PR provides a new path not only for degrading plastic waste but also for producing chemical products at the same time. Uekert *et al.*[113] used CdS/CdO_x quantum dots for PR of three polymers, PUR, PET and polylactic acid (PLA), produced commonly in alkaline aqueous solution (Fig. 5a). In a typical experiment with all conditions optimized, PR of PUR, PET and PLA generated H_2 with activities of 0.85 ± 0.28, 3.42 ± 0.87 and 64.3 ± 14.7 $\text{mmol}_{H_2}\ \text{g}_{\text{CdS}}^{-1}\ \text{h}^{-1}$, respectively. Superior to a previous report for plastic PR, 5% Pt/TiO_2 showed impressive rates of 0.015 and 0.031 $\text{mmol}_{H_2}\ \text{g}_{\text{cat}}^{-1}\ \text{h}^{-1}$ with PVC and PE in 5 M aq. NaOH.[114] And the H_2 production continued to 0.04 ± 0.01, 0.21 ± 0.04 and 3.09 ± 0.15 $\text{mmol}_{H_2}\ \text{g}_{\text{substrate}}^{-1}$ (Fig. 5b and c), corresponding to external quantum yields of 0.14 ± 0.03% for PUR, 3.74 ± 0.34% for PET and 3.74 ± 0.34% for PET at $\lambda = 430$ nm. Under optimized pre-treatment conditions, the PR activity for both PUR and PET improved by 4 times, to 3.22 ± 0.13 and 12.4 ± 2.0 $\text{mmol}_{H_2}\ \text{g}_{\text{CdS}}^{-1}\ \text{h}^{-1}$ (Fig. 5d). H_2 conversion reached 38.8 ± 4.0% for PLA and 16.6 ± 1.0% for PET at higher pH (10 M KOH); the values reported for $CN_x|Ni_2P$ were 6.7 ± 0.8% for PLA and 24.5 ± 3.3% for PET under the same conditions.[115] Analysis of their ^{1}H-NMR spectra found that PLA in NaOH was hydrolyzed to sodium lactate, which was oxidized to an alkalinity-induced pyruvate-based compound or pyruvate, PET was hydrolyzed to terephthalate, ethylene glycol and isophthalate, while photo-oxidation produced formate, glycolate, ethanol, acetate and lactate, and PUR was firstly hydrolyzed to aliphatic (propylene glycol or similar) and aromatic (2,6-diaminotoluene) components, and while the aromatic constituent remained intact during PR, the aliphatic components were photo-oxidized to pyruvate, acetate, formate and lactate. In the investigation of a real-world PET water bottle, the result showed that H_2 was

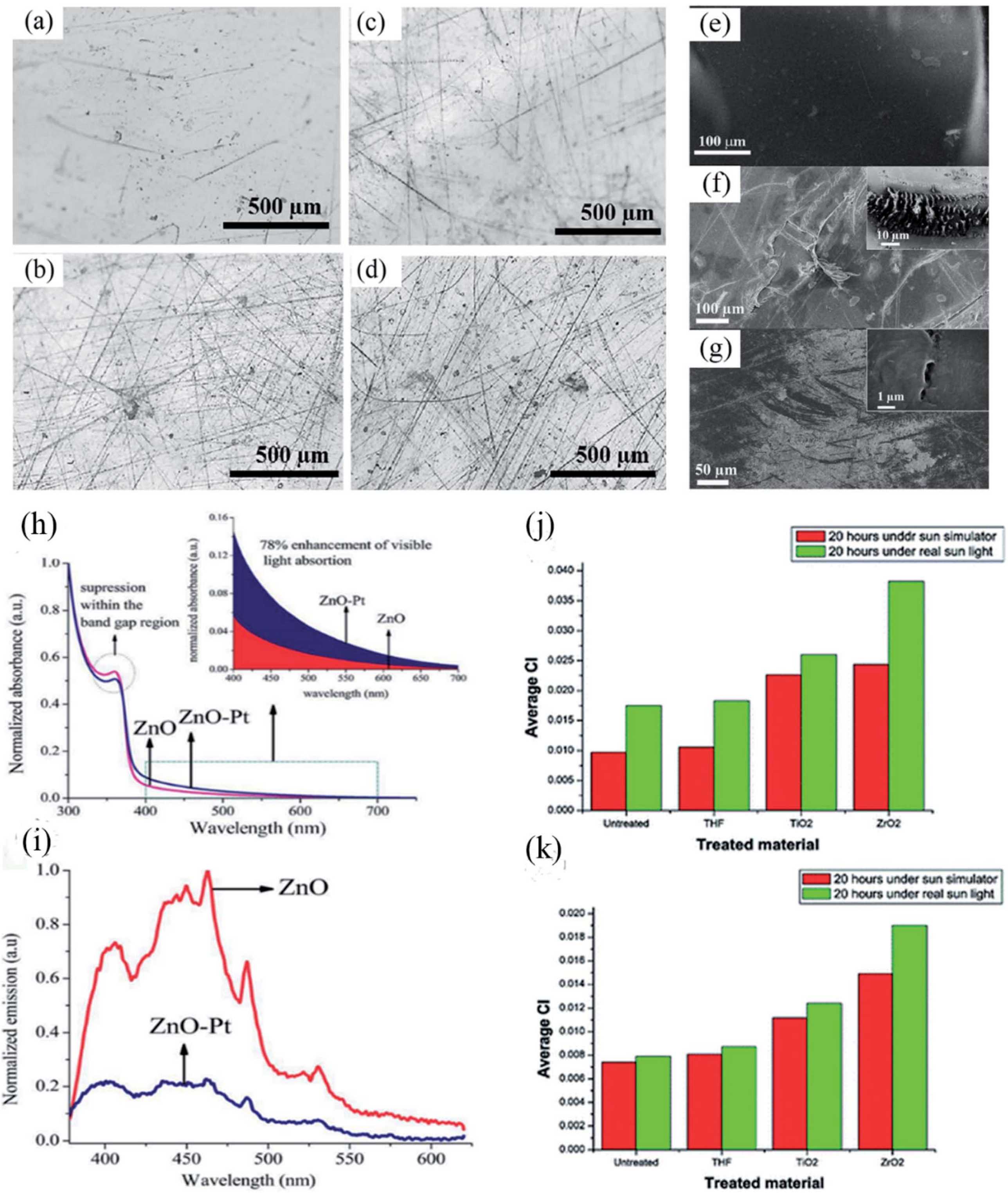

Fig. 4 (a) Microscopy images of the as-received LDPE and (b) 175 h photo-irradiated LDPE in contact with ZnO (10 mM_5 h), (c) ZnO (3 mM_5 h), and (d) ZnO (20 mM_5 h) nanorods. Reproduced with permission from ref. 28. Copyright 2019, Springer. (e) SEM images of LDPE film after 175 hours of visible light exposure: controlled LDPE, (f) ZnO, and (g) ZnO–Pt. (h) UV-vis adsorption spectra of ZnO nanorods and platinum nanoparticle-doped ZnO, and (i) emission spectra of ZnO nanorods and ZnO–Pt with 320 nm excitation. Reproduced with permission from ref. 29. Copyright 2019, Springer. Average CI variation of PE (j) and PP (k) under laboratory conditions and real conditions. Reproduced with permission from ref. 112. Copyright 2017, The Royal Society of Chemistry.

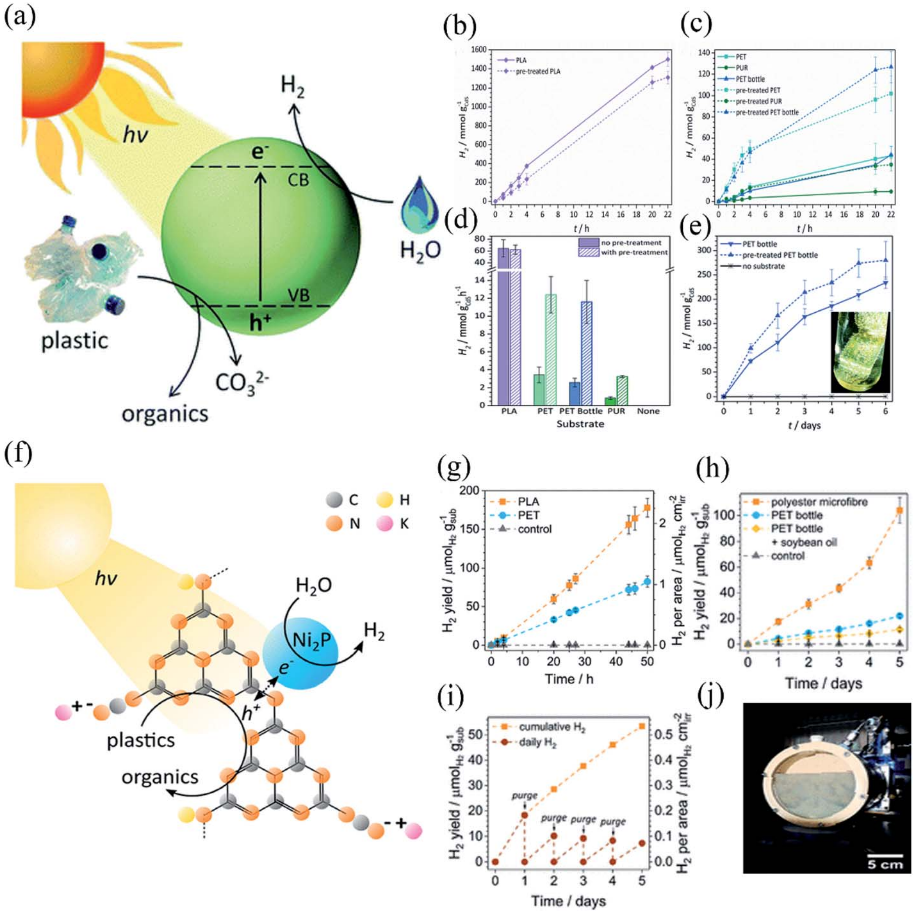

Fig. 5 (a) Schematic diagram of the polymer PR process using a CdS/CdO$_x$ quantum dot photocatalyst. (b) Long-term photocatalytic production of H_2 by CdS/CdO$_x$ QDs (1 nmol) from pure and pretreated PLA and (c) PET, PUR and PET bottle. (d) PR of polymers to H_2 using CdS/CdO$_x$ QD$_s$, and (e) long-term PR of a PET bottle to H_2 using CdS/CdO$_x$. Reproduced with permission from ref. 113. Copyright 2018, The Royal Society of Chemistry. (f) Schematic diagram of the polymer PR process using a CN$_x$|Ni$_2$P photocatalyst, (g) long-term PR of PET and PLA, (h) long-term PR of polyester microfibers, a PET bottle, and an oil-coated PET bottle, (i) upscaled PR of polyester microfibers (the sample was purged every 24 h), and (j) photograph of the batch reactor in use. Reproduced with permission from ref. 115. Copyright 2019, American Chemical Society.

generated continuously for 6 consecutive days and the photocatalytic activity reached 4.13 ± 0.40 $\text{mmol}_{H_2}\ g_{\text{CdS}}^{-1}\ h^{-1}$, with a conversion of 5.15 ± 0.72% and external quantum yield of 2.17 ± 0.38% (Fig. 5e). SEM inspection results showed that during the PR process, the surface of the untreated plastic bottle changed from a smooth shape to a grain shape featuring pits. Besides, the authors confirmed that H_2 could be evolved from PET, PUR, PLA and a PET water bottle using a carbon nitride/nickel phosphide (CN$_x$|Ni$_2$P) photocatalyst (Fig. 5f). 178 ± 12 and 82.5 ± 7.3 $\mu\text{mol}_{H_2}\ g_{\text{sub}}^{-1}$ were generated from PLA and PET after 50 h of irradiation, corresponding to turnover numbers of 16.8 ± 1.1 and 7.8 ± 0.7 $\text{mol}_{H_2}\ \text{mol}_{\text{Ni}}^{-1}$ for the respective polymers and external quantum yields of 0.101 ± 0.018% for PLA and 0.035 ± 0.005% for PET at $\lambda = 430$ nm (Fig. 5g). 1.6 ± 0.2% and 4.4 ± 0.6% H_2 conversions were achieved with PLA and PET after 8 days of PR. In order to explore the mechanism of photocatalytic degradation in the experiment, the authors performed PR with the OH$^•$ scavenger TPA. Through reaction with OH$^•$, TPA can be transformed into 2-hydroxyterephthalic acid, which fluoresces at $\lambda = 430$ nm when excited at $\lambda = 315$ nm. No TPA–OH emission was detected after 20 h of PR. PR likely proceeds *via* direct h$^+$ transfer between the substrate and CN$_x$. The h$^+$ transformed from the CN$_x$|Ni$_2$P photocatalyst to the substrate caused the oxidation half-reaction and yielded several valuable organic chemicals such as formate and acetate instead of CO_2. The ^{1}H-NMR spectra showed that PET was hydrolyzed to its monomers – ethylene glycol and terephthalate – or soluble oligomer fragments, and PLA was hydrolyzed to lactate during pretreatment, which was then oxidized primarily to CO_3^{2-} and small quantities of acetate, formate, and other unidentified products. In addition, the degradation of real-world polymeric material samples including oil-contaminated PET and polyester microfibers was also studied. 11.4 ± 1.2, 22.0 ± 1.3 and 104 ± 10 $\mu\text{mol}_{H_2}\ g_{\text{sub}}^{-1}$ were achieved from oil-contaminated PET, a PET bottle and microfibers after 5 days of illumination, respectively (Fig. 5h). Expanding the experimental setup to 120 mL for research purposes found that over the course of 5 days, 53.5 $\mu\text{mol}_{H_2}\ g_{\text{sub}}^{-1}$ was produced from PR of microfibers (Fig. 5i and j).[115]

To achieve the degradation of plastics, highly active $^{\bullet}OH$ radicals are generally required to participate in the reactions. Bearing this in mind, Jiao *et al.*[10] selected Nb_2O_5 to achieve production of C_2 fuels from waste plastics by photocatalytic conversion under simulated natural environment conditions (Fig. 6). By a sequential photoinduced C–C cleavage and coupling pathway, disposable food containers, single-use bags, food wrap films, and their main components, PP, PE and PVC, could be transformed into CH_3COOH by photocatalysis in the absence of sacrificial agents. Among them, PP could be completely converted into CO_2 by Nb_2O_5 within 40 hours, and the produced CO_2 was further reduced to CH_3COOH. To unveil the degradation process, they carried out a series of experiments and used a series of technical means including isotope-labeling experiments, *in situ* electron paramagnetic resonance (EPR) spectra, *in situ* FTIR spectra, and synchrotron radiation vacuum ultraviolet photoionization mass spectrometry (SVUV-PIMS). Tests confirmed that $^{\bullet}OH$ and O_2 caused the C–C rupture of PE, thereby generated CO_2. By coupling the $^{\bullet}COOH$ intermediates of C–C, CO_2 could be reduced to CH_3COOH. Taking all the above results into consideration, it was proposed that the photoconversion of pure PE into CH_3COOH underwent the two following sequential C–C bond cleavage and coupling processes:

Step 1: pure PE was primarily photodegraded into CO_2:

$$H_2O + h^+ \rightarrow {}^{\bullet}OH + H^+ \tag{9a}$$

$$(\text{–}CH_2\text{–}CH_2\text{–})_n + {}^{\bullet}OH + O_2 \rightarrow 2nCO_2 \tag{9b}$$

Meanwhile, O_2 was reduced to H_2O:

$$O_2 + e^- \rightarrow {}^{\bullet}O_2^- \tag{10a}$$

$${}^{\bullet}O_2^- + e^- + 2H^+ \rightarrow H_2O_2 \tag{10b}$$

$$H_2O_2 + 2e^- + 2H^+ \rightarrow 2H_2O \tag{10c}$$

Step 2: CO_2 was reduced to CH_3COOH:

$$CO_2 + e^- + H^+ \rightarrow {}^{\bullet}COOH \tag{11a}$$

$${}^{\bullet}COOH + {}^{\bullet}COOH \rightarrow HOOC\text{–}COOH \tag{11b}$$

$$HOOC\text{–}COOH + 6e^- + 6H^+ \rightarrow CH_3COOH + 2H_2O \tag{11c}$$

Simultaneously, H_2O was oxidized to O_2:

$$2H_2O + 4h^+ \rightarrow O_2 + 4H^+ \tag{12}$$

A 2D/2D cocatalyst/photocatalyst with a large and robust heterointerface can facilitate interface charge transfer to a great extent. Loading a hydrogen evolution cocatalyst on $C_xZ_{1-x}S$ is an efficient means of enhancing charge carrier separation and offering active sites for catalytic H_2 evolution, and it suppresses photo-corrosion. Motivated by this, Zhang *et al.*[116] fabricated MoS_2/$Cd_xZn_{1-x}S$ photocatalysts with a uniform 2D/2D structure for production of solar water-reductive H_2 with the degradation of PET plastic. PET (1.5 g) or pieces of PET bottles were added into 60 mL of 10 M NaOH aqueous solution and stirred for 24 h at 40 °C. The formed mixture was centrifuged for 3 min at 6000 rpm, and then

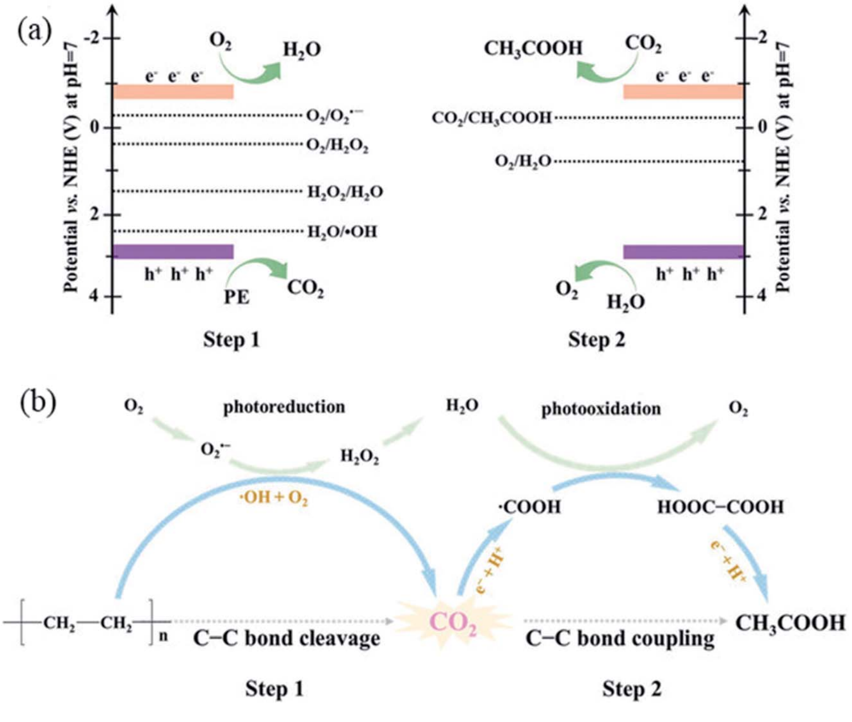

Fig. 6 Schematic representations for (a) the band-edge positions of Nb_2O_5 atomic layers along with the potentials of CO_2, H_2O, H_2O_2, and O_2 redox couples at pH 7 and (b) the proposed two-step C–C bond cleavage and coupling mechanism from pure PE into CH_3COOH under simulated natural environment conditions. Reproduced with permission from ref. 10. Copyright 2020, Wiley-VCH.

the supernatant was used as the substrate for photocatalytic H_2 evolution. 4.3 wt% MoS_2 in $MoS_2/Cd_xZn_{1-x}S$ exhibited the best H_2 evolution rate of 15.90 mmol g^{-1} h^{-1}. ^{1}H-NMR spectroscopy was adopted to analyze the products of photocatalytic PET degradation. The results showed that the plastic is effectively degraded into some small molecules such as acetate and formate (Fig. 7b). The photocatalytic mechanism for the redox coupling can be seen in Fig. 7a. When the photocatalyst was irradiated, photoexcited carriers were generated, and the photogenerated e^- migrated to the MoS_2 surface, where H_2O was reduced to H_2. Simultaneously, the PET polymer was eventually oxidized to formate, methanol, acetate, ethanol, *etc.* by photoinduced h^+.

With relatively low cost, nickel based catalysts have attracted great attention from researchers. Since there are very few studies conducted on degradation of PE plastics using metal oxides or spinels, Venkataramana and co-workers[117] prepared $NiAl_2O_4$ spinels by co-precipitation (denoted as NA) and hydrothermal (denoted as NB) methods for photocatalytic degradation of PP-LDPE. The experimental process was similar to the general photocatalytic degradation of pollutants. Firstly, 30 mg PP-LDPE was placed in the solution under dark conditions for half an hour to achieve adsorption equilibrium between PP-LDPE and the spinel. Secondly, light was allowed to fall on it for 5 h continuously and the solvent and a small piece were collected every hour to determine the photodegradation of PP-LDPE using FTIR analysis with a measurement range of 4000–5000 cm^{-1}. The results showed that NB spinel prepared by hydrothermal assisted synthesis is much more favourable for the degradation of PPs under visible light illumination; besides, the weight loss of PP-LDPE was higher with NB spinel (12.5%) than NA spinel (10%). The difference in the results might be due to the difference in size, surface and crystallinity of the two catalysts. The degradation pathways are explained below:

$$NiAl_2O_4 + h\nu \rightarrow h^+ + e^- \tag{13}$$

$$h^+ + H_2O/OH \rightarrow {}^{\bullet}OH \tag{14}$$

$$e^- + O_2 \rightarrow {}^{\bullet}O_2^- \tag{15}$$

$$(\text{–}CH_2CH_2\text{–})_n + {}^{\bullet}OH \rightarrow (\text{–}CHCH_2\text{–})_n + H_2O \tag{16}$$

$$(\text{–}CHCH_2\text{–})_n + O_2 \rightarrow (\text{–}CH_2\text{–}HCOO^{\bullet}\text{–}CH_2)_n \tag{17}$$

$$(\text{–}CH_2\text{–}HCOO^{\bullet}\text{–}CH_2)_n + (\text{–}CH_2CH_2\text{–})_n \rightarrow (\text{–}CH_2\text{–}HCOOH\text{–}CH_2\text{–})_n + (\text{–}^{\bullet}CHCH_2\text{–})_n \tag{18}$$

$$(\text{–}CH_2\text{–}HCOOH\text{–}CH_2\text{–})_n \rightarrow (\text{–}CH_2\text{–}HCO^{\bullet}\text{–}CH_2\text{–})_n + {}^{\bullet}OH \tag{19}$$

$$(\text{–}CH_2\text{–}HCO^{\bullet}\text{–}CH_2\text{–})_n + (\text{–}CH_2CH_2\text{–})_n \rightarrow (\text{–}^{\bullet}CHCH_2\text{–})_n + (\text{–}CH_2\text{–}HCOH\text{–}CH_2\text{–})_n \tag{20}$$

Besides, Lu *et al.*[118] successfully prepared a novel hydroxy-rich ultrathin BiOCl and completed the experiment of photodegradation of high-density polyethene microspheres (PE-S) under simulated solar light. The PE-S catalyzed by BiOCl-1 with light displayed 5.38% mass loss, which was 134 and 24 times higher than that obtained with only light (0.04%) and BiOCl with light (0.22%), respectively. The strong characteristic signals of $DMPO^{\bullet}O_2^-$ and $DMPO^{\bullet}OH$ were observed in the presence of BiOCl and the signal intensity was weaker than that of BiOCl-1 (Fig. 7d and e). The results verified that BiOCl-1 could

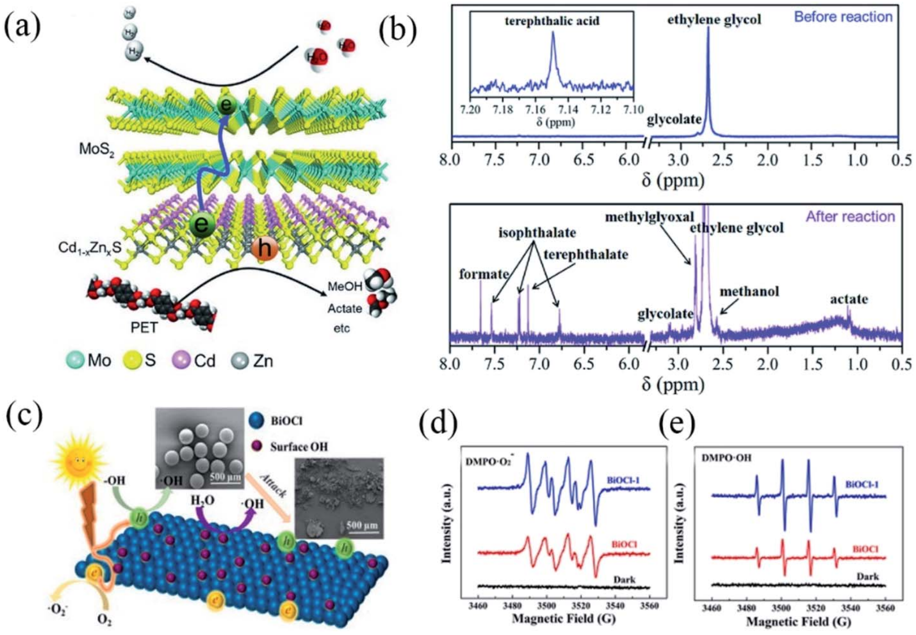

Fig. 7 (a) The mechanism of H_2 evolution coupled with the degradation of PET plastic over $M_t/C_xZ_{1-x}S$, and (b) ^{1}H-NMR spectra of an aqueous solution of PET plastic before and after photocatalytic H_2 generation for 5 h. Reproduced with permission from ref. 116. Copyright 2020, Elsevier. (c) Microplastic degradation by hydroxy-rich BiOCl, and PR signals for $DMPO^{\bullet}O_2^-$ (d) and $DMPO^{\bullet}OH$ (e). Reproduced with permission from ref. 118. Copyright 2020, Elsevier.

produce $^{\bullet}O_2^-$ and $^{\bullet}OH$ under visible light irradiation. Meanwhile, the active species trapping experiment results showed that adding the $^{\bullet}O_2^-$ scavenger (BQ) did not change the photocatalytic performance, while the catalytic degradation performance of PE-S decreased rapidly after adding $^{\bullet}OH$ (IPA). Therefore, the hydroxyl radical was the main reaction group in the photocatalytic degradation of PE-S by hydroxy-rich ultrathin BiOCl. The degradation mechanism diagram is shown in Fig. 7c and the main hydroxyl free radical generation pathways in the degradation process can be seen below:

$$BiOCl–OH^- + h\nu \rightarrow h^+ + e^- \quad (21)$$

$$e^- + O_2 \rightarrow {}^{\bullet}O_2^- \quad (22)$$

$$h^+ + OH^- \rightarrow {}^{\bullet}OH \quad (23)$$

$$BiOCl–OH^- + H_2O \rightarrow BiOCl–OH^- + {}^{\bullet}OH + H^+ \quad (24)$$

$$^{\bullet}O_2^- + {}^{\bullet}OH + \text{microplastics} \rightarrow CO_2 + H_2O \quad (25)$$

4 Photocatalytic degradation of the main plastic-derived chemicals

In the following section, emphasis is placed on research into photocatalytic degradation of several kinds of plastic-derived chemical often detected in the environment, including PAEs, BPA, BFRs and NP. In the process of photocatalytic degradation of organic contaminants, when the energy absorbed by the photocatalyst ($h\nu$) is higher than or equal to the band gap energy (E_g), it will cause e^- on the semiconductor to be excited from the VB to the CB, leaving h^+ in the VB. Subsequently, the CB attains a negative charge and it is reducing while the VB acquires a positive charge and it is oxidizing. Basically, the CB e^- are trapped by O_2 to form $^{\bullet}O_2^-$, another important oxidizing agent, while the VB h^+ capture OH^- or H_2O to form the extremely powerful, non-selective, oxidizing $OH^{\bullet}$. The $OH^{\bullet}$ and $^{\bullet}O_2^-$ partake in the degradation of the organic pollutants into intermediates and even CO_2 and H_2O.[119–121] The various reactions responsible for the formation of these oxidizing species and plastic-derived chemical degradation are depicted below:

$$\text{Semiconductor (SC)} + h\nu \rightarrow h^+_{(VB)} + e^-_{(CB)} \quad (26)$$

$$h^+_{(VB)} + H_2O \rightarrow OH^{\bullet} + H^+ \quad (27)$$

$$h^+_{(VB)} + OH^- \rightarrow OH^{\bullet} \quad (28)$$

$$e^-_{(CB)} + O_2 \rightarrow {}^{\bullet}O_2^- \quad (29)$$

$$OH^{\bullet} + OH^{\bullet} \rightarrow H_2O_2 \quad (30)$$

$$H_2O_2 + h\nu \rightarrow 2OH^{\bullet} \quad (31)$$

$$H_2O_2 + {}^{\bullet}O_2^- \rightarrow OH^{\bullet} + O_2 + OH^- \quad (32)$$

$$e^-_{(CB)} + H_2O_2 \rightarrow OH^{\bullet} + OH^- \quad (33)$$

$$^{\bullet}O_2^- + OH^{\bullet} + \text{pollutans} \rightarrow \text{degradation products} \quad (34)$$

4.1 Phthalic acid ester plasticizers

PAEs are used as plasticizers and widely used in plastic manufacturing processes. PAEs in the environment are mainly derived from the weathering of plastics and materials containing PAEs. Because they are difficult to be degraded by microorganisms in the environment, they are widely distributed in natural water bodies, which has a significant impact on the environment.[122,123] Photocatalytic degradation is a promising technology for the removal of PAEs.

Doping is an effective way to improve photocatalytic performance. Common non-metallic doping elements include C, N, O, S, P, *etc.*,[124,125] while the most commonly studied metal doping elements include K, Na, Cu, Fe, *etc.*[125,126] Many studies have modified photocatalysts by doping to improve their ability to degrade PAEs. Due to its simple and easy operation process, non-metal ion doping has attracted much interest. The degradation of diethylhexyl phthalate (DEHP) by N-doped TiO_2 under ozone and visible light was studied by Anandan *et al.*[124] The experimental results showed that the photocatalytic degradation rate of N_x–TiO_{2-x} was faster than that of TiO_2 under visible light. TiO_2 doped with halogen has many advantages such as reducing the band gap of TiO_2 and enhancing the photocatalytic activity under UV light. Wang *et al.*[127] reported that Cl-doped TiO_2 could absorb higher wavelength light. Under the same conditions of visible light irradiation for 4 h, more than 92% of butyl benzyl phthalate (BBP) could be degraded by Cl-doped TiO_2, while only 30% and 16% could be degraded by P25 and pure TiO_2, respectively. Co-doping is also a good method to improve photocatalytic activity. Graphene quantum dots/Mn–N–TiO_2/g-C_3N_4 (GQDs/TCN) catalysts with different weight ratios of g-C_3N_4 nanosheets (CNS) against Mn–N–TiO_2 prepared through hydrothermal reaction methods were examined towards photocatalytic degradation of organic pollutants with H_2 evolution.[128] The 5% GQDs/TCN-0.4 catalyst was chosen to explore the relationship between H_2 production and degradation of pollutants. The degradation rates of ciprofloxacin (CIP), diethyl phthalate (DEP) and *p*-nitrophenol (4-NP) are 89%, 70.4% and 48.6%, respectively, while the H_2 production rate in different reaction systems follows the order of H_2O < 4-NP < DEP < CIP. The reaction mechanism is shown in Fig. 8a. When irradiated with simulated solar radiation, GQDs in the GQDs/TCN-0.4 photocatalyst could convert the absorbed long-wavelength light into short-wavelength light absorbed by CNS and Mn–N–TiO_2. Both Mn–N–TiO_2 and CNS were excited by light at the same time to generate photo-generated e^- and h^+. The H_2O molecules on Pt or GQDs on the surface of Mn–N–TiO_2 could be reduced by the e^- transferred from the CB of the CNS to the CB of Mn–N–TiO_2, to generate H_2. In the system of 4-NP degradation, a small portion of e^- would be consumed by the degradation intermediates, so the efficiency of H_2 production was not as efficient as in the other two pollutant degradation systems. The h^+ transferred from the Mn–N–TiO_2 VB to the CNS VB could oxidize OH^- to $^{\bullet}OH$, which was used for pollutant

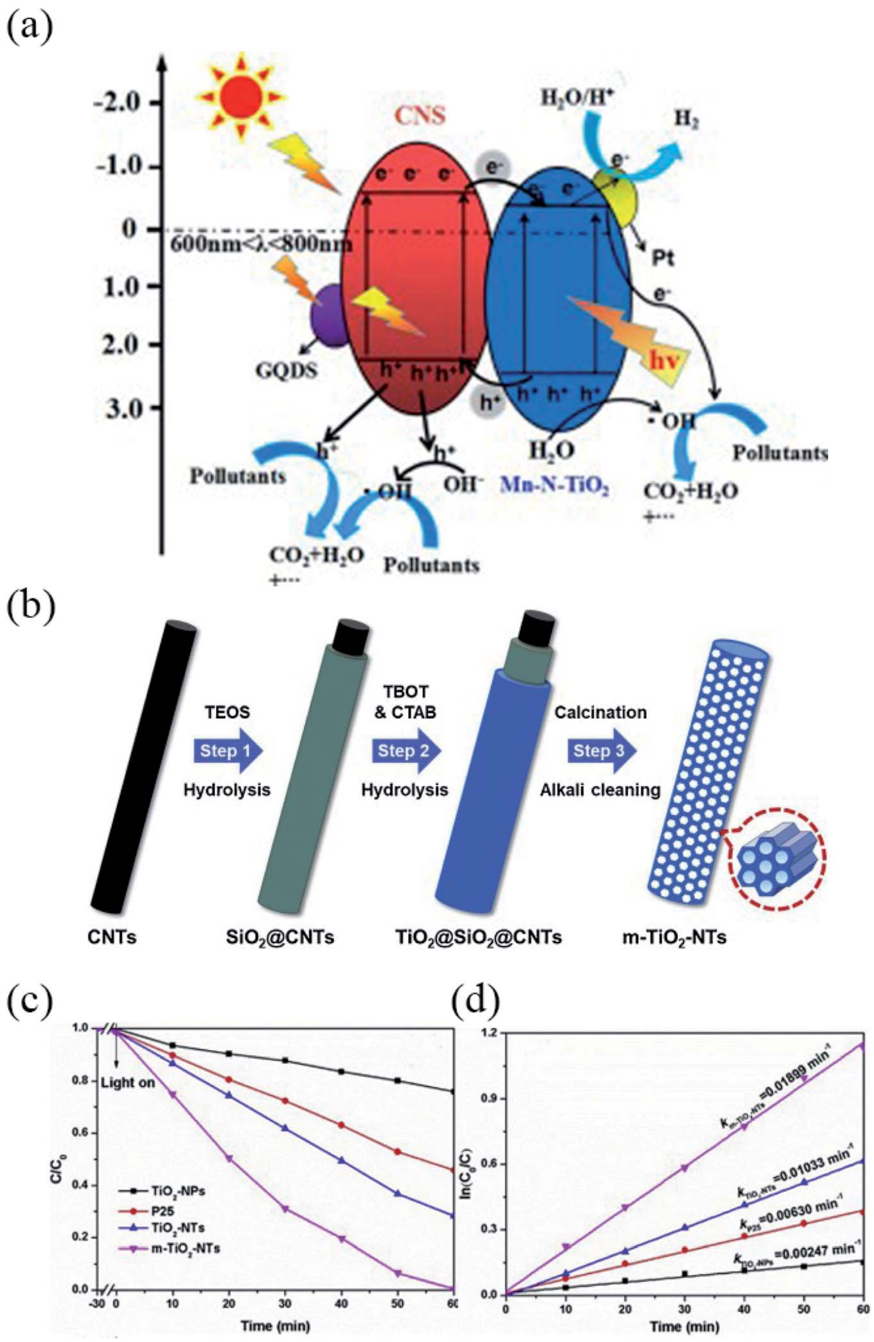

Fig. 8 (a) Possible photocatalytic mechanism of degradation of organic pollutants coupled with simultaneous photocatalytic H_2 evolution over GQDs/TCN-0.4 under simulated solar irradiation. Reproduced with permission from ref. 128. Copyright 2018, Elsevier. (b) Schematic illustration of the synthesis of mesoporous TiO_2 nanotubes prepared by the dual-template method, (c) photocatalytic degradation of DBP over different TiO_2 photocatalysts under UV light irradiation, and (d) linear fit log plots of DBP degradation curves. Reproduced with permission from ref. 130. Copyright 2019, Elsevier.

degradation, while h^+ could also degrade pollutants directly. Ma *et al.*[129] announced that the degradation efficiency of TiO_2-NTs-(0.8, 9.4) (99.8%) on DEP was higher than those of TiO_2-NTs (66.0%), Pt/In_2O_3–TiO_2-NPs-(0.8, 9.4) (73.5%), and In_2O_3–TiO_2-NTs-(0, 9.4) (91.6%). The enhanced photocatalytic performance was due to two reasons: (1) doped Pt and In_2O_3 enhanced the separation of electron–hole pairs; (2) the structure of nanotubes was favorable for the distribution of In_2O_3 and Pt in the nanotubes, and the mesoporous morphology and high adsorption capacity were favorable for the migration of substances to active sites.

The morphology of the photocatalyst also greatly affects the photocatalytic activity, because it determines the chemical and physical properties of the photocatalyst for surface reactions, light absorption and charge transfer efficiency.[130] Therefore, in the degradation of PAEs, changing the morphology of photocatalysts can also significantly improve the degradation efficiency. For instance, Ma *et al.*[131] verified that TiO_2 nanotube (TiO_2 NT) films exhibited stronger photocatalytic activity in photocatalytic degradation of dioctyl phthalate (DOP) than TiO_2 nanoparticle (TiO_2 NP) films, because the TiO_2 NT film structure facilitated O_2 adsorption and the transfer of degradation byproducts and photo-generated free radicals. TiO_2 NTs have the advantages of a large number of surface defects and large specific surface area, but there are still disadvantages; for example, their opaque walls and long channels will affect light transmission and their small size will affect mass transfer. To overcome the above disadvantages, He and co-workers[130] synthesized mesoporous TiO_2 nanotubes (m-TiO_2-NTs) *via* a dual-template method to investigate their photocatalytic performance. A schematic diagram of the photocatalyst synthesis can be seen in Fig. 8b. It can be seen that dibutyl phthalate (DBP) could be degraded by m-TiO_2-NTs more efficiently than other photocatalysts, and the corresponding reaction rate constants were 1.8, 3.0, and 7.7 times higher than those of TiO_2-NTs, P25 and TiO_2-NPs, respectively (Fig. 8c and d). This result could be attributed to the multi-channel structure improving light utilization while exposing more active sites.

12-Tungstophosphoric acid ($H_3PW_{12}O_{40}$) is a highly efficient electron trap with a good Keggin structure and a kind of polyoxometalate widely used in photocatalytic reactions. Introducing $H_3PW_{12}O_{40}$ into photocatalysts can effectively inhibit the recombination of photogenerated carriers. Li and coworkers[132] fabricated $H_3PW_{12}O_{40}$ modified carbon nitride nanotubes ($H_3PW_{12}O_{40}/C_3N_4$ NTs) with different mass ratios of $H_3PW_{12}O_{40}$ to g-C_3N_4. DEP was selected as the target degradation material to study the photocatalyst performance under visible light irradiation. $H_3PW_{12}O_{40}/C_3N_4$ NTs (3 : 10) had the best photocatalytic activity among all the prepared photocatalysts; they achieved 100% degradation rate and 24.5% removal rate of DEP after being stimulated by visible-light irradiation for 1 and 2 days. The author attributed these results to three main reasons: (1) the high light-utilization efficiency boosted the production of photogenerated h^+–e^- pairs; (2) incorporating a Keggin structure with strong electron-accepting ability into C_3N_4 NTs enhanced the quantum efficiency; (3) the nanotube structure could increase the number of active sites and increase their availability. Xu *et al.*[133] reported that the degradation efficiencies of dimethyl phthalate (DMP), DEP and DBP over PW_{12}/TiO_2-19.8 (the loading (wt%) of $H_3PW_{12}O_{40}$ in the PW_{12}/TiO_2 composite was 19.8%) were 80%, 84% and 98%, respectively, after being irradiated with simulated sunlight for 1.5 h. Li *et al.*[134] prepared a series of mesoporous $H_3PW_{12}O_{40}$–titania materials with controlled pore geometries and structural configurations. Under simulated sunlight irradiation, $H_3PW_{12}O_{40}$–titania photocatalysts with appropriate $H_3PW_{12}O_{40}$ loading showed a higher photocatalytic activity compared to pristine TiO_2 in the degradation of DEP.

4.2 Nonylphenol antioxidants

Nonylphenol ethoxylates (NPEs) are widely used antioxidants and surfactants. And their intermediate product NP is recognized as an endocrine disruptor which is harmful to human health and is banned by the European Union.[135] Also, it is one of the most common plastic additives found in the environment.[45,136] In the field of photocatalysis, there are also studies on the degradation of NP. Studies on photocatalysts for the degradation of NP mainly focus on TiO_2-based, $BiVO_4$-based and ZnO-based photocatalysts. Tang *et al.*[137] grafted perfluorooctyl groups onto TiO_2 nanotubes to obtain TiO_2 nanotubes with hydrophobic properties for photocatalytic oxidation of NP. Under the same experimental conditions, NP could be completely degraded by hydrophobic TiO_2 nanotubes (H-TiO_2 NTs) after 40 min of light irradiation, while only 87% of NP could be completely degraded by hydrophilic TiO_2 nanotubes (TiO_2 NTs). The reasons for this phenomenon could be summarized as follows: (1) compared with pure TiO_2, H-TiO_2 NTs had a stronger ability to adsorb NP; (2) the hydrophobic surface of H-TiO_2 NTs was beneficial for the generation of $^{\bullet}OH$, thereby promoting the degradation. In an early study, Inumaru *et al.*[138] discovered that *n*-octyl-grafted TiO_2 (C_8-TiO_2) performed well in the degradation of NP in the presence of phenol, being more efficient than TiO_2 under the same conditions due to the selective adsorption properties of the hydrophobic surface. There are also related studies on the photocatalytic degradation of NP with TiO_2 modified by metal and non-metal doping. Noorimotlagh *et al.*[136] incorporated C into TiO_2 as C-doped TiO_2 with anatase/rutile (A/R) coated on granular activated carbon (GAC). Under optimal experimental conditions, CDT (A/R)/GAC achieved complete NP degradation after 1 h of visible light irradiation. The simplified mechanism can be seen in Fig. 9a. Naya *et al.*[139] used a deposition–precipitation method to prepare a Au nanoparticle-loaded rutile TiO_2 (Au/rutile TiO_2) photocatalyst. The TEM of Au/rutile and UV-vis absorption spectra of rutile and Au/rutile can be seen in Fig. 9c and d. Au nanoparticles (Au NPs) were evenly distributed on the TiO_2 surface and TiO_2 has inter-band transition only below ∼400 nm; Au/rutile exhibited broad and strong light absorption capabilities. Compared to $BiVO_4$ and Au/anatase, Au/rutile TiO_2 had better photocatalytic performance as shown in Fig. 9e. The mechanism of NP degradation is shown in Fig. 9b. Firstly, NP was quickly adsorbed and enriched on the surface of Au NPs, and because of the local plasmon resonance of Au NPs, the e^- generated by them were quickly transferred to TiO_2; at the same time, continuous oxidative decomposition of NP was achieved. The intermediates were transferred from the Au NPs to the TiO_2 surface and were further oxidized to CO_2.

Ye *et al.*[140] constructed $BiVO_4$–Au@CdS to study the degradation of 4-nonylphenol. The schematic diagram for the synthesis of $BiVO_4$–Au@CdS can be seen in Fig. 10a (samples with Au@CdS non-selectively deposited on the {110} and {010} facets and selectively deposited on the {010} facets of $BiVO_4$ are denoted as c-$BiVO_4$–Au@CdS and $BiVO_4$–Au@CdS, respectively). From Fig. 10c–e, the degradation kinetic rate of 4-nonylphenol over $BiVO_4$–Au@CdS-2 was higher than those of $BiVO_4$–Au-2, $BiVO_4$ and $BiVO_4$–CdS, and this result indicated that the deposition of CdS and Au could improve the overall photocatalytic performance, which was attributed to the formation of Z-type heterojunctions in $BiVO_4$–Au@CdS. It can also be seen from

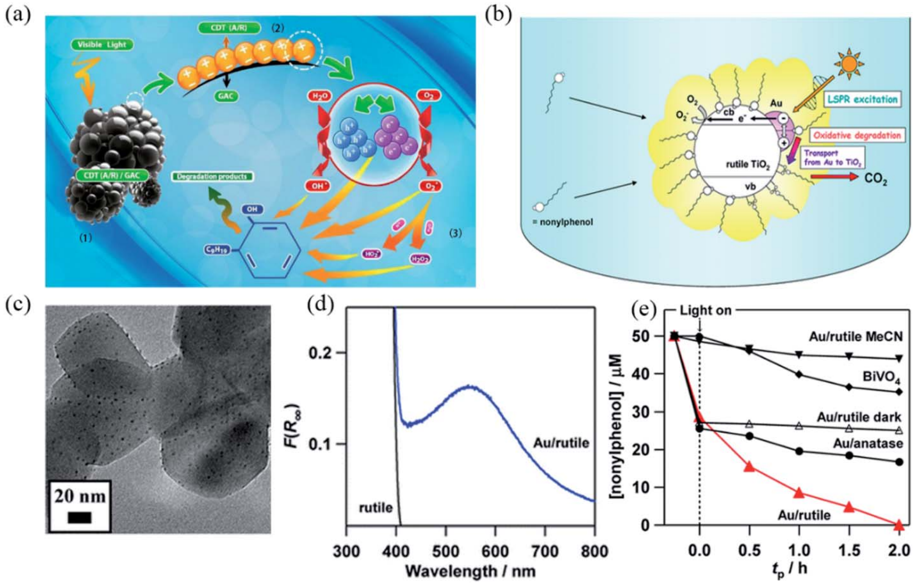

Fig. 9 (a) Simplified mechanism for photocatalytic degradation of NP using CDT (A/R)/GAC. Reproduced with permission from ref. 136. Copyright 2018, Elsevier. (b) Proposed mechanism of NP degradation by the Au/rutile TiO_2 plasmon photocatalyst, (c) TEM of Au/rutile, (d) UV-vis absorption spectra of rutile and Au/rutile, and (e) time courses for NP degradation. Reproduced with permission from ref. 139. Copyright 2013, American Chemical Society.

the photocatalytic loss over 4 cycles that $BiVO_4$–Au@CdS-2 had a good stability (Fig. 10f). From Fig. 10g–i, the higher photocurrent and stronger PL intensity for c-$BiVO_4$–Au@CdS and c-$BiVO_4$–Au compared with those of $BiVO_4$–Au@CdS and $BiVO_4$–Au can be observed, despite the similar light absorption characteristics. This means that the carrier separation efficiency of $BiVO_4$–Au@Cd was higher than that of c-$BiVO_4$–Au@Cd. The degradation kinetic rate of c-$BiVO_4$–Au@CdS (0.0221 min^{-1}) was only about half that of $BiVO_4$–Au@CdS (0.0430 min^{-1}) (Fig. 10j). The phenomenon was ascribed to two aspects: the synergistic effect between the Z-scheme mechanism and facet induction effect of $BiVO_4$ (Fig. 10b).

In addition to TiO_2 and $BiVO_4$, ZnO is also widely used in photocatalytic degradation of NP antioxidant. Babaei *et al.*[141] adopted a multivariate approach to study the degradation of NP using ZnO as a photocatalyst. The degradation rate constant was positively correlated with pH values until the pH value increased to 10. This was because a high pH (10) was favorable for the formation of $^·OH$, thus promoting the degradation of NP. The degradation reaction rate increased with the decrease of the initial concentration of NP, and increased with the increase of ZnO content until the ZnO concentration reached 0.5 g L^{-1}. Bechambi and co-workers[142] demonstrated that doping Ag ions into a ZnO matrix could shift the absorption edge, increase the specific surface area, reduce the e^-–h^+ recombination and decrease the band gap of ZnO. And under optimum conditions, Ag–ZnO achieved 88% TOC conversion and 100% degradation efficiency for NP.

4.3 Bisphenol A plasticizer

BPA is a kind of chemical with high production and consumption. It is a synthetic monomer widely used in the production of thermal receipt paper, dental sealants, epoxy resin linings of beverage containers, and PC plastics.[143] At the same time, it is also recognized as an endocrine disruptor that is harmful to the human body and the environment. BPA discharged into the environment mainly comes from incomplete removal during wastewater treatment, landfill leachate, treatment of BPA during the manufacturing process, and leaching of discarded BPA-containing substances (*e.g.* hydrolysis of PC and recycled paper).[144] At present, there are many technical means of investigating the removal of BPA from the environment, including reverse osmosis, nanofiltration, membrane bioreactors, ozone, *etc.*[145–149] However, these methods have their own disadvantages. For example, the use of ozonation technology to remove BPA requires a large investment to generate O_3, and may also produce some carcinogenic intermediates.[150] BPA can be removed effectively by chlorination, but the chlorinated derivatives formed during the reaction show more toxic effects than BPA.[151] Among the various strategies, the photocatalytic technology shows excellent performance in the degradation of BPA. In the following sections, we will selectively discuss several types of photocatalyst including Bi-based, Ag-based and g-C_3N_4-based photocatalysts. Herein, various photocatalysts for degradation of BPA are generally summarized in Table 2.

4.3.1 Bi-based photocatalysts for BPA degradation. Bi-based photocatalysts are popular photocatalysts with a wide variety, including Bi^{3+}-containing compounds such as $BiPO_4$, Bi_2WO_6, $BiFeO_3$, $Bi_2O_2CO_3$, $Bi_{12}TiO_{20}$, $Bi_4Ti_3O_{12}$, Bi_2O_3, $BiVO_4$, Bi_3TiNbO_9, $Bi_{0.5}K_{0.5}TiO_3$ and BiOX (X = Cl, Br, I). Most of these Bi^{3+}-containing photocatalysts have a plate-like appearance and a layered structure. In addition, there are some photocatalysts containing Bi^{5+} such as $NaBiO_3$, $LiBiO_3$ and $KBiO_3$. Due to the instability of Bi^{5+}, there are relatively few reports on this type of

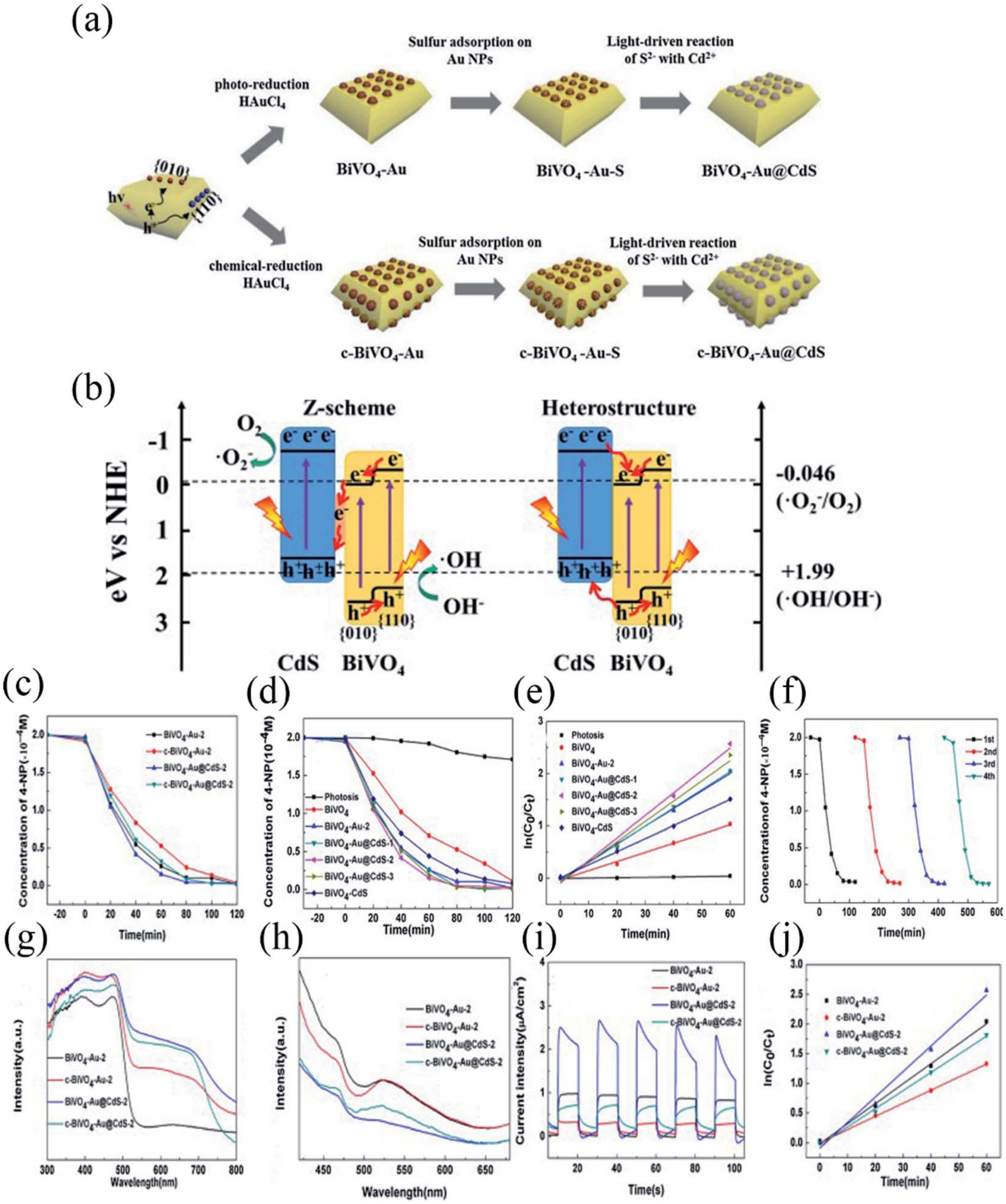

Fig. 10 (a) Schematic illustration for the preparation of ternary $BiVO_4$–Au@CdS, (b) proposed photocatalytic mechanisms of the CdS–Au–$BiVO_4$ Z-scheme and CdS–$BiVO_4$ heterostructure, (c and d) concentration of 4-NP *versus* time plots, (e) degradation kinetics of 4-NP during the photocatalytic process on different photocatalysts under visible light irradiation ($\lambda \geq 420$ nm), (f) the stability test of the $BiVO_4$–Au@CdS-2 photocatalyst in the recycling reactions for the degradation of 4-NP, (g) UV-vis absorption spectra, (h) photoluminescence spectra and (i) photocurrent responses of $BiVO_4$–Au-2, c-$BiVO_4$–Au-2, $BiVO_4$–Au@CdS-2 and c-$BiVO_4$–Au@CdS-2, and (j) degradation kinetics of 4-NP during the photocatalytic process on different photocatalysts under visible light irradiation ($\lambda \geq 420$ nm). Reproduced with permission from ref. 140. Copyright 2017, Elsevier.

photocatalyst.[152] Bi-based photocatalysts are widely used for photocatalytic degradation of BPA including Bi-based multicomponent oxides, bismuth subcarbonate, BiOX, $Bi_xO_yX_z$, *etc.*

Bi-based multi-component oxides are a type of oxysalt, including Bi_2WO_6, Bi_2MoO_6, $Bi_4Ti_3O_{12}$, $BiVO_4$, *etc.*, usually composed of Bi_2O_3 and various metal oxides such as V_2O_5, Mo_2O_3, TiO_2, *etc.* with a layered Aurivillius structure. That is, the $[Bi_2O_2]^{2+}$ layer interacts with the metal oxide layer grown along the *c*-axis.[153] Yu *et al.*[154] prepared a series of fluorinated Bi_2MoO_6 photocatalysts with different atomic ratios of F to Bi for degradation of organic pollutants including BPA under different light irradiation sources. The mineralization rate of $F_{0.20}$–Bi_2MoO_6 to BPA reached 77.81%, 67.11%, and 41.2% and the removal rate of BPA reached 98.3%, 87.9% and 74.7% under UV-vis, UV, and vis light irradiation, respectively. F doping could reduce the size of Bi_2MoO_6 crystals and increase their crystallinity, which would

Table 2 A summary of degradation of BPA over various photocatalysts

Photocatalysts	Light source, λ (nm)	BPA concentration	Reaction time (min)	Degradation efficiency	TOC removal efficiency	Kinetics	Ref.
(A) Bismuth-based							
Co-Doped BiOCl	A 500 W Xe arc lamp, $\lambda > 420$ nm	10 mg L^{-1}	120	95%	—	Pseudo-first-order	198
I-Deficient BiOI	An 800 W xenon lamp	10 mg L^{-1}	30	Almost 100%	—	—	102
$Bi_4O_5I_2$–Bi_5O_7I	A 500 W Xe lamp, $\lambda > 420$ nm	10 mg L^{-1}	240	94%	—	—	168
$Bi_{12}O_{17}Cl_2$ nanobelts	A 500 W Xe arc lamp, $\lambda > 420$ nm	10 mg L^{-1}	120	95%	50%	Pseudo-first-order	170
F–Bi_2MoO_6	A 500 W xenon lamp, $\lambda \leq 400$ nm	20 mg L^{-1}	100	98.3%	77.81%	Pseudo-first order	154
Iodide-modified $Bi_4O_5Br_2$	A 500 W Xe lamp, a 420 nm cut-off filter	15 mg L^{-1}	120	95%	72.7%	—	171
$BiOIO_3$	A 1000 W xenon lamp, $\lambda > 420$ nm	10 mg L^{-1}	60	93.1%		Pseudo-first-order	199
BN/$Bi_4O_5I_2$	A 300 W Xe lamp, a 400 nm cut-off filter	10 mg L^{-1}	20	97%	—	—	200
BiOCl	A 300 W Hg arc lamp, UV light	1×10^{-5} M	360	96%	96% (13 h)	—	162
CuO_x/$BiVO_4$	A 100 W xenon ozone-free lamp, a filter with a 420 nm cut-off	210 μg L^{-1}	180	85%	—	—	155
Fe_3O_4/BiOI	An 800 W xenon lamp, a 420 nm cut-off filter	—	90	100%	—	Pseudo-first-order	167
$Bi_2O_2CO_3$/Bi_2O_4	A 500 W halogen lamp, 420 nm $< \lambda <$ 800 nm	20 mg L^{-1}	20	100%	—	—	159
$Bi_7O_9I_3$	A 500 W iodine tungsten lamp, a 400 nm cutoff filter	20 mg L^{-1}	360	95%	—	—	169
$BiOBr_{0.75}I_{0.25}$/$BiOIO_3$	A 300 W xenon lamp, $\lambda > 420$ nm	10 mg L^{-1}	120	85.2%		Pseudo-first-order	201
Bi–BiOI	A 500 W Xe lamp, a cut-off filter blocking ultraviolet light	10 mg L^{-1}	240	86%	—	—	161
Bi–$Bi_4O_5I_2$	A 350 W Xe lamp, a 420 nm ultraviolet cut-off filter	20 mg L^{-1}	15	94%	—	—	172
(B) Silver-based							
Ag_3PO_4/$LaCoO_3$	A 300 W Xe lamp, $\lambda \geq 400$ nm	10 mg L^{-1}	40	100%	77.27%	—	202
Ag_3PO_4@P3HT	A 400 W metal halide lamp, $\lambda \geq 420$ nm	20 ppm	10	Almost 100%	—	—	177
Ag_2WO_4/Ag_3PO_4	A 350 W Xe lamp	20 mg L^{-1}	10	93%	75% (30 min)	Pseudo-first-order	175
AgI/Ag_2WO_4	A 150 W Xe lamp, $\lambda > 420$ nm	10 mg L^{-1}	10	100%	91% (60 min)	Pseudo-first-order	186
Ag_2O/$ZnFe_2O_4$	A 300 W Xe lamp, $\lambda > 420$ nm	20 mg L^{-1}	60	92.5%	—	Pseudo-first-order	203
rGH–AgBr@rGO	A 400 W metal halide lamp, a 420 nm cutoff filter	20 ppm	90	100%	—	—	180
Ag_3PO_4/rGH	A 250 W metal halide lamp, $\lambda > 420$ nm	5 ppm	12	100%	—	—	178
Ag/AgBr/$BiOIO_3$	A 500 W Xe lamp, a 420 nm cutoff filter	10 mg L^{-1}	240	70.9%	71.0%	—	185
C_{60}@AgCl-LDO	A 300 W xenon lamp, simulated visible light	10 mg L^{-1}	300	90%	—	Pseudo-first-order	204
(C) g-C_3N_4-based							
ZIF-NC/g-C_3N_4	A 300 W xenon lamp, an optical filter ($\lambda >$ 400 nm)	20 mg L^{-1}	60	97%	—	Pseudo-first-order	197
Ag/mpg-C_3N_4	A 300 W Xe lamp, a UV cutoff filter (>400 nm)	20 mg L^{-1}	60	98%	80%	—	205
OA-g-C_3N_4	A 500 W Xe lamp	15 mg L^{-1}	240	100%	56%	—	193
Carbon-doped g-C_3N_4	A 300 W Xe lamp, a 420 nm cut-off filter	5 mg L^{-1}	90	100%	—	—	192
C and O dual-doped g-C_3N_4	A 500 W Xe lamp, a 420 nm cutoff filter	15 ppm	180	55%	52%	Pseudo-first-order	194
Dual-oxygen doped porous g-C_3N_4	A 300 W xenon lamp, 420 nm $\leq \lambda \leq$ 780 nm	20 mg L^{-1}	50	99%	75%	Pseudo-first-order	206
Ag-decorated S doped g-C_3N_4	A 155 W Xe arc lamp, 280 $\leq \lambda \leq$ 630 nm	10 mg L^{-1}	240	78%	—	Pseudo-first-order	207
CeO_2/g-C_3N_4 nanosheets	A 300 W Xe lamp, a cutoff filter (<420 nm)	10 mg L^{-1}	80	93.7%	39.3%	Pseudo-first-order	208
α-Fe_2O_3-DBD/g-C_3N_4	A 500 W Xe lamp	15 ppm	180	91.1%	52.2%	—	209

Table 2 (*Contd.*)

Photocatalysts	Light source, λ (nm)	BPA concentration	Reaction time (min)	Degradation efficiency	TOC removal efficiency	Kinetics	Ref.
g-C_3N_4 nanosheets (with PS addition)	A 150 W xenon lamp, a 400 nm cutoff filter	5 mg L^{-1}	90	Almost 100%	—	Pseudo-first-order	195
g-C_3N_4/PDI@MOF	A 5 W white LED lamp, $280 \leq \lambda \leq 630$ nm	50 ppm, 2 ppm	10	100%	—	—	196

promote the transfer of photo-generated carriers. At the same time, F^- could replace O^{2-} anions to generate O vacancies. F ions and O vacancies could absorb e^-, thereby promoting the separation of photo-generated h^+ and e^-. Due to the low separation effect of photo-generated carriers, the photocatalytic activity of $BiVO_4$ was not high. Kanigaridou *et al.*[155] found that the removal rate of BPA over $CuO_x/BiVO_4$ was 85% after 3 h reaction under irradiation with visible light; due to the p–n heterojunction formed between n-type $BiVO_4$ and p-type CuO (or Cu_2O) semiconductors, the separation of photo-generated carriers was promoted.

Bismuth subcarbonate, a kind of compound with an Aurivillius/Sillén phase, gets lots of attention in the field of photocatalysis due to its low cost, chemical stability, non-toxic nature and remarkable photocatalytic activity.[156,157] Shi *et al.*[158] found that BPA could be degraded effectively by Z-scheme $Bi_2O_2CO_3/Bi/Bi_2WO_6$ composites. The removal rate and the TOC degradation rate of BPA over BOCW-3 were 92.4% and 81.5% within 2 h under simulated solar irradiation. The excellent photocatalytic activity was attributed to the formation of the Z-scheme between the ternary complexes as can be seen in Fig. 11a. Sun *et al.*[159] verified that the $Bi_2O_2CO_3/Bi_2O_4$ photocatalyst showed excellent performance in the degradation of BPA because the heterojunction formed between Bi_2O_4 and $Bi_2O_2CO_3$ could effectively enhance the separation efficiency of photo-generated e^- and h^+.

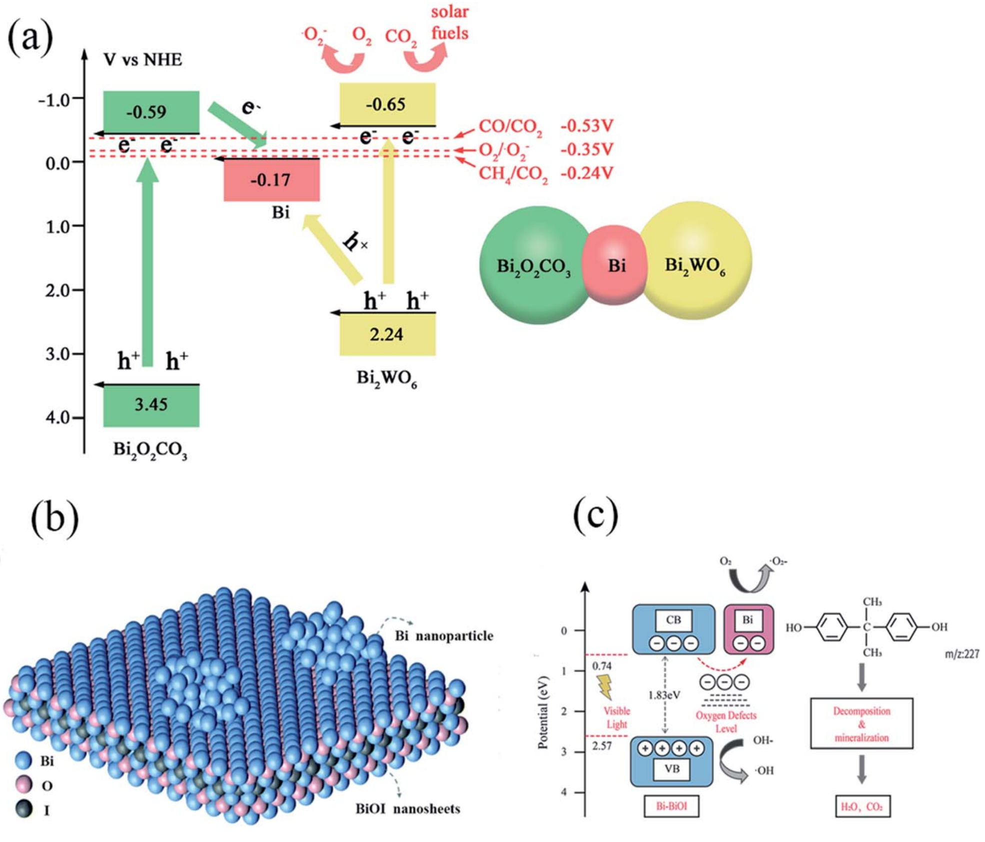

Fig. 11 (a) Possible mechanism for organic pollutant photodegradation by the BOCW composite under simulated solar irradiation. Reproduced with permission.[158] Copyright 2018, Elsevier. (b) Schematic diagram of the atomic structure of Bi–BiOI. (c) Proposed photodegradation process in Bi–BiOI under visible light irradiation. Reproduced with permission from ref. 161. Copyright 2017, The Royal Society of Chemistry.

BiOX are Bi-based photocatalysts, including BiOF, BiOBr, BiOI and BiOCl, with a layered structure characterized by $[Bi_2O_2]$ slabs interleaved by double slabs of halogen atoms.[160] The formation of an internal electric field between the X^- layers and the $[Bi_2O_2]^{2+}$ layers can effectively facilitate the separation of photo-generated e^- and h^+, thus improving the photocatalytic activity.[153] The existence of defects will significantly change the physical and chemical properties and photoelectric properties of the photocatalysts. Zhu and co-workers[102] synthesized an I-deficient BiOI thin film *via* a solvothermal approach. The generated I vacancies could effectively trap h^+, thereby inhibiting the e^-–h^+ recombination. Compared to BiOI powder, it performed better in the degradation of BPA. Luo *et al.*[161] prepared Bi–BiOI with Bi nanodots deposited on BiOI for enhanced photocatalytic BPA degradation (Fig. 11b). Under the same experimental conditions, the removal rate of BPA from Bi–BiOI was 1.6 times higher than that of BiOI. This was mainly due to the existence of O vacancies promoting the generation and separation of photo-generated e^- and h^+, and Bi–BiOI has a lower VB and thus has a stronger oxidizing ability. Both were also beneficial for the generation of free radicals (Fig. 11c). Guo *et al.*[162] used two types of BiOCl nanosheet with different thicknesses but similar exposed surfaces and morphologies to prepare nanostructures (BiOCl-1 and BiOCl-2; the nanosheets of BiOCl-1 were thinner than those of BiOCl-2). The positron annihilation experiments indicated that BiOCl-1 possessed larger vacancies than BiOCl-2. The results showed that after 6 h of UV light irradiation, 96% of BPA could be removed by BiOCl-1, while 55% of BPA could be removed by BiOCl-2. When light illumination was extended to 13 h, the removal rate of BPA over BiOCl-1 was 96%, while only 35% TOC could be reduced by BiOCl-2. DFT calculations revealed that the presence of mesopores promoted the formation of large vacancies, which could counterbalance the thermodynamic instability caused by Bi and O atoms. It is well known that a variety of semiconductors with matching energy band gaps are joined to form a heterojunction. The synergistic effect between the semiconductors and the contact between the surfaces make its photocatalytic performance better than that of a single photocatalyst.[163] $SrTiO_3$ is a typical n-type photocatalyst with excellent photocatalytic activity, but its light absorption range is limited to UV light. Niu *et al.*[164] fabricated a p–n heterostructure *via* combining $SrTiO_3$ with BiOI. The degradation rate of BPA was almost 3 times that of BiOI with an optimum loading of $SrTiO_3$ in the $SrTiO_3$/BiOI composite. Li *et al.*[165] prepared p–n heterojunction BiOCl–CuO_x (BC-x, $x = 1$, 2 and 3) photocatalysts with different amounts of CuO. During the reaction, almost no degradation of BPA was achieved by pure BiOCl, while the best degradation rate (98.42%) and removal rate (98.86%) for BPA were observed over BC-2. In addition, there are also studies on the degradation of BPA by ternary photocatalytic compounds. Hu *et al.*[166] found that photocatalysts formed by supporting carbon quantum dots (CQDs) on BiOCl/BiOBr had a stronger catalytic activity than BiOCl/BiOBr. The separation efficiency of photo-generated e^-–h^+ pairs and visible light absorption were enhanced due to the introduction of CQDs. The application of nanoparticles has the disadvantage of them being difficult to recycle, so it is a research hotspot to prepare photocatalysts with magnetic properties for easy recycling. Gao and co-workers[167] prepared a series of three-dimensional microsphere shaped heterojunction photocatalysts (Fe_3O_4/BiOI) with different molar mass ratios. Fe_3O_4/BiOI (FB-4) with a 1 : 4 molar mass ratio showed the most excellent photocatalytic performance among all the tested photocatalysts. The reaction rate constant for FB-4 was about 4 times higher than that of FB-1 and 1.7 times that of BiOI. Almost all BPA could be removed within 1.5 h. When Fe_3O_4 was hybridized with BiOI, a p–n heterojunction and an internal electric field between BiOI and Fe_3O_4 was formed. The e^- in the CB of Fe_3O_4 were transferred to BiOI, and the h^+ in the VB were transferred to Fe_3O_4. This would cause the photo-generated carriers to migrate rapidly and reduce the recombination rate of h^+ and e^-.

$Bi_xO_yX_z$ photocatalysts, including Bi_5O_7Br, $Bi_7O_9I_3$, $Bi_4O_5Br_2$, $Bi_{12}O_{17}Cl_2$, $Bi_4O_5I_2$, $Bi_{24}O_{31}Br_{10}$, *etc.*, have layer structures with weak interlayer nonbonding and strong interlayer bonding interactions. Similar to BiOX, $Bi_xO_yX_z$ has a more negative VB position.[160] Huang *et al.*[168] used BiOI as a template to prepare three-dimensional (3D) hierarchical BiOI, $Bi_4O_5I_2$, Bi_5O_7I and $Bi_4O_5I_2$–Bi_5O_7I phase-junction at different reaction temperatures (Fig. 12a). The experimental results showed that $Bi_4O_5I_2$ exhibited the best performance as a single photocatalyst, and $Bi_4O_5I_2$–Bi_5O_7I had the strongest photocatalytic activity among all prepared samples owing to the fabrication of an energy–structure matchable heterojunction (Fig. 12b), which promoted the separation and transfer of charges. Zhao *et al.*[169] prepared I-deficient bismuth oxyiodides (Bi_5O_7I, $Bi_7O_9I_3$, and $Bi_4O_5I_2$) by adjusting the solution pH value during preparation (Fig. 12c). $Bi_7O_9I_3$ showed the best photocatalytic performance reaching 95% removal efficiency for BPA under 6 h of light due to appropriate band structures, good visible-light absorption and low electrochemical impedance. Visible-light responsive $Bi_{12}O_{17}Cl_2$ nanobelts were synthesized through a solvothermal route. $Bi_{12}O_{17}Cl_2$ showed significantly enhanced photoreactivity compared to BiOCl and was also better than the classic photocatalyst TiO_2 (P25) owing to the efficient visible light absorption.[170] Modifying the surface of the photocatalyst is a feasible method to improve photocatalytic performance. Zhang *et al.*[171] verified that using I to modify $Bi_4O_5Br_2$ could change its band gap. The removal and the TOC removal rate of BPA over BOB-3 (the molar ratio of KI to KBr was 1.5) were 95% and 72.7% after 2 h visible-light irradiation. Also, it had good stability after several cycles. Bi-modified $Bi_4O_5I_2$ with O vacancies showed enhanced photocatalytic BPA degradation, which could be attributed to the enhanced visible light absorption due to the Bi metal and the synergistic effect of the O vacancies and Bi metal on trapping e^-.[172]

4.3.2 Ag-based photocatalysts for BPA degradation. Ag based photocatalysts, such as Ag_3PO_4, AgCl, *etc.*, are also often used in the photocatalytic degradation of BPA, but due to their fast photogenerated carrier recombination and photocorrosion, their performance is not very outstanding. Constructing heterojunctions, core–shell structures, *etc.* can improve their photocatalytic performance.

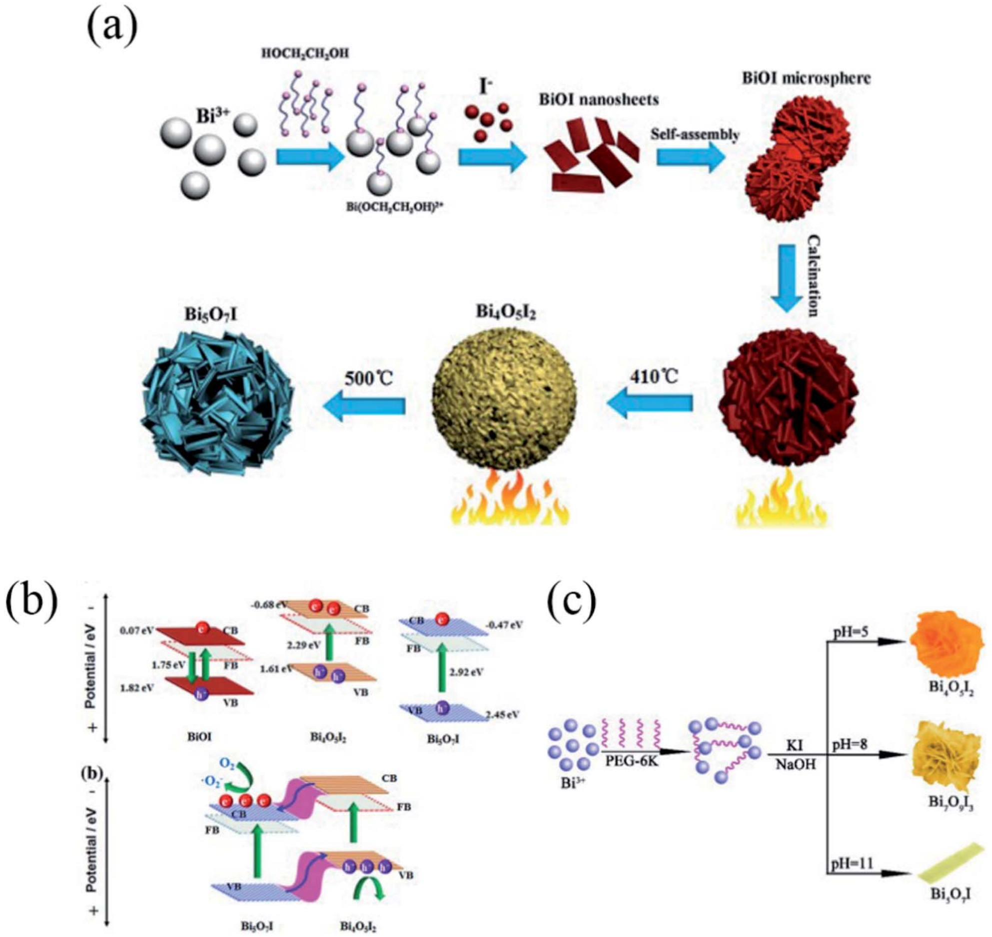

Fig. 12 (a) Formation diagram of the hierarchical architectures of BiOI, $Bi_4O_5I_2$, $Bi_4O_5I_2$–Bi_5O_7I composite and Bi_5O_7I, and (b) formation diagram of the hierarchical architectures of BiOI, $Bi_4O_5I_2$, $Bi_4O_5I_2$–Bi_5O_7I composite and Bi_5O_7I phase junction. Reproduced with permission from ref. 168. Copyright 2016, Elsevier. (c) Schematic illustration of the possible formation mechanism of Bi-based oxyiodides. Reproduced with permission from ref. 169. Copyright 2017, Elsevier.

Ag_3PO_4 is a photocatalyst with a band gap energy of approximately 2.43 eV, and can be excited by visible light. Pure Ag_3PO_4 can absorb sunlight energy with wavelengths below 530 nm.[173] Ag_3PO_4 is a promising photocatalyst for the treatment of environmental pollutants such as Cr(VI), humic acid, dyes, phenol and phenol derivatives, endocrine disrupting compounds, personal care products and pharmaceuticals.[174] Preparing composites of semiconductor photocatalysts and other materials is an effective way to improve the photocatalytic performance. Hybrid photocatalysts tend to perform better than single photocatalysts. Preparation of Ag_3PO_4-based photocatalysts can effectively inhibit photo-generated carrier recombination. Li *et al.*[175] explored the photocatalytic performance of Ag_2WO_4/Ag_3PO_4 under simulated solar light irradiation. With the increase of the molar mass percentage of Ag_2WO_4 in the composite Ag_2WO_4/Ag_3PO_4 photocatalyst, the degradation efficiency of BPA also increased significantly. The efficiency was the highest when the molar mass percentage of Ag_2WO_4 reached 7.5%, and 93% of BPA could be degraded within 10 min. Further increasing the content of Ag_2WO_4 would make it occupy the reactive sites of Ag_3PO_4, thus reducing removal efficiency. The removal rate of TOC was also higher than that with Ag_3PO_4 alone. Ag-based ternary composite photocatalysts have also been studied. Niu *et al.*[176] observed that AgBr/Ag/$PbBiO_2Br$ with an initial amount of $AgNO_3$ of 0.3 mmol (denoted as AgBr/Ag-3/$PbBiO_2Br$) achieved an optimal photocatalytic performance with 82.3% BPA removal rate within 2 h and the kinetic constant (0.0134 min^{-1}) was 4.52 times higher than that of pure $PbBiO_2Br$ (0.0038 min^{-1}). It was attributed to the efficient separation of photo-generated e^-–h^+ pairs and the acceleration of the interfacial electron transfer process.

The construction of core–shell structures can improve the contact between two materials effectively. Conductive polymers can increase the photoelectric conversion efficiency, and most of them have good visible light absorption capacity. Lu *et al.*[177] fabricated Ag_3PO_4@P3HT with a P3HT-coated Ag_3PO_4 core–shell structure. At a loading of 0.07 wt% P3HT, the composite exhibited higher activity which was about 1.4 times that of the Ag_3PO_4 monomer. This was ascribed to the close contact between core–shell composite materials, which increased the charge transfer rate. The 3D network structure of the photocatalyst is conducive to the adsorption and further degradation of pollutants. Graphene is an absorbent with low porosity and high surface area. Two-dimensional graphene nanosheets could be assembled into graphene hydrogel (rGH) with a 3D network structure *via* π–π conjugation. Cui *et al.*[178] ensured 100% removal of BPA within 12 min by using Ag_3PO_4/rGH as a photocatalyst. The unique 3D structure of the composite photocatalyst could effectively adsorb BPA, and the maximum adsorption capacity was more than 2 times those of Ag_3PO_4/Al_2O_3 and Ag_3PO_4/AC. Meanwhile, the Ag_3PO_4 nanoparticles anchored on graphene could further degrade the adsorbed BPA. In the same year, they[179] successfully inserted core–shell AgCl@rGO (graphene) into the 3D structure of graphene hydrogel. The core–shell structure of AgCl@rGO could inhibit the aggregation of AgCl particles and the conversion of AgCl particles to Ag particles, which was beneficial for the separation and transfer of photogenerated carriers. Due to the synergistic effect of photocatalytic degradation and adsorption, the degradation ability of AgCl@rGO-rGH for BPA was more than 2 times and 6 times those of pure rGH and AgCl, respectively. In addition, they synthesized a graphene hydrogel–AgBr@rGO photocatalyst with 3D network structures. Firstly, rGO was wrapped on AgBr to form a AgBr@rGO composite, then the AgBr@rGO was put on a graphene hydrogel to form graphene hydrogel–AgBr@rGO (Fig. 13a). The 3D structure of rGH retained the large accessible to get AgBr@rGO. The presence of rGO in AgBr@rGO not only prevented vitamin C from reducing Ag^+ to Ag^0, avoiding the emergence of a large number of Ag particles, but also changed the morphology of the graphene hydrogel, achieving a more regular and uniform particle size. (Fig. 13c and d). The thickness of the GO films was reduced and a homogeneous distribution of AgBr was accomplished *via* ultrasonication (Fig. 13e and f). Both AgBr and Ag could be excited to generate

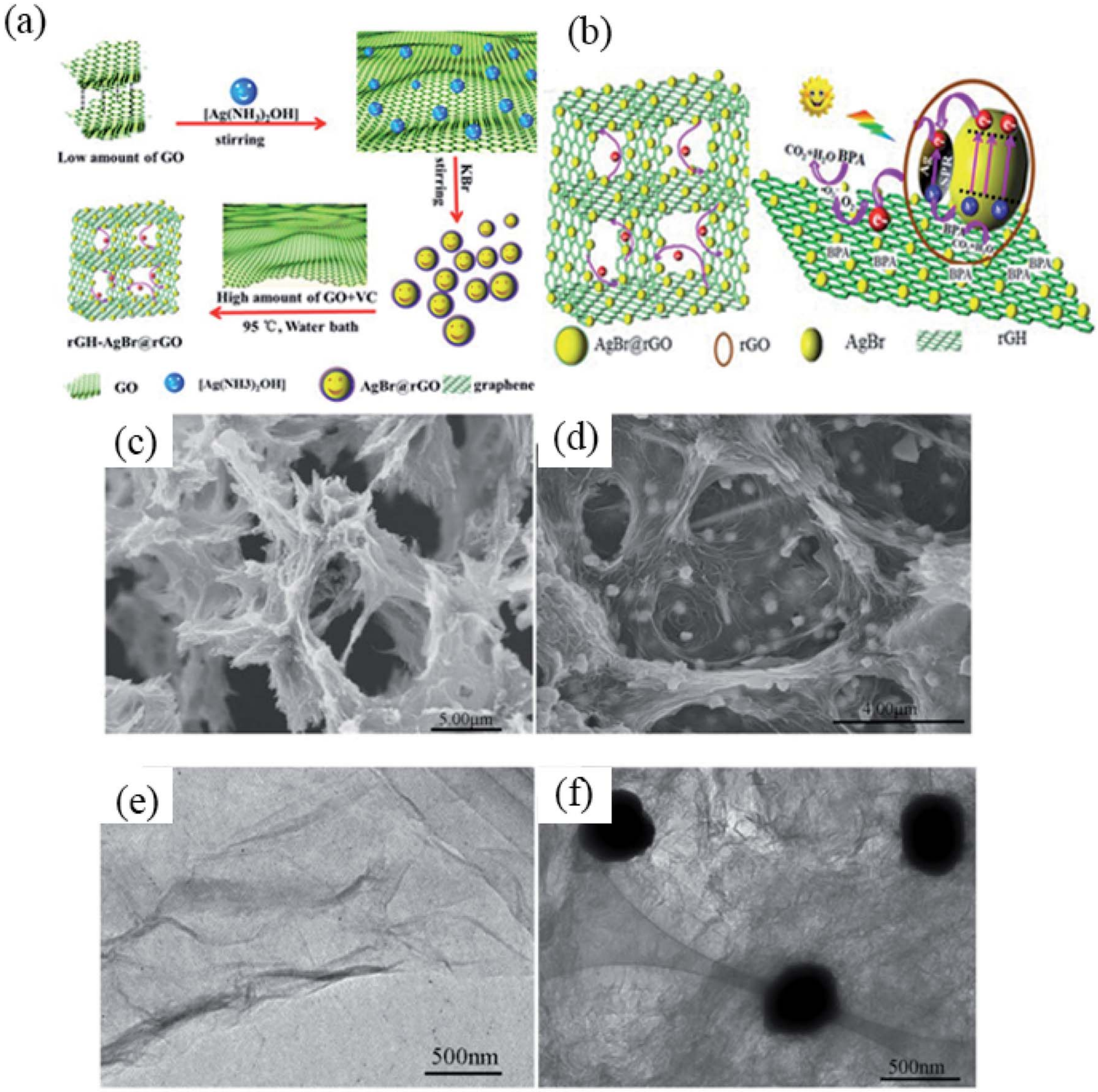

Fig. 13 (a) Schematic synthesis of rGH–AgBr@rGO, (b) proposed mechanism for photocatalytic BPA degradation by rGH–AgBr@rGO under visible-light illumination, (c) SEM images of rGH and (d) 10% rGH–AgBr@rGO, and (e) TEM images of GO and (f) 10% rGH–AgBr@rGO. Reproduced with permission from ref. 180. Copyright 2017, Elsevier.

e^- and h^+ under visible light irradiation. The h^+ could react with H_2O to generate $^{\bullet}OH$ for BPA degradation, or reacted directly with BPA. Electrons could be quickly transferred to the surface through rGO, and they further migrated to the surface of rGH, and reacted with O_2 to generate $^{\bullet}O_2^-$. rGH could effectively inhibit the recombination between e^- and h^+ and π–π conjugation enabled BPA adsorption (Fig. 13b). The BPA removal efficiency of 10% rGH–AgBr@rGO was 1.5 times that of pure AgBr. The composite photocatalyst retained a high degradation ability even after repeated cycling.[180]

Many studies have confirmed that Z-scheme photocatalysis has great potential in improving the photocatalytic performance. In the Z-scheme system, the photoinduced h^+ from the VB of photocatalyst PS I can combine with the e^- from the CB of photocatalyst PS II, thus enhancing the separation efficiency of photo-generated carriers and improving the redox ability of the photocatalytic system. Mei and co-workers[181] reported that Ag_3PO_4/g-C_3N_4 (APC) exhibited excellent photocatalytic activity compared to g-C_3N_4 and Ag_3PO_4. APC-25 (mass ratio of Ag_3PO_4 was 25%) exhibited 90% BPA removal efficiency with visible light on in 3 h, which could be attributed to the low recombination of photo-generated h^+ and e^-. Sun *et al.*[182] successfully modified the surfaces of Ag_3PO_4 with numerous g-C_3N_4 nanocrystals, forming g-C_3N_4/Ag_3PO_4 (CN/APO) hybrid photocatalysts; the degradation ratio of BPA over bulk-g-C_3N_4/APO-20 was about 65% after 45 min of reaction, while that over the CN/APO-20 hybrid (mass ratio = 1 : 4) was about 91%. The reaction rate constant of the former towards BPA degradation was also much lower than that of the latter. Under irradiation by visible light, due to the short distance between the VB of g-C_3N_4 and CB of Ag_3PO_4, e^- on the CB of Ag_3PO_4 transferred to the VB of g-C_3N_4 and recombined with the above h^+, which promoted the separation of photo-generated carriers while maintaining the strong redox capacity of the system. Besides, the dual Z-scheme PANI/Ag_3PO_4/$NiFe_2O_4$ composite prepared by Chen *et al.* exhibited excellent visible-light photocatalytic activity towards BPA elimination.[183] The double Z-scheme heterojunction structure inhibited the recombination of photo-generated e^- and h^+ pairs with stronger redox.

Using the surface plasmon resonance (SPR) strategy is also an effective method to improve photocatalytic activity. Ag/AgX (X = I, Br, Cl) is a widely used dopant to modify other photocatalysts. The highly dispersed AgX can promote the dispersion of photo-generated carriers, and at the same time, metallic Ag nanoparticles are able to absorb visible light efficiently. Yang *et al.*[184] selected $SrTiO_3$ nanocubes as an applicable support and decorated them with Ag/AgCl nanoparticles as photocatalysts. It was observed that at a 0.216 : 1 mass ratio of Ag to $SrTiO_3$, the Ag/AgCl/$SrTiO_3$ (21.6%) composite photocatalyst exhibited 83% BPA removal efficiency under visible light illumination for 4 h. This was credited to the efficient charge separation and strong visible light absorbance due to the SPR effect. The unique structure of $BiOIO_3$ endowed it with excellent photocatalytic performance and outstanding performance in pollutant degradation. However, it only responds to UV light. In order to overcome this disadvantage, Chen *et al.*[185] combined $BiOIO_3$ with Ag/AgBr, which has been proven to have a good response to visible light. It was found that at a KBr/$BiOIO_3$ molar ratio of

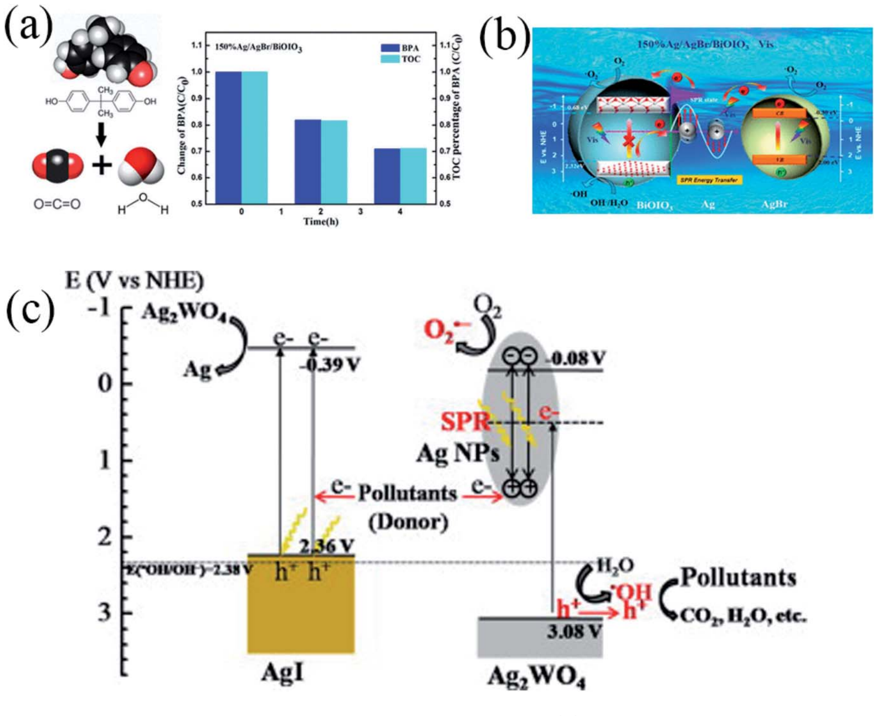

Fig. 14 (a) Photocatalytic degradation efficiency and TOC percentage of BPA, and (b) schematic diagrams for charge-transfer mechanisms of 150% Ag/AgBr/$BiOIO_3$ under visible light (λ > 420 nm). Reproduced with permission from ref. 185. Copyright 2017, American Chemical Society. (c) Proposed photocatalytic mechanism for AgI/Ag_2WO_4. Reproduced with permission from ref. 186. Copyright 2019, Elsevier.

1.5 : 1, the resultant composite photocatalyst (denoted as 150% Ag/AgBr/$BiOIO_3$) removed 70.9% BPA and 71% of its TOC in 4 h under visible light illumination (Fig. 14a). This was ascribed to the synergistic effect of fabrication of a heterojunction and Ag nanoparticle SPR effect (Fig. 14b). Ag showing an SPR effect can also be produced in some Ag-based photocatalytic systems. Zhang *et al.*[186] observed higher photocatalytic activity towards BPA over AgI/Ag_2WO_4 suspension (100% removal rate within 10 min) compared to Ag_2WO_4, AgI, $TiO_{2-x}N_x$, and AgI + Ag_2WO_4 (0%, 24%, 36%, and 53% removal rates within 1 h) and more than 91% of the TOC was removed in 1 h. The reaction rate constant of AgI/Ag_2WO_4 (0.3722 min^{-1}) was 39, 52 and 91 times those of AgI + Ag_2WO_4 (0.0095 min^{-1}), $TiO_{2-x}N_x$ (0.0072 min^{-1}) and AgI (0.0041 min^{-1}), respectively. Due to the SPR effect of the formed Ag, the degradation rate of BPA at longer wavelengths was faster than that at shorter wavelengths (the electron-losing self-oxidation, oxidation of $^{\bullet}OH$ and h^+ on Ag_2WO_4 and SPR of the *in situ* formed Ag NPs collectively contributed to the high photocatalytic activity (Fig. 14c)).

4.3.3 $g\text{-}C_3N_4$-based photocatalysts for BPA degradation.

$g\text{-}C_3N_4$ is a popular and widely used photocatalyst, but its quantum efficiency is low because of its high photogenerated carrier recombination rate and slow charge mobility.[32,36] Tailoring $g\text{-}C_3N_4$ photocatalysts with enhanced charge separation, surface area, and optical properties for photocatalytic degradation of BPA, such as forming a Z-scheme photocatalysis system, combining with other photocatalysts, *etc.*, is a hot topic of recent research.

Z-scheme photocatalysis systems have also been applied in $g\text{-}C_3N_4$-based photocatalysis, such as the Ag_3PO_4/$g\text{-}C_3N_4$ composite photocatalysts mentioned in the previous section. Wang *et al.*[187] examined the degradation performance of BPA over aldehyde-functionalized $\alpha\text{-}Fe_2O_3$/$g\text{-}C_3N_4$ ($\alpha\text{-}Fe_2O_3$-DBD/$g\text{-}C_3N_4$) with varying weight percentage of $\alpha\text{-}Fe_2O_3$ nanoparticles. The hybrid photocatalyst containing 1.6% $\alpha\text{-}Fe_2O_3$ loading (1.6% $\alpha\text{-}Fe_2O_3$-DBD/$g\text{-}C_3N_4$) exhibited the highest photocatalytic activity and showed higher photocurrent than that of $g\text{-}C_3N_4$ (Fig. 15b), reaching 91.1% BPA (Fig. 15c) removal within 3 h reaction, much higher than that of 1.6% $\alpha\text{-}Fe_2O_3$/$g\text{-}C_3N_4$,

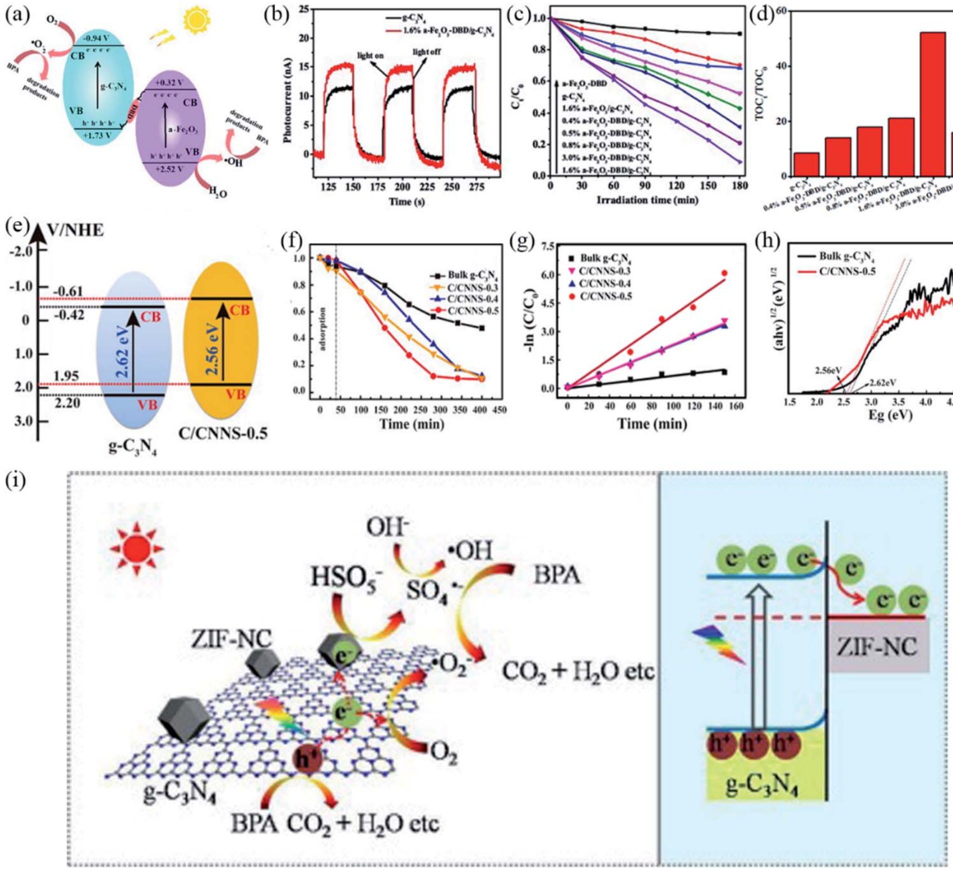

Fig. 15 (a) Proposed photocatalytic degradation mechanism of BPA over $\alpha\text{-}Fe_2O_3$-DBD/$g\text{-}C_3N_4$, (b) photocurrent spectra of $g\text{-}C_3N_4$ and 1.6% $\alpha\text{-}Fe_2O_3$-DBD/$g\text{-}C_3N_4$, (c) BPA degradation by different $\alpha\text{-}Fe_2O_3$-DBD/$g\text{-}C_3N_4$ photocatalysts, and (d) the TOC removal ratio of BPA over $g\text{-}C_3N_4$ and x $\alpha\text{-}Fe_2O_3$-DBD/$g\text{-}C_3N_4$. Reproduced with permission from ref. 187. Copyright 2019, Elsevier. (e) The band structure diagrams of bulk $g\text{-}C_3N_4$ and C/CNNS-0.5 photocatalysts, (f) photocatalytic performance and (g) kinetic linear simulation curves of BPA by bulk $g\text{-}C_3N_4$ and C/CNNS-x (x = 0.3, 0.4, 0.5) photocatalysts, and (h) the band gap plots of bulk $g\text{-}C_3N_4$ and C/CNNS-0.5 photocatalysts. Reproduced with permission from ref. 192. Copyright 2018, Elsevier. (i) Proposed photocatalytic degradation mechanism of BPA over ZIF-NC/$g\text{-}C_3N_4$. Reproduced with permission from ref. 197. Copyright 2018, Elsevier.

showing a mineralization rate 6.14 times (Fig. 15d) that of BPA over g-C_3N_4. This was ascribed to the higher redox potential and the enhanced charge separation efficiency due to the Z-scheme system (Fig. 15a). N-doped graphene aerogel (NGA), which has good electron transfer properties and mechanical strength, is often used as a catalyst support. Chen *et al.*[188] observed higher photocatalytic activity towards BPA removal over Ag/AgBr/g-C_3N_4@NGA compared to g-C_3N_4@NGA, reaching 92% after 2 h irradiation. After repeated use, it still maintained high photocatalytic activity (>80%). The functional and structural merits of g-C_3N_4 and Ag/AgBr in NGA, the strong anchoring effect of chitosan for AgBr nanoparticles and the desirable mechanical strength of NGA were cited as the reasons behind the excellent photocatalytic performance.

If a photocatalytic system can be designed to achieve both the degradation of pollutants and the evolution of H_2 at the same time, the efficiency of separating photo-generated carriers and the quantum efficiency of the photocatalyst will also be improved. CdS is a visible-light catalyst with a mild band gap (2.4 eV), but its aggregation, poor photo-stability, and high photo-generated electron–hole pair recombination rate hinder its photocatalytic applications.[189] Jiang *et al.*[190] prepared CDs/CdS/GCN nanocomposites, achieving H_2 evolution coupled with photodegradation of organic pollutants. In the presence of BPA, the rate of H_2 production was almost two times higher than that in pure water, and the degradation rate of BPA was 72% over the 3% CDs/10% CdS/GCN composite. Wu and coworkers[191] successfully fabricated petal-like CdS nanostructures coated with S-doped C_3N_4 (SCN). The best activity was observed from CS5 which was prepared by adding 50 mg exfoliated SCN during the synthetic process. In the degradation of BPA, the reaction rate of CS5 was about an order of magnitude higher than that of the exfoliated SCN and the degradation efficiency was 3.61 and 9.00 times higher than those of CdS and exfoliated SCN. This was credited to the enhanced separation of charge carriers, due to the existence of heterojunction interfacial structures between exfoliated SCN and CdS.

Element doping can effectively adjust the luminescent, electronic and optical properties of g-C_3N_4. Research on element-doped g-C_3N_4 photocatalysts is in an ascending stage with increasing achievements. Wang *et al.*[192] synthesized a series of C-doped g-C_3N_4 ultrathin nanosheets and found that the C/CNNS-0.5 sample, which was prepared by adding agar and deionized water with a mass ratio of 0.5, showed the highest activity. It completely removed all BPA in 1.5 h, the removal efficiency was more than 2 times that of bulk g-C_3N_4 (Fig. 15f), and the reaction rate constant was close to 6 times that of bulk g-C_3N_4 (Fig. 15g). Meanwhile, the CB and VB values of C/CNNS-0.5 were more negative than those of bulk g-C_3N_4, and the band gap was relatively narrower (Fig. 15h and e). More active sites provided by the 2D nanosheet structure, enhanced visible-light harvesting ability and charge separation of photogenerated carriers were proposed to be the reasons behind the excellent activity. In the investigation of O-doped porous g-C_3N_4 (x OA-g-C_3N_4) for BPA degradation by Qiu *et al.*,[193] 40% OA-g-C_3N_4 achieved 100% removal efficiency of BPA within 3 h and 56% mineralization rate of BPA under 4 h visible light irradiation. O doping could change the position of the CB and VB of g-C_3N_4, the band gap edge was narrowed, the light absorption threshold was expanded to 700 nm and the photocatalytic degradation mechanism was changed. Simultaneously, more light could be absorbed due to the porous structure with a multiple-reflection effect and high specific surface area. Dual-doping can improve optical and structural properties. Gu *et al.*[194] fabricated a series of C and O dual-doped g-C_3N_4 (MACN) and evaluated the photocatalytic activity for BPA degradation. 1MACN, which was prepared by adding an equal weight of urea and malonic acid during the preparation process, showed the highest activity under visible light irradiation. The reaction rate constant of 1MACN and the initial degradation rate of BPA reached 1.1480 min^{-1} and 0.0863 mmol $g_{cat}{}^{-1}$ h^{-1}, respectively. O doping expanded the 1MACN absorption threshold to the visible light region, which would facilitate the generation of photo-generated carriers. At the same time, N doping could limit the recombination of photo-generated carriers.

Some salts, such as persulfate (PS), can be activated by heat, UV light and transition metals to produce $^{\bullet}OH$ and $SO_4{}^{2-}$ with strong redox ability. Metal-free catalysts for peroxymonosulfate (PMS) and PS activation are popular because they are inexpensive and don't cause any secondary pollution. Liu *et al.*[195] reported that the photocatalytic efficiency of g-C_3N_4 nanosheets was higher than that of bulk g-C_3N_4 towards BPA degradation. The addition of PS would further improve the photocatalytic performance. The promoted photocatalytic activity was credited to the fact that PS could be used as an electron trapping agent to promote the separation of photo-generated carriers. Metal–organic frameworks (MOFs) have become the focus of attention because of their adjustable structural composition, and high porosity and surface area. Fe-based MOFs have a wide absorption range in the visible region. Li *et al.*[196] successfully prepared heterojunctions with NH2-MIL-53 (Fe) and pyromellitic diimide g-C_3N_4 (g-C_3N_4/PDI) combined, named CPM. CPM-2 (50%) formed by adding g-C_3N_4/PDI with a mass ratio of 50% during the synthesis process showed excellent performance, achieving 100% degradation efficiency for BPA within 10 min. This could be due to the widened visible light absorption range of g-C_3N_4/PDI after introduction of Fe-MOF and the enhanced separation of photo-generated carriers due to the formation of a heterojunction between NH2-MIL-53 (Fe) and g-C_3N_4/PDI. The carbon materials derived from MOF have abundant active sites, large surface area and hierarchical porous structures, and the MOF-derived N doped porous C obtained *via* thermal treatment could trigger the transition of the PMS response to $SO_4{}^{\bullet -}$. There exists a study that links MOF and PMS to form a new catalyst for g-C_3N_4. Gong *et al.*[197] studied the degradation of BPA by a MOF (ZIF-8)-derived N-doped C modified g-C_3N_4 composite (ZIF-NC/g-C_3N_4) in the presence of PMS under visible light. The results showed that the apparent rate constant for the degradation of BPA by ZIF-NC/g-C_3N_4 with PMS was nearly 9 times that of pure g-C_3N_4. A Schottky type heterojunction between ZIF-NC and g-C_3N_4 was proposed to explain the result (Fig. 15i). The photo-generated e^- from g-C_3N_4 excited by visible light could travel across the interface between ZIF-NC and g-C_3N_4 and then react with PMS to produce $SO_4{}^{\bullet -}$ radicals. At the same time, the e^-

transferred to the surface of g-C_3N_4 could convert O_2 to $^{\bullet}O_2^-$ radicals, which could decompose the BPA rapidly.

4.4 Brominated flame retardants

PBDEs are a kind of hydrophobic substance with many formulations, which play the role of flame retardant in plastic products. There are three formulations widely used in commercial applications called penta-, octa- and deca-BDEs. These additives are widely present in environmental media and cause great harm to human health.[135,210] In the past few decades, these pollutants have been detected in almost all environmental compartments. The increasing level of PBDEs in the environment and especially human tissues is alarming due to their potential cancer proliferation, neurological effects and thyroid hormone imbalance.[211,212]

Hexabromocyclododecane is an important brominated flame retardant used in polystyrene insulation materials, electrical equipment enclosures and decorative materials.[213] HBCDs are found in extruded PS (XPS) and expanded PS (EPS) up to 4–7% by weight. HBCD has three dominant stereoisomers: α-, β-, and γ-HBCD. These BFRs are recognized as POPs in the Stockholm Convention and the three isomers are subject to authorization in the European Union. HBCDs can induce cancer by causing inappropriate antidiuretic hormone syndrome. Due to their improper disposal and extensive use, their widespread occurrence in various environmental compartments has been well documented. The environmental impact of HBCD has been detected worldwide, with concentrations ranging from ng to μg. Therefore, an urgent need is to improve our understanding of their environmental fate and to develop effective approaches for dealing with the relevant environmental contamination.[45,214,215]

TBBPA is the most common BFR. It is produced by brominating bisphenol A and constitutes more than half of the BFR market. It is widely used in acrylonitrile butadiene styrene (ABS) and other plastics.[45] As one of the most predominant BFRs, TBBPA has been applied widely in various plastic products, electronics and textiles. It is frequently found in air, house dust, water, soil and sediments, as well as human and animal tissues. And it is regarded as a potential endocrine disruptor due to its similar molecular structure to thyroid hormones. It is urgent for us to find effective approaches for dealing with the relevant environmental contamination.[216,217] There are also many studies on the photocatalytic degradation of TBBPA.

4.4.1 TiO_2-based photocatalysts for BFR degradation. TiO_2 has been widely used in the degradation of PBDEs due to its excellent photocatalytic properties (Table 3). Many studies have been done to study modified TiO_2 for the photocatalytic degradation of PBDEs. For example, metal doped TiO_2 such as Pd/TiO_2, Ag/TiO_2, Pt/TiO_2 and Cu/TiO_2,[218] rGO (reduced graphene oxide)/TiO_2,[219] CuO/TiO_2 nanocomposites,[220] TiO_2–Cu_2O composite films,[221] Ag/TiO_2,[222] and KH570–TiO_2-NT[223] are used for photocatalytic degradation of BDE47, and TiO_2,[224–227] Cu/TiO_2,[228] CuO/TiO_2,[229] AgI–TiO_2,[230] and Pd–TiO_2 (ref. 231) are used for photocatalytic degradation of BDE209. The degradation efficiency of TiO_2 based photocatalysts for PBDE degradation depends on several parameters including photocatalyst concentration, H_2O content, acidity and alkalinity, *etc.*

The photocatalyst concentration has a great influence on the photocatalytic reaction rate. With catalyst loading, heterogeneous photocatalytic reactions show a proportional increase in photodegradation.[232] In order to ensure effective photon absorption and avoid excessive catalyst, an optimal catalyst concentration needs to be determined.[232,233] When the catalyst concentration exceeds the optimal value, the screening effect and opacity play a major role in reducing light utilization efficiency in the aqueous solution.[224,234] Lei *et al.*[235] observed that when the amount of rGO/TiO_2 was increased from 0 to 0.1 g L^{-1}, the efficiency of debromination was significantly improved from 9.0% to 59.4%. However, further increasing the catalyst load led to the decrease of debromination efficiency. This was because the excess photocatalyst would reduce the utilization efficiency of light and light transmittance. Huang *et al.*[224] found a similar pattern, where TiO_2 played dual roles in the degradation of BDE209. The concentration of active species increased with the increase of TiO_2 load; however, higher TiO_2 load would reduce the efficiency of UV light utilization and increase the turbidity of the solution. Thus, when the amount of TiO_2 increased from 0 to 0.1 g L^{-1}, the debromination efficiency increased from 21.2% to 95.6% and then decreased to 41.1% with the TiO_2 load increased to 1.0 g L^{-1} (Fig. 16a). Azri *et al.*[234] observed that the optimal catalyst (Cu/Ni/TiO_2/PVC (5 : 10 : 85)) dosage was 20 mg towards PBDE degradation (Fig. 16b). A higher catalyst dosage would reduce the $^{\bullet}OH$ production, which was used for degradation.

It was shown that the amount of H_2O in the reaction system has a positive or negative impact on the degradation of PBDEs. One study using Ag/TiO_2 for degradation of BDE47 found that Ag^0 could promote electron separation on TiO_2 and transfer electrons to BDE47 for degradation. Before the degradation of BDE47, an induction period was needed for Ag^0 to accumulate the e^-. Increasing the amount of H_2O in the mixtures shortened the induction time and speeded up the degradation of BDE47.[222] Through investigating the photocatalytic degradation of BDE209, Zhang *et al.*[225] found that in a water/THF system (<50%), there was a lower efficiency of debromination finally than in a pure water system (>80%). Huang and co-workers observed the same behavior: the addition of H_2O could promote degradation of BDE209 and the debromination efficiency increased with the increase of H_2O content within 12 h under UV irradiation (Fig. 16c).[224] However, two experiments conducted by Sun and co-workers showed that water had the opposite effect in the degradation process of PBDEs.[226,227] In their first experiment, when the H_2O content increased from 0.1% to 1.0% under anaerobic acetonitrile conditions, the adsorption amount and degradation rate showed a significant decline from 14.2% to 0.5% and 43.6% to 0, respectively. Addition of 1.0% H_2O could stop the degradation process completely on TiO_2 (Fig. 16d); this was because the surface of TiO_2 was highly hydrophilic, while BDE209 was highly hydrophobic. The H_2O adsorbed on the surface of TiO_2 would prevent contact between BDE209 and TiO_2 and further reduced the number of e^- transferred from the TiO_2 CB to BDE209.[227] Moreover, Sun *et al.* pre-adsorbed the BDE209 molecule on the TiO_2 surface to form a micro-environment in an

Table 3 List of various photocatalysts and their photodegradation of PBDEs[a]

Photocatalysts	PBDE congeners	Matrix	Initial concentration of PBDEs	Operating conditions	Results	Ref.
(A) TiO_2-based						
TiO_2	BDE209	0.1% DMSO	75 $\mu g\ L^{-1}$	Preparation of 1% nano-sized TiO_2 solution in 20 mL of 0.1% DMSO at pH 7; irradiation with visible light	Half-life: 3.5 days Kinetics: pseudo-first-order Main mechanism: reductive process	236
TiO_2	BDE209	H_2O with residual THF or H_2O : THF (1 : 1, v/v)	2 mg L^{-1}	100 mL BDE209 (2 mg L^{-1}) + 2 g L^{-1} TiO_2; irradiation with six mercury lamps	Kinetics: majority (>98%) was removed within 4 h in both pure water (treatment) and THF/water (control) systems	225
TiO_2	BDE209	Water: ACN with 1% THF	10 mg L^{-1}	10 mg TiO_2 + 100 mL BDE209 (10 mg L^{-1}) mixed for 1 min ultrasonically; a PLS-SXE300 Xe lamp with a VISREF filter at $340 \leq \lambda \leq 400$ nm	Kinetics: 95.6% (12 h, UV/TiO_2/H_2O) Main mechanism: oxidative process	224
AgI–TiO_2	BDE209	Isopropanol	1×10^{-5} mol L^{-1}	10 mg of AgI–TiO_2 was added to 9.95 mL of BDE209 solution in a Pyrex vessel with 0.05 mL isopropanol added; a PLSSXE300 Xe lamp, $\lambda \geq 420$ nm	Kinetics: 70% (3 h, visible light irradiation), pseudo-first-order Main mechanism: reductive process	230
CuO/TiO_2	BDE15, BDE166, BDE116, BDE75, BDE47, BDE30, BDE99, 2-CH_3–BDE61, BDE209, BDE7	Methanol	10^{-5} mol L^{-1}	10 mg CuO/TiO_2 + 50 mL PBDE in methanol; a PLS-SXE300 Xe lamp equipped with a 365 nm bandpass filter, purged with Ar; magnetically stirred with Ar protection	Kinetics: pseudo-first-order Main mechanism: reductive debromination	229
Cu/TiO_2	BDE209	Methanol	1×10^{-5} mol L^{-1}	Ultrasonically dispersed; magnetically stirred; purged with argon; protected under an argon atmosphere; a 300 W xenon lamp with an infrared cutoff filter and a 360 nm cutoff filter	Kinetics: pseudo-first-order Rate constants: 0.090 min^{-1} for 0.16% Cu/TiO_2 Mechanism: reductive debromination	228
KH570–TiO_2-NT	BDE47	Dichloromethane	10 mg L^{-1}	0.18 g catalysts + 20 mL BDE47; UV radiation (365 nm)	Mechanism: reductive debromination	223
Ag/TiO_2	BDE47	Acetonitrile–water (1 : 1) solvent + methanol	1000 mg L^{-1}	0.5 mL BDE47 added to 0.1 g L^{-1} catalysts; a PLSSXE300 Xe lamp, purged with nitrogen, protected under a nitrogen atmosphere	Kinetics: almost 100% after 13 min of UV irradiation Mechanism: reductive debromination	222
CuO/TiO_2	BDE47, BDE209	Methanol–water (v/v = 7 : 3) + methanol	1000 mg L^{-1}	20 mg catalysts + 0.5 mL BDE47, 20 mg catalysts + 0.5 mL BDE209; ultrasonically mixed; purged with argon; protected under an argon atmosphere; a PLS-SXE300 Xe lamp	Kinetics: 100% within 0.75 min and 7.5 min for BDE209 and BDE47 under UV-irradiation in an anoxic atmosphere, pseudo-first-order Mechanism: reductive process Rate constant: 3.19 and 0.41 min^{-1} for BDE209 and BDE47, respectively	220
(B) Carbon-based						
Ni-g-C_3N_4	BDE47	Methanol/TEA mixture	10 μM	40 mg C_3N_4 + 20 mL of solution containing 10 μM BDE47; purged with argon; a 300 W xenon lamp with a 420 nm long pass filter	Kinetics: 100% (90 min) Debromination efficiency: 45% Mechanism: debromination	242
g-C_3N_4	BDE209	Methanol	1×10^{-5} mol L^{-1}	20 mg g-C_3N_4 + 20 mL solution of BDE209; anoxic conditions; purged with argon; a PLS-SXE300 Xe lamp, $\lambda \geq 360$ nm	Kinetics: 60% (20 min UV irradiation), pseudo-first-order Mechanism: stepwise reductive process Rate constant: 0.057 ± 0.01 min^{-1}	243
Graphene oxide (GO)/Ag_3PO_4	BDE209	Methanol	1 mg L^{-1}	0.1 g GO/Ag_3PO_4 + 100 mL BDE209 + 1 mL methanol; a 500 W Xe lamp ($\lambda \geq 420$ nm)	Kinetics: 97.33% (8 h) Mechanism: multi-electron reduction process	253

Table 3 (*Contd.*)

Photocatalysts	PBDE congeners	Matrix	Initial concentration of PBDEs	Operating conditions	Results	Ref.
Ag@Ag_3PO_4/g-C_3N_4	BDE47	Methanol/ultrapure water = 20 : 80	5 mg L^{-1}	50 mg of catalysts + 100 mL BDE47; a 300 W Xe lamp (λ > 420 nm)	Kinetics: 97.33% (8 h) Mechanism: multi-electron reduction process	254
(C) Others						
Cu_2O@Pd	BDE47	Ethanol/water 50 : 50 (v/v)	15.0 µM	50 mg of Cu_2O@Pd + 50 mL BDE47; a water-cooled 450 W medium-pressure mercury vapor lamp	Kinetics: pseudo-first-order Rate constant: 0.21 h^{-1} Mechanism: reductive photo-debromination	260
Ag-loaded CdS	BDE47	Methanol/water (70 : 30, 100 mL)	5 mg L^{-1}	30 mg Ag/CdS; magnetically stirred; purged with nitrogen; a 300 W Xe lamp with a 420 nm cutoff filter	Kinetics: 100% (30 min) Debromination efficiency: 44.3% Mechanism: reductive photo-debromination	261

[a] BDE209: decabromodiphenyl ether; BDE7, BDE15: dibromodiphenyl ethers; BDE30: tribromodiphenyl ether; BDE47, BDE75: tetrabromodiphenyl ethers; BDE99, BDE116: pentabromodiphenyl ethers; BDE166: hexabromodiphenyl ether; 2-CH_3-BDE61: 2-methyl-3,4,5,6-tetrabromo-diphenyl ether; DMSO: C_2H_6OS; THF: tetrahydrofuran; TEA: triethylamine.

aqueous system. Methanol was selected as a h^+ scavenger and was able to reach the surface of TiO_2 to capture photo-generated h^+. And the debromination efficiency increased with the increase of methanol content.[226]

Besides, acidity and alkalinity in a TiO_2 reaction system affect the degradation efficiency. The degradation of BDE47 and H_2 production by TiO_2–Cu_2O films under different pH conditions (3.0, 5.0, 6.8, 8.0, and 10.0) were studied by Hu *et al.*[221]

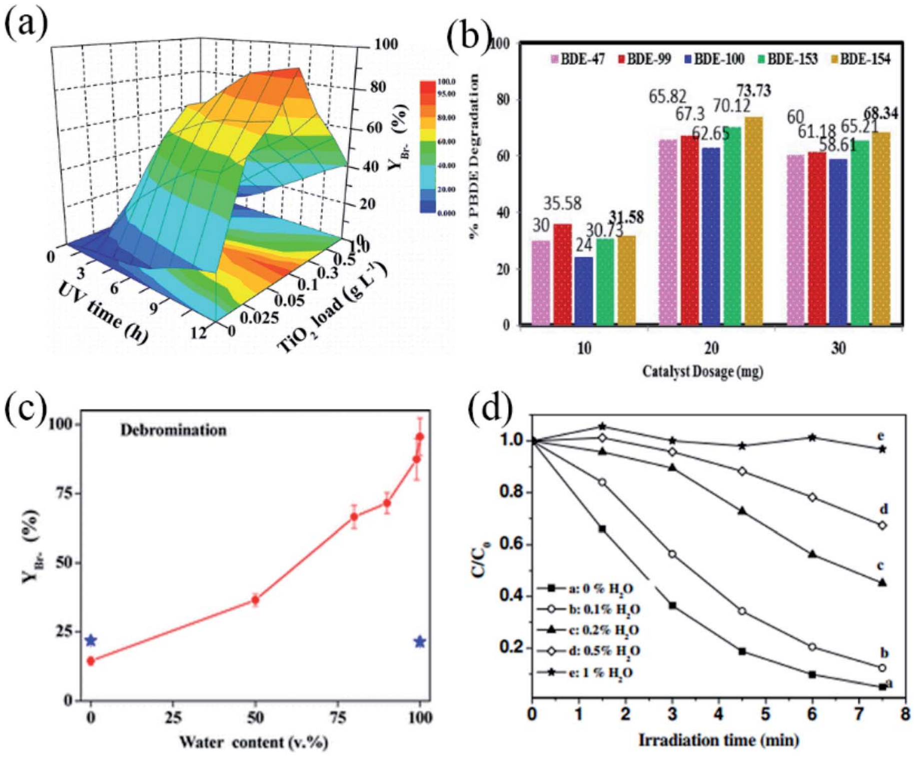

Fig. 16 (a) Effect of TiO_2 load on the debromination efficiency (Y_{Br^-}) of BDE209 in UV-irradiated aqueous dispersions under air-saturated conditions. (c) Effects of water content in water–CH_3CN mixtures on the debromination efficiency (Y_{Br^-}) of BDE209 within 12 h. Reproduced with permission from ref. 224. Copyright 2012, American Chemical Society. (b) The effect of catalyst dosages of Cu/Ni/TiO_2/PVC (5 : 10 : 85) photocatalysts on the PBDE compound photodegradation. Reproduced with permission from ref. 234. Copyright 2016, Elsevier. (d) Effects of H_2O concentration on the photocatalytic degradation kinetics of BDE209 in 40 mL of anaerobic TiO_2/acetonitrile dispersion. Reproduced with permission from ref. 227. Copyright 2009, American Chemical Society.

They found that the optimal pH value was 5.0, because at neutral pH, TiO_2 has a greater effective surface area in contact with BDE47. Azri *et al.*[234] observed the degradation of PBDEs by $Cu/Ni/TiO_2$ (5 : 10 : 85) at different pH values. The results showed that the optimal pH value was 6.8, because less $^{\bullet}OH$ was produced under acidic conditions which play an important role in degradation. The decreased degradation rate under alkaline conditions could be explained by the following reasons: (1) PBDEs are highly ionized, so their adsorption on the catalyst surface decreases, which in turn reduces the degradation efficiency; (2) excess hydroxide ions compete with Br ions for adsorption sites on the catalyst surface; (3) the negative charge on the hydroxide surface was repelled by the TiO_2 surface, preventing the formation of $^{\bullet}OH$ which was used to degrade PBDEs. $^{\bullet}OH$ for degradation was more likely to be produced in alkaline solutions, so the effect of BDE209 degradation was better at a higher pH value.[236] At the same time, TiO_2 particles with the same charge would repel each other and disperse, which would promote their contact area with BDE209. In earlier years, Sun *et al.*[227] verified the same pattern. Adding an acid or base to the TiO_2-mediated catalytic degradation system of BDE209 could inhibit or promote the degradation of BDE209. This may be due to changes in the Fermi energy level of TiO_2 particles.

Arita *et al.*[237] studied the selective decomposition of HBCD in polystyrene (PS)/HBCD, using thermal and light energy. The experimental process needed to control the cross-linking reaction between PS. Firstly, the degradation of HBCD was initiated by the TiO_2/polyethylene oxide photocatalyst. Polyethylene oxide (PEO) was first degraded by photocatalyst TiO_2 to generate $^{\bullet}OH$ and then $^{\bullet}OH$ would cause degradation of HBCD and PS. Secondly, $NO^{\bullet}$ was broken by heat treatment. Through the hybrid treatments, the degradation rate of HBCD was over 90%. Li and his co-workers[238] used three different systems (the UV/TiO_2 system, the potassium persulfate (UV/KPS) system, and the UV/TiO_2/KPS system) for degradation of HBCD. The results showed that the effect of the UV/TiO_2/KPS system on the degradation of HBCD was much stronger than that of the other two systems, in which HBCD was degraded completely due to the synergistic effect of $^{\bullet}OH$ produced by TiO_2 photocatalysis and $SO_4{}^{2-}$ produced by persulfate.

Horikoshi *et al.*[239] designed an alkaline TiO_2 solution with UV light irradiation, which could dissolve TBBPA easily. After 2 h of reaction, complete degradation of TBBPA was achieved. To improve the photocatalytic performance of TiO_2 under visible light, a lot of research has been carried out. Au nanoparticles were deposited on anatase TiO_2 nanobelts (NBs) *via* electrochemical deposition by Chen *et al.*[240] Au nanoparticles would respond in visible light due to surface plasmon resonance (Fig. 17a), which would extend the light response range of TiO_2 to the visible light region (Fig. 17b); at the same time, the Fermi level of TiO_2 NBs/Au NPs was lower than that of the TiO_2 CB, and e^- could migrate from the TiO_2 CB to Au NPs, which would inhibit the recombination of e^- and h^+. Compared with TiO_2 NBs, the TiO_2 NBs/Au NPs presented greater performance in photodegradation of TBBPA under simulated solar light and visible light irradiation as shown in Fig. 17c and d. TiO_2 exhibits good photocatalytic performance under UV light, and combining it with some materials can further enhance its photocatalytic performance. For instance, tourmaline is a complex borosilicate mineral, which has permanent and spontaneous magnetic poles capable of producing electric dipoles. The electrostatic field on the surface of tourmaline can inhibit the recombination of e^- and h^+ from TiO_2, thus improving the photocatalytic performance. Li *et al.*[241] reported that tourmaline–TiO_2 composites showed significant enhancement in the photodegradation of TBBPA. Especially, the (20%)-TiO_2 catalyst was determined to be the optimal catalyst which could completely remove TBBPA after exposure to UV light for 1 h. This result confirmed the theory mentioned above.

4.4.2 g-C_3N_4-based photocatalysts for BFR degradation. g-C_3N_4-based photocatalysts are also widely used in photocatalytic degradation of BFRs. Wei *et al.*[242] studied a g-C_3N_4 supported Ni photocatalyst for debromination of BDE47 and achieved complete debromination of BDE47. Triethylamine was used as a hydrogen source in the reaction system, and its surface coordination with Ni caused weakness in C–Br bonds, playing an important role in the high degree of debromination. Sun *et al.*[243] found that 60% of BDE209 was degraded after 20 min of UV irradiation in an anoxic g-C_3N_4/BDE209 solution and the photodegradation of BDE209 was considered as a stepwise process which was caused by CB e^- produced by the irradiated g-C_3N_4. In order to overcome the high dispersion, not conducive to multiple use, and low quantum efficiency shortcomings of g-C_3N_4, Shao and co-workers[244] chose Fe_3O_4 to construct an Fe_3O_4–g-C_3N_4 heterojunction for degradation of BDE209. That's because Fe_3O_4 nanoparticles have many excellent properties such as a matched energy band, high conductivity and easy recycling because of their magnetic separation properties. The results of the study showed that, among all the hybrids, the photocatalyst Fe_3O_4–g-C_3N_4 with 4 wt% Fe_3O_4 content showed the highest reaction rate, and its reaction rate was 6.7 times higher than that of the original g-C_3N_4. In addition, it could be easily separated and recovered under the action of an external magnetic field, and had good light stability.

4.4.3 Bi-based photocatalysts for BFR degradation. Some Bi-based materials have potential photocatalytic properties; thus they have attracted much attention. For example, Meng *et al.*[245] reported that total TBBPA could be decomposed completely by a mesoporous BiOBr catalyst after 15 min of irradiation. However, only 75% of the total TBBPA could be removed by the P25 photocatalyst under the same conditions. The excellent performance of the catalyst was because of the efficient separation of e^-–h^+ pairs and the full utilization of visible light. Guo *et al.*[246] studied the degradation of pollutants by Pt–BiOBr heterojunctions with different morphologies (Pt–BiOBr micro-flowers, microspheres, nanosheets and sphere-like micro-flowers). They found that the Pt–BiOBr microspheres were the most active photocatalyst achieving 100% removal efficiency for TBBPA under simulated sunlight irradiation for 5 min. In order to overcome some inherent defects of BiOX, some researchers have taken effective measures to degrade TBBPA such as fabricating heterojunctions based on BiOX[247] and doping bismuth oxide with halogens.[248] For instance, Gao

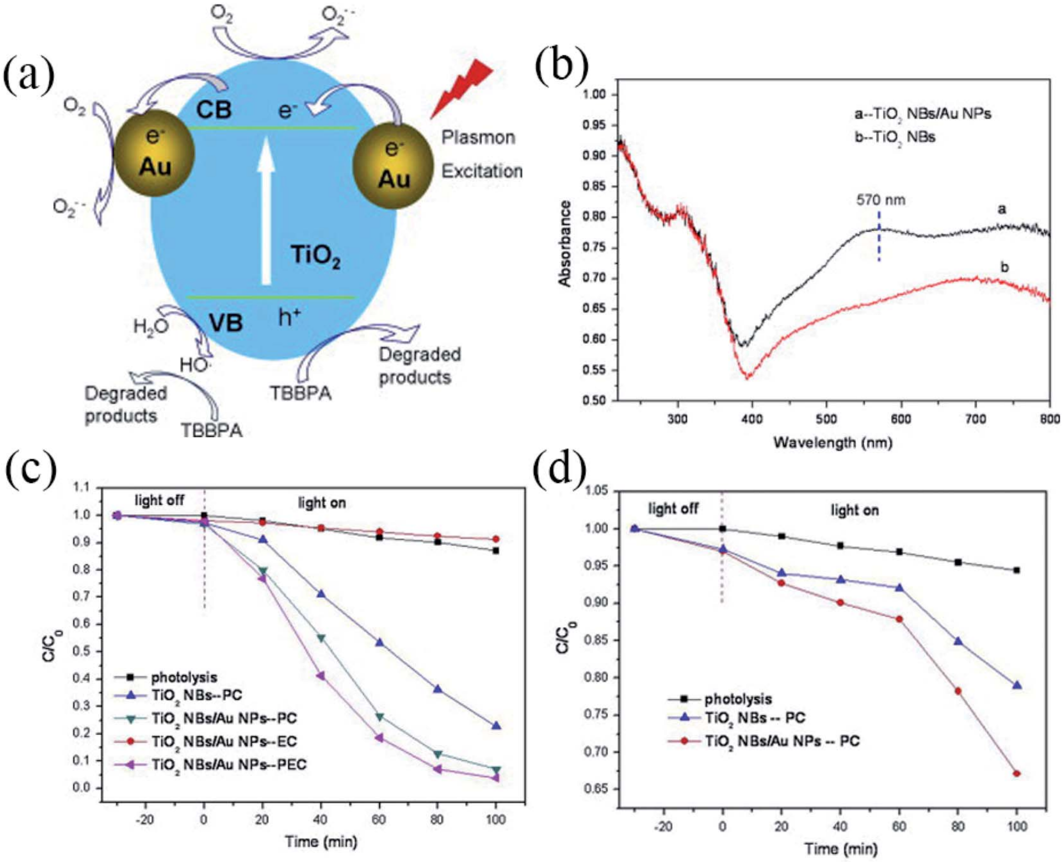

Fig. 17 (a) Schematic illustration of the proposed PC mechanism over TiO_2 NBs/Au NPs under simulated solar light irradiation, (b) UV-vis diffuse reflectance spectra of TiO_2 NBs and TiO_2 NBs/Au NPs, (c) PC and PEC degradation of TBBPA under simulated sunlight irradiation, and (d) comparative visible light ($k > 400$ nm) active PC degradation of TBBPA over TiO_2 NBs and TiO_2 NBs/Au NPs. Reproduced with permission from ref. 240. Copyright 2013, Elsevier.

et al.[247] evaluated the potential for photodegradation of TBBPA using $BiOBr/BiOI/Fe_3O_4$ nanocomposites, photocatalysts with magnetic separation properties and a unique heterostructure, and a schematic illustration of the proposed degradation mechanism is shown in Fig. 18b. The experimental results showed that $BiOBr/BiOI/Fe_3O_4$ (2 : 2 : 0.5) had the best photocatalytic performance (Fig. 18c). It could remove 98.5% TBBPA (Fig. 18d) within 1.5 h under irradiation. Qin *et al.*[248] demonstrated that a flower-like $BiOCl_{1-x}Br_x$ hierarchical microsphere photocatalyst could photodegrade and mineralize TBBPA efficiently. In addition, some other Bi containing materials are also used in the composite photocatalyst to degrade TBBPA. Zhu *et al.*[249] found that zero dimensional Bi_3TaO_7 nanoparticles loaded on N,C co-doped TiO_2 (B/VNT) performed better than the pristine components in the degradation of TBBPA. The 10% B/VNT could degrade 69.9% of TBBPA within 80 min. The mechanism diagram is shown in Fig. 18a. The reasons for this phenomenon could be summarized as follows: (1) doping N and C would narrow the band gap of TiO_2, which would enhance the absorption of light, thereby promoting the generation of photogenerated e^- and h^+; (2) compared with the original component, 10% B/VNT had a larger surface area, which could promote the adsorption of pollutants on it; (3) the built-in electric field formed between the Bi_3TaO_7 and $V/N–TiO_2$ interface resulted in the formation of a Z-type structure, which promoted the separation of $e^-–h^+$ pairs and thus improved photocatalytic performance. Guo *et al.*[250] observed that the $Ag/Bi_5Nb_3O_{15}$ heterostructured material could effectively degrade and mineralize TBBPA. The excellent photocatalytic activity of $Ag/Bi_5Nb_3O_{15}$ could be attributed to the synergistic effect of the layered structure of $Bi_5Nb_3O_{15}$, photoresponse in both UV and visible light region of $Ag/Bi_5Nb_3O_{15}$, and the electron trapping ability of metallic Ag particles.

4.4.4 Other photocatalysts for BFR degradation. Graphene oxide (GO) has many excellent properties, such as strong light absorption, high specific surface area, excellent electrical conductivity, and chemical stability. It has been proven to promote the separation and migration of charge pairs efficiently.[251,252] Many GO/Ag_3PO_4 composites with different GO contents for degradation of BDE209 were prepared by Chen *et al.*[253] Under the conditions of anoxic H_2O using CH_3OH as the e^- donor, when irradiated with visible light for 8 h, 97.33% of BDE209 was degraded by the GO/Ag_3PO_4 photocatalyst containing 7% GO content. GO could not only promote the transfer of e^- generated on the CB of Ag_3PO_4 to BDE209 molecules, but also protected Ag_3PO_4 from photo-corrosion. Liang *et al.*[254]

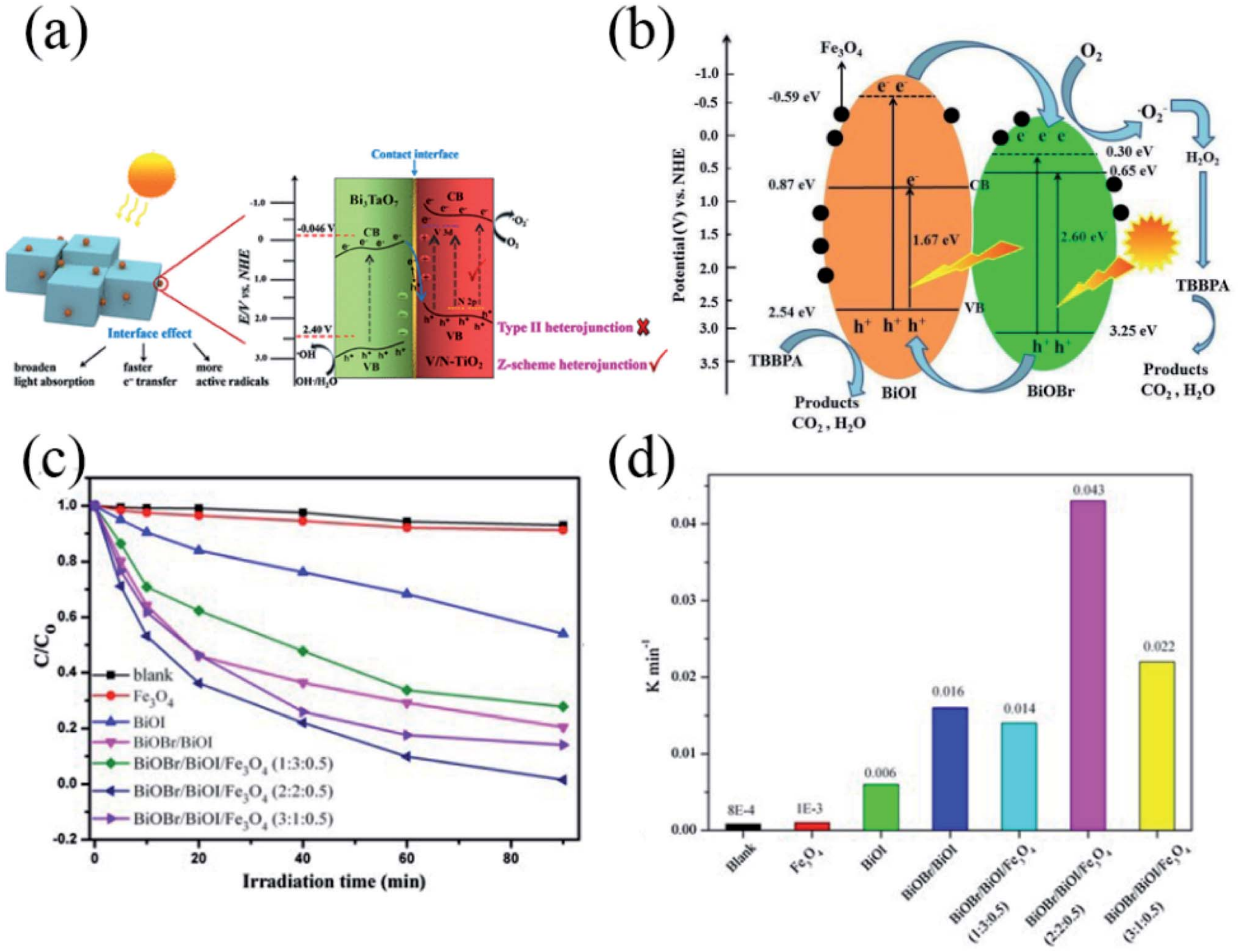

Fig. 18 (a) Schematic diagram of the photoinduced electron–hole separation process for the 10% B/VNT Z-scheme heterojunction. Reproduced with permission from ref. 249. Copyright 2019, American Chemical Society. (b) Schematic illustration of the proposed photocatalytic degradation mechanism of TBBPA over BiOBr/BiOI/Fe_3O_4 under visible light irradiation (>420 nm), and the removal ratio (c) and rate constant (d) of TBBPA degradation over different samples under visible light irradiation. Reproduced with permission from ref. 247. Copyright 2017, Elsevier.

prepared a Ag@Ag_3PO_4/g-C_3N_4/rGO composite, which formed a Z-scheme system (Fig. 19a), for BDE47 removal. Rapid e^- transfer and cleavage of C–Br bonds played important roles in the degradation; the e^- accumulated on the catalyst surface were transferred to the BDE47 molecule, which was subsequently converted to BDE28, which then underwent a continuous process of debromination (Fig. 19b). Within 2 h under visible light ($\lambda > 420$ nm) irradiation, through catalytic reduction debromination, the removal rate of BDE47 over Ag@Ag_3PO_4/g-C_3N_4/rGO was 173.65 times higher than that of the original g-C_3N_4 (Fig. 19c). And the removal efficiency of BDE47 reached 93.4% (Fig. 19d). The remaining e^- could reduce the protons (H^+) to hydrogen atoms (H°). H° could convert BDE47 to BDE17 because of steric hindrance. Besides, photogenerated h^+ could react with CH_3OH to convert it into a $^\bullet CH_2OH$ radical, which was capable of injecting e^- into the catalyst for the debromination reaction. Graphene is a unique two-dimensional material, which has excellent electrical conductivity, effectively promotes electron migration, and has achieved large-scale production, and it is widely used in environment and energy applications.[255] Su *et al.*[256] prepared a macro-porous silicon/graphene heterostructure by deposition of graphene sheets on the surface of MPSi (macroporous silicon) by electrophoresis. It was used for photoelectrocatalytic and photocatalytic processes for debromination of BDE47 under visible light irradiation. This MPSi/Gr heterostructure showed better debromination effects compared to MPSi, mainly due to the following points: (1) graphene sheets protected silicon from corrosion; (2) graphene sheets had a wide range of light responses and could effectively promote the separation of photo-generated carriers.

Tang *et al.*[257] used an ultrasonication-assisted route to prepare CoO@graphene nanocomposites. Investigations showed that 73.4% of TBBPA was removed under visible light irradiation due to the well-dispersed CoO on the surface of graphene nanosheets, and increased crystallization led to strong light absorption and narrowed band gap energy.

In addition, graphene and GO have some other applications in the degradation of TBBPA. For example, Ag_3PO_4 has excellent

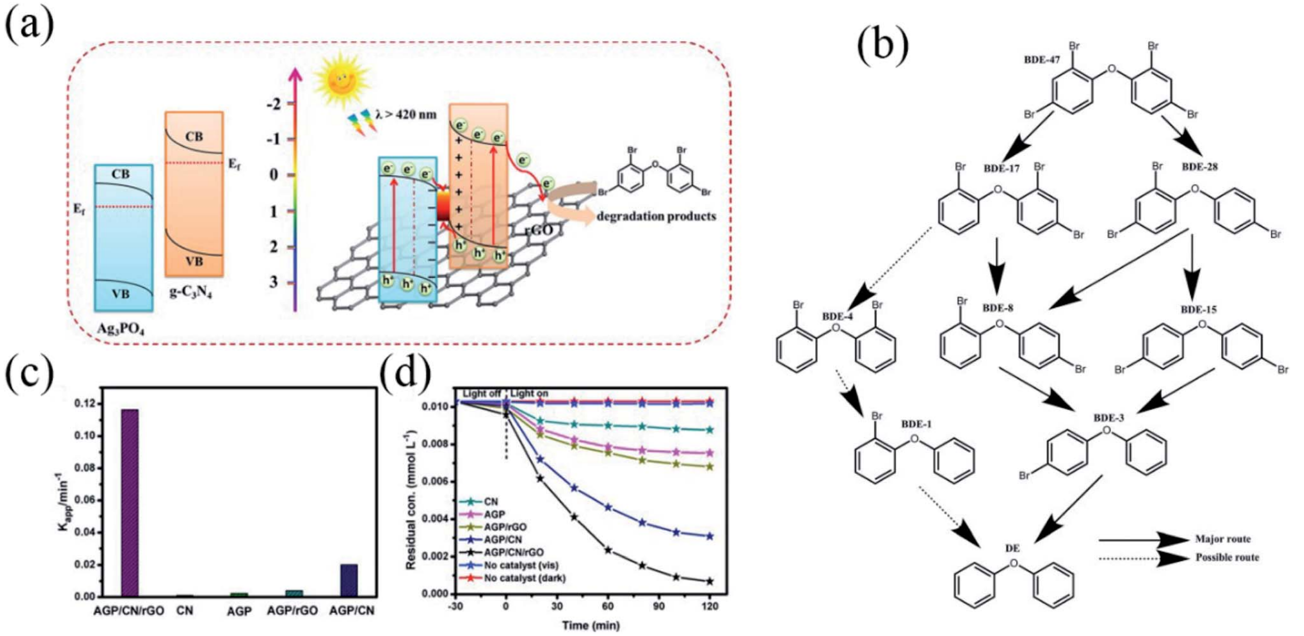

Fig. 19 (a) Possible charge pair transfer model for the Z-scheme system with enhanced photocatalytic performance over the Ag@Ag_3PO_4/g-C_3N_4/rGO composite, (b) pathway of debromination of BDE47 in the photocatalytic system, (c) corresponding rate constants (K_{app}) of AGP/CN/rGO, CN, AGP, AGP/rGO and AGP/CN composites, and (d) photo-removal of BDE47 over the as-prepared composites under visible light irradiation. Reproduced with permission from ref. 254. Copyright 2018, Elsevier.

performance in photocatalysis, but its stability is reduced by long-term light irradiation. Zhang *et al.*[258] verified that by integrating GO with Ag_3PO_4, Ag_3PO_4 showed improved performance in terms of visible light absorption, separation efficiency and lifetime of e^-–h^+ pairs. And the Ag_3PO_4/GO composite could completely decompose TBBPA within 1 h under illumination. Cao and co-workers[259] prepared a graphene-based photocatalyst with magnetic separation performance, which was composed of graphene, Fe_3O_4 and TiO_2. After being exposed to UV light for 1 h, the removal rate of TBBPA over the photocatalyst containing 3% graphene was more than 99%, which was much better than that over naked TiO_2. In this study, the function of graphene could be summarized as follows: (1) flaked graphene could make TiO_2 particles disperse evenly, preventing their agglomeration to avoid the degradation of photocatalytic performance; (2) the large surface area of graphene was conducive to full contact with TiO_2 particles, which increased the catalytically active sites, thus improving catalytic performance; (3) as a good electron acceptor, graphene could transfer the photogenerated electrons produced on TiO_2 particles to graphene rapidly, which could inhibit the recombination of e^- and h^+.

In addition to the photocatalysts mentioned above, there are other photocatalysts used for the degradation of PBDEs. Miller *et al.*[260] synthesized Cu_2O crystals with their surface modified by Pb nanoparticles *via* a hydrothermal method for the degradation of BDE47. The initial quasi first order rate constant reached 0.21 h^{-1}, which indicated that Cu_2O@Pd could achieve a high-efficiency debromination of BDE47. Wang and team members[261] studied the application of a Ag-loaded CdS photocatalyst in the debromination of BDE47, and found that BDE47 could be completely removed, and the efficiency of debromination reached 44.3% within 0.5 h under irradiation with visible light. In photocatalytic degradation of BDE209, Jiang and co-workers[262] found that BDE209 could be debrominated effectively by pyruvic acid under UV light. In the anoxic solution, 60% of BDE209 was removed after 1 h of irradiation.

5 Conclusions and perspectives

As a result of modernization, plastics have already caused global environmental problems. Additives in plastic are being released into the environment causing harm to ecosystems. In particular, regarding the emerging MPs and NPs, it is a huge challenge to remove them from the environment. One of the important aspects of MPs and NPs is their ability to transmit environmental contaminants. There is still a lot of room for understanding the fate, risks and transportation of MPs and NPs that are ubiquitous in the environment. Many questions need to be answered such as the following. How can we formulate a clear definition of MPs and NPs that is uniform within the literature? How do MPs and NPs interact with other emerging contaminants? How can we improve existing methods or explore new techniques to push the detection towards the nanoscale?

Investigations have confirmed that it is feasible to use photocatalytic technology to degrade polymeric materials. In general, there are relatively few studies on photocatalytic degradation of plastic fragments. In the most typical experiments, $TiO_2|Pt$, CdS/CdO_x and $CN_x|Ni_2P$ photocatalysts were used. Although the degradation of plastics is accompanied by the generation of H_2 energy, photocatalysts like $TiO_2|Pt$ can only absorb UV light and are relatively expensive, and CdS/CdO_x quantum dots are a toxic photocatalyst. Since UV light only accounts for about 4% of the total energy of sunlight, it is necessary to design photocatalysts driven by visible light and non-toxicity for transforming plastics into a variety of organic chemicals and clean H_2 fuel. Plastic is a valuable material which contains chemical feedstocks and stored energy, but it loses most of its potential due to landfill or other improper operation methods. These mentioned photocatalytic studies have opened the way for the degradation of plastics in the future, and we can further explore how to achieve more efficient photodegradation of plastics while generating energy.

In general, photocatalysis has great potential in degrading plastic-derived chemicals. However, for chemicals like BPA and PAEs, the degradation processes are achieved in multiple steps, and some by-products or intermediates formed in the process of degrading plastic-derived chemicals may be more toxic than the parent compounds. Thus, attention should also be paid to assessing the human toxicity or eco-toxicity of these intermediate and final degradation products. Various high-level characterization methods must be used to accurately analyze the catalytic reactions to ensure that the degradation intermediates or by-products are less toxic than the parent. For example, the X-ray absorption near-edge structure (XANES) can be used to investigate the strains and defect materials. X-ray photoelectron spectroscopy (XPS) using a synchrotron light source is a powerful tool to inspect the photoinduced carrier transfer. Electron spin resonance (ESR) is a suitable method for the detection of active free radicals on the surface of photocatalysts. *In situ* FTIR is a useful tool for exploring the reaction pathways and surface intermediates. Besides, due to the difference between the laboratory environment and the actual wastewater, in order to realize the challenge in the practical wastewater application, the experimental environment should be replaced by actual wastewater. So far, many photocatalysts such as TiO_2, g-C_3N_4, *etc.* have been used in the degradation of plastic-derived chemicals. How to effectively control the textural/surface properties and the band gap structure of these photocatalysts should be taken seriously. Efforts must be made to expand the light absorption range to take full advantage of the solar spectrum. In order to improve photocatalysts' efficiencies, more investigations should be conducted on enhancing the utilization of sunlight, tuning the morphology, improving the separation of photogenerated electron–hole pairs, *etc.* For example, incorporating lanthanide-based molecules into photocatalysts expands the light absorption range from visible light to NIR light, and constructing a Z-type system can promote the separation of photogenerated carriers, and enhance the lifetime of photogenerated carriers. Moreover, new theoretical calculation and characterization methods are expected to guide the design of better photocatalytic systems. Further understanding the mechanism of photocatalytic degradation of plastic-derived chemicals and the basic calculations and simulations will help in designing more excellent photocatalysts.

Current studies almost entirely focus on several common plastic-derived chemicals. For instance, regarding brominated flame retardants, only HBCD, TBBPA and a few PBDEs are discussed in this study. There are many other flame retardants that are subject to expanded use, whose degradation needs to be studied, as well as some alternatives to common BFRs, such as deca-bromodiphenyl ethane (DBDPE), which is a substitute for deca-BDE, and other emerging BFRs such as hexabromobenzene and 1,2-bis(2,4,6-tribromophenoxy)ethane, which have been identified in food, humans, organisms and many environmental compartments. In conclusion, photocatalytic degradation technology can be applied to more types of plastic-derived chemical in the future.

In summary, the degradation of plastics and plastic-derived chemicals by employing photocatalysts and solar radiation as the energy input will be a promising technology. What can be determined is that progress in the synthesis and modification methods for the photocatalysts coupled with a more in-depth understanding of photodegradation mechanisms will enable the rational design of photocatalysts with excellent activity. However, at present, the investigations are only in the experimental stage, and there are still great challenges in their application in the actual environment. We are confident that continuous optimization of photocatalysts, improvement of characterization technology, and deepening of photocatalytic degradation mechanisms can provide a bright future to photocatalytic degradation of plastics and plastic-derived chemicals.

Conflicts of interest

There are no conflicts to declare.

Acknowledgements

This study was financially supported by the Program for the National Natural Science Foundation of China (51809090), the Natural Science Foundation of Hunan Province, China (Grant No. 2019JJ50077), and the Fundamental Research Funds for the Central Universities (531118010114).

References

1 PlasticsEurope, *Plastics – the facts 2019: an analysis of European plastics production, demand and waste data*, 2020.
2 S. Lambert and M. Wagner, *Chem. Soc. Rev.*, 2017, **46**, 6855–6871.
3 O. S. Alimi, J. F. Budarz, L. M. Hernandez and N. Tufenkji, *Environ. Sci. Technol.*, 2018, **52**, 1704–1724.
4 J. N. Hahladakis, C. A. Velis, R. Weber, E. Iacovidou and P. Purnell, *J. Hazard. Mater.*, 2018, **344**, 179–199.
5 J. Y. Li, H. H. Liu and J. P. Chen, *Water Res.*, 2018, **137**, 362–374.
6 W. C. Li, H. F. Tse and L. Fok, *Sci. Total Environ.*, 2016, **566**, 333–349.
7 S. B. Borrelle, J. Ringma, K. L. Law, C. C. Monnahan, L. Lebreton, A. McGivern, E. Murphy, J. Jambeck,

G. H. Leonard, M. A. Hilleary, M. Eriksen, H. P. Possingham, H. De Frond, L. R. Gerber, B. Polidoro, A. Tahir, M. Bernard, N. Mallos, M. Barnes and C. M. Rochman, *Science*, 2020, **369**, 1515–1518.

8 F. Wang, C. S. Wong, D. Chen, X. Lu, F. Wang and E. Y. Zeng, *Water Res.*, 2018, **139**, 208–219.

9 B. Worm, H. K. Lotze, I. Jubinville, C. Wilcox and J. Jambeck, *Annu. Rev. Environ. Resour.*, 2017, **42**, 1–26.

10 X. Jiao, K. Zheng, Q. Chen, X. Li, Y. Li, W. Shao, J. Xu, J. Zhu, Y. Pan, Y. Sun and Y. Xie, *Angew. Chem., Int. Ed.*, 2020, **59**, 15497–15501.

11 M. O. Rodrigues, N. Abrantes, F. J. M. Goncalves, H. Nogueira, J. C. Marques and A. M. M. Goncalves, *Sci. Total Environ.*, 2018, **633**, 1549–1559.

12 V. Hidalgo-Ruz, L. Gutow, R. C. Thompson and M. Thiel, *Environ. Sci. Technol.*, 2012, **46**, 3060–3075.

13 L. Nizzetto, G. Bussi, M. N. Futter, D. Butterfield and P. G. Whitehead, *Environ. Sci.: Processes Impacts*, 2016, **18**, 1050–1059.

14 J. M. Panko, J. Chu, M. L. Kreider and K. M. Unice, *Atmos. Environ.*, 2013, **72**, 192–199.

15 J. P. da Costa, P. S. M. Santos, A. C. Duarte and T. Rocha-Santos, *Sci. Total Environ.*, 2016, **566**, 15–26.

16 I. Peeken, S. Primpke, B. Beyer, J. Guetermann, C. Katlein, T. Krumpen, M. Bergmann, L. Hehemann and G. Gerdts, *Nat. Commun.*, 2018, **9**, 1505.

17 C. Munari, V. Infantini, M. Scoponi, E. Rastelli, C. Corinaldesi and M. Mistri, *Mar. Pollut. Bull.*, 2017, **122**, 161–165.

18 M. Oliveira and M. Almeida, *TrAC, Trends Anal. Chem.*, 2019, **114**, 196–201.

19 J. M. Garcia and M. L. Robertson, *Science*, 2017, **358**, 870–872.

20 R. J. Wright, G. Erni-Cassola, V. Zadjelovic, M. Latva and J. A. Christie-Oleza, *Environ. Sci. Technol.*, 2020, **54**, 11657–11672.

21 M. C. M. Blettler, E. Abrial, F. R. Khan, N. Sivri and L. A. Espinola, *Water Res.*, 2018, **143**, 416–424.

22 S. Frehland, R. Kaegi, R. Hufenus and D. M. Mitrano, *Water Res.*, 2020, **182**, 115860.

23 C.-B. Jeong, H.-M. Kang, Y. H. Lee, M.-S. Kim, J.-S. Lee, J. S. Seo, M. Wang and J.-S. Lee, *Environ. Sci. Technol.*, 2018, **52**, 11411–11418.

24 H. Hirai, H. Takada, Y. Ogata, R. Yamashita, K. Mizukawa, M. Saha, C. Kwan, C. Moore, H. Gray, D. Laursen, E. R. Zettler, J. W. Farrington, C. M. Reddy, E. E. Peacock and M. W. Ward, *Mar. Pollut. Bull.*, 2011, **62**, 1683–1692.

25 A. A. Horton, A. Walton, D. J. Spurgeon, E. Lahive and C. Svendsen, *Sci. Total Environ.*, 2017, **586**, 127–141.

26 C. Zhang, W. Wang, A. Duan, G. Zeng, D. Huang, C. Lai, X. Tan, M. Cheng, R. Wang, C. Zhou, W. Xiong and Y. Yang, *Chemosphere*, 2019, **222**, 184–194.

27 C. Zhang, G. Zeng, D. Huang, C. Lai, M. Chen, M. Cheng, W. Tang, L. Tang, H. Dong, B. Huang, X. Tan and R. Wang, *Chem. Eng. J.*, 2019, **373**, 902–922.

28 T. S. Tofa, K. L. Kunjali, S. Paul and J. Dutta, *Environ. Chem. Lett.*, 2019, **17**, 1341–1346.

29 T. S. Tofa, F. Ye, K. L. Kunjali and J. Dutta, *Catalysts*, 2019, **9**, 819.

30 A. Fujishima and K. Honda, *Nature*, 1972, **238**, 37–38.

31 G. Zhang, G. Liu, L. Wang and J. T. S. Irvine, *Chem. Soc. Rev.*, 2016, **45**, 5951–5984.

32 D. He, C. Zhang, G. Zeng, Y. Yang, D. Huang, L. Wang and H. Wang, *Appl. Catal., B*, 2019, **258**, 117957.

33 Y. Zhou, W. Wang, C. Zhang, D. Huang, C. Lai, M. Cheng, L. Qin, Y. Yang, C. Zhou, B. Li, H. Luo and D. He, *Adv. Colloid Interface Sci.*, 2020, **279**, 102144.

34 S. Tian, C. Zhang, D. Huang, R. Wang, G. Zeng, M. Yan, W. Xiong, C. Zhou, M. Cheng, W. Xue, Y. Yang and W. Wang, *Chem. Eng. J.*, 2020, **389**, 123423.

35 W. Wang, Z. Zeng, G. Zeng, C. Zhang, R. Xiao, C. Zhou, W. Xiong, Y. Yang, L. Lei, Y. Liu, D. Huang, M. Cheng, Y. Yang, Y. Fu, H. Luo and Y. Zhou, *Chem. Eng. J.*, 2019, **378**, 122132.

36 W. Wang, Q. Niu, G. Zeng, C. Zhang, D. Huang, B. Shao, C. Zhou, Y. Yang, Y. Liu, H. Guo, W. Xiong, L. Lei, S. Liu, H. Yi, S. Chen and X. Tang, *Appl. Catal., B*, 2020, **273**, 119051.

37 W. Wang, Q. Niu, G. Zeng, C. Zhang, D. Huang, B. Shao, C. Zhou, Y. Yang, Y. Liu, H. Guo, W. Xiong, L. Lei, S. Liu, H. Yi, S. Chen and X. Tang, *Appl. Catal., B*, 2020, **273**, 119051.

38 H. Luo, Z. Zeng, G. Zeng, C. Zhang, R. Xiao, D. Huang, C. Lai, M. Cheng, W. Wang, W. Xiong, Y. Yang, L. Qin, C. Zhou, H. Wang, Y. Zhou and S. Tian, *Chem. Eng. J.*, 2020, **383**, 123196.

39 R. Gusain, K. Gupta, P. Joshi and O. P. Khatri, *Adv. Colloid Interface Sci.*, 2019, **272**, 102009.

40 C. Zhang, C. Lai, G. Zeng, D. Huang, C. Yang, Y. Wang, Y. Zhou and M. Cheng, *Water Res.*, 2016, **95**, 103–112.

41 D. Qin, Y. Zhou, W. Wang, C. Zhang, G. Zeng, D. Huang, L. Wang, H. Wang, Y. Yang, L. Lei, S. Chen and D. He, *J. Mater. Chem. A*, 2020, **8**, 19156–19195.

42 C. Zhang, Y. Zhou, W. Wang, Y. Yang, C. Zhou, L. Wang, L. Lei, D. He, H. Luo and D. Huang, *Appl. Surf. Sci.*, 2020, **527**, 146757.

43 Y. Yang, X. Li, C. Zhou, W. Xiong, G. Zeng, D. Huang, C. Zhang, W. Wang, B. Song, X. Tang, X. Li and H. Guo, *Water Res.*, 2020, **184**, 116200.

44 P. V. L. Reddy, K. H. Kim, B. Kavitha, V. Kumar, N. Raza and S. Kalagara, *J. Environ. Manage.*, 2018, **213**, 189–205.

45 L. Hermabessiere, A. Dehaut, I. Paul-Pont, C. Lacroix, R. Jezequel, P. Soudant and G. Duflos, *Chemosphere*, 2017, **182**, 781–793.

46 M. Oliveira, M. Almeida and I. Miguel, *TrAC, Trends Anal. Chem.*, 2019, **112**, 196–200.

47 C. M. Rochman, S. M. Kross, J. B. Armstrong, M. T. Bogan, E. S. Darling, S. J. Green, A. R. Smyth and D. Veríssimo, *Environ. Sci. Technol.*, 2015, **49**, 10759–10761.

48 R. Lehner, C. Weder, A. Petri-Fink and B. Rothen-Rutishauser, *Environ. Sci. Technol.*, 2019, **53**, 1748–1765.

49 Y. Y. Tsang, C. W. Mak, C. Liebich, S. W. Lam, E. T. P. Sze and K. M. Chan, *Mar. Pollut. Bull.*, 2017, **115**, 20–28.

50 M. Eriksen, L. C. M. Lebreton, H. S. Carson, M. Thiel, C. J. Moore, J. C. Borerro, F. Galgani, P. G. Ryan and J. Reisser, *PLoS One*, 2014, **9**, e111913.

51 P. Liu, L. Qian, H. Wang, X. Zhan, K. Lu, C. Gu and S. Gao, *Environ. Sci. Technol.*, 2019, **53**, 3579–3588.

52 P. G. Ryan, R. S. Shomura and M. H. Godfrey, *Proceedings of the Second International Conference on Marine Debris U S Department of Commerce*, 1990, pp. 623–634.

53 S. C. Gall and R. C. Thompson, *Mar. Pollut. Bull.*, 2015, **92**, 170–179.

54 C. Wilcox, G. Heathcote, J. Goldberg, R. Gunn, D. Peel and B. D. Hardesty, *Conserv. Biol.*, 2015, **29**, 198–206.

55 P. G. J. E. P. Ryan, *Environ. Pollut.*, 1987, **46**, 119–125.

56 C. M. Rochman, E. Hoh, T. Kurobe and S. J. Teh, *Sci. Rep.*, 2013, **3**, 3263.

57 B. K. Dau, K. V. Gilardi, F. M. Gulland, A. Higgins, J. B. Holcomb, J. S. Leger and M. H. Ziccardi, *J. Wildl. Dis.*, 2009, **45**, 355–362.

58 J. P. Winn, B. L. Woodward, M. J. Moore, M. L. Peterson and J. G. Riley, *Mar. Mammal Sci.*, 2008, **24**, 326–340.

59 B. L. Woodward, J. P. Winn, M. J. Moore and M. L. Peterson, *Mar. Mammal Sci.*, 2006, **22**, 299–310.

60 G. M. Vélez-Rubio, A. Estrades, A. Fallabrino and J. Tomás, *Mar. Biol.*, 2013, **160**, 2797–2811.

61 E. Moore, S. Lyday, J. Roletto, K. Litle, J. K. Parrish, H. Nevins, J. Harvey, J. Mortenson, D. Greig and M. Piazza, *Mar. Pollut. Bull.*, 2009, **58**, 1045–1051.

62 T. P. Good, J. A. June, M. A. Etnier and G. Broadhurst, *Mar. Pollut. Bull.*, 2010, **60**, 39–50.

63 S. I. Rothstein, *Condor*, 1973, **75**, 344–345.

64 R. H. Day, D. H. S. Wehle and F. Coleman, *Proceedings of the Workshop on the Fate and Impact of Marine Debris*, 1985, pp. 344–386.

65 S. Avery-Gomm, J. Provencher, K. Morgan and D. Bertram, *Mar. Pollut. Bull.*, 2013, **72**, 257–259.

66 Q. Schuyler, B. D. Hardesty, C. Wilcox and K. Townsend, *Conserv. Biol.*, 2014, **28**, 129–139.

67 S. da Silva Mendes, R. H. de Carvalho, A. F. de Faria and B. M. de Sousa, *Mar. Pollut. Bull.*, 2015, **92**, 8–10.

68 R. S. Shomura and H. O. Yoshida, *Proceedings of the Workshop on the Fate and Impact of Marine Debris, 27–29 November 1984*, University of North Texas Libraries, UNT Digital Library, Honolulu, Hawaii, 1985.

69 M. C. Fossi, C. Peda, M. Compa, C. Tsangaris, C. Alomar, F. Claro, C. Ioakeimidis, F. Galgani, T. Hema and S. Deudero, *Environ. Pollut.*, 2018, **237**, 1023–1040.

70 C. Wilcox, E. Van Sebille and B. D. Hardesty, *Proc. Natl. Acad. Sci. U. S. A.*, 2015, **112**, 11899–11904.

71 J. N. Möller, M. G. Löder and C. Laforsch, *Environ. Sci. Technol.*, 2020, **54**, 2078–2090.

72 L.-J. Feng, X.-D. Sun, F.-P. Zhu, Y. Feng, J.-L. Duan, F. Xiao, X.-Y. Li, Y. Shi, Q. Wang and J.-W. Sun, *Environ. Sci. Technol.*, 2020, **54**, 3386–3394.

73 Z. Sobhani, X. Zhang, C. Gibson, R. Naidu, M. Mallavarapu and C. Fang, *Water Res.*, 2020, **174**, 115658.

74 N. B. Hartmann, T. Hüffer, R. C. Thompson, M. Hassellöv, A. Verschoor, A. E. Daugaard, S. Rist, T. Karlsson, N. Brennholt, M. Cole, M. P. Herrling, M. C. Hess, N. P. Ivleva, A. L. Lusher and M. Wagner, *Environ. Sci. Technol.*, 2019, **53**, 1039–1047.

75 E. J. Carpenter and K. L. Smith, *Science*, 1972, **175**, 1240–1241.

76 J. Boucher and D. Friot, *Primary Microplastics in the Oceans: A Global Evaluation of Sources*, 2017.

77 L. Nizzetto, M. Futter and S. Langaas, *Environ. Sci. Technol.*, 2016, **50**, 10777–10779.

78 L. M. Heidbreder, I. Bablok, S. Drews and C. Menzel, *Sci. Total Environ.*, 2019, **668**, 1077–1093.

79 K. Betts, *Environ. Sci. Technol.*, 2008, **42**, 8995.

80 C. J. Moore, *Environ. Res.*, 2008, **108**, 131–139.

81 M. M. Patel, B. R. Goyal, S. V. Bhadada, J. S. Bhatt and A. F. Amin, *CNS Drugs*, 2009, **23**, 35–58.

82 V. Zitko and M. Hanlon, *Mar. Pollut. Bull.*, 1991, **22**, 41–42.

83 S. A. Carr, J. Liu and A. G. Tesoro, *Water Res.*, 2016, **91**, 174–182.

84 F. Murphy, C. Ewins, F. Carbonnier and B. Quinn, *Environ. Sci. Technol.*, 2016, **50**, 5800–5808.

85 D. K. Barnes, F. Galgani, R. C. Thompson and M. Barlaz, *Philos. Trans. R. Soc., B*, 2009, **364**, 1985–1998.

86 H. Nishihara and T. Kyotani, *Adv. Mater.*, 2012, **24**, 4473–4498.

87 N. Panwar, A. M. Soehartono, K. K. Chan, S. Zeng, G. Xu, J. Qu, P. Coquet, K.-T. Yong and X. Chen, *Chem. Rev.*, 2019, **119**, 9559–9656.

88 Y. Fu, G. Zeng, C. Lai, D. Huang, L. Qin, H. Yi, X. Liu, M. Zhang, B. Li, S. Liu, L. Li, M. Li, W. Wang, Y. Zhang and Z. Pi, *Chem. Eng. J.*, 2020, **399**, 125743.

89 F. Qin, Y. Peng, G. Song, Q. Fang, R. Wang, C. Zhang, G. Zeng, D. Huang, C. Lai, Y. Zhou, X. Tan, M. Cheng and S. Liu, *J. Hazard. Mater.*, 2020, **398**, 122816.

90 K. Mattsson, E. V. Johnson, A. Malmendal, S. Linse, L. A. Hansson and T. Cedervall, *Sci. Rep.*, 2017, **7**, 11452.

91 Y. F. Lu, Y. Zhang, Y. F. Deng, W. Jiang, Y. P. Zhao, J. J. Geng, L. L. Ding and H. Q. Ren, *Environ. Sci. Technol.*, 2016, **50**, 4054–4060.

92 C. Della Torre, E. Bergami, A. Salvati, C. Faleri, P. Cirino, K. A. Dawson and I. Corsi, *Environ. Sci. Technol.*, 2014, **48**, 12302–12311.

93 K. W. Lee, W. J. Shim, O. Y. Kwon and J. H. Kang, *Environ. Sci. Technol.*, 2013, **47**, 11278–11283.

94 I. Inkielewicz-Stepniak, L. Tajber, G. Behan, H. Z. Zhang, M. W. Radomski, C. Medina and M. J. Santos-Martinez, *Materials*, 2018, **11**, 724.

95 L. M. Hernandez, E. G. Xu, H. C. E. Larsson, R. Tahara, V. B. Maisuria and N. Tufenkji, *Environ. Sci. Technol.*, 2019, **53**, 12300–12310.

96 J. Gasperi, S. L. Wright, R. Dris, F. Collard, C. Mandin, M. Guerrouache, V. Langlois, F. J. Kelly and B. Tassin, *Curr. Opin. Environ. Sci. Health*, 2018, **1**, 1–5.

97 S. L. Wright and F. J. Kelly, *Environ. Sci. Technol.*, 2017, **51**, 6634–6647.

98 A. Vogt, B. Combadiere, S. Hadam, K. M. Stieler, J. Lademann, H. Schaefer, B. Autran, W. Sterry and U. Blume-Peytavi, *J. Invest. Dermatol.*, 2006, **126**, 1316–1322.

99 D. Lithner, A. Larsson and G. Dave, *Sci. Total Environ.*, 2011, **409**, 3309–3324.
100 M. Shen, Y. Zhang, Y. Zhu, B. Song, G. Zeng, D. Hu, X. Wen and X. Ren, *Environ. Pollut.*, 2019, **252**, 511–521.
101 E. Fasano, F. Bono-Blay, T. Cirillo, P. Montuori and S. Lacorte, *Food Control*, 2012, **27**, 132–138.
102 S. Cui, G. Shan and L. Zhu, *Appl. Catal., B*, 2017, **219**, 249–258.
103 F. Wang, K. M. Shih and X. Y. Li, *Chemosphere*, 2015, **119**, 841–847.
104 D. Brennecke, B. Duarte, F. Paiva, I. Cacador and J. Canning-Clode, *Estuarine, Coastal Shelf Sci.*, 2016, **178**, 189–195.
105 H. Lee, W. J. Shim and J.-H. Kwon, *Sci. Total Environ.*, 2014, **470**, 1545–1552.
106 C. Zarfl and M. Matthies, *Mar. Pollut. Bull.*, 2010, **60**, 1810–1814.
107 K. Mizukawa, H. Takada, M. Ito, Y. B. Geok, J. Hosoda, R. Yamashita, M. Saha, S. Suzuki, C. Miguez, J. Frias, J. C. Antunes, P. Sobral, I. Santos, C. Micaelo and A. M. Ferreira, *Mar. Pollut. Bull.*, 2013, **70**, 296–302.
108 Y. Ogata, H. Takada, K. Mizukawa, H. Hirai, S. Iwasa, S. Endo, Y. Mato, M. Saha, K. Okuda, A. Nakashima, M. Murakami, N. Zurcher, R. Booyatumanondo, M. P. Zakaria, L. Q. Dung, M. Gordon, C. Miguez, S. Suzuki, C. Moore, H. K. Karapanagioti, S. Weerts, T. McClurg, E. Burres, W. Smith, M. Van Velkenburg, J. S. Lang, R. C. Lang, D. Laursen, B. Danner, N. Stewardson and R. C. Thompson, *Mar. Pollut. Bull.*, 2009, **58**, 1437–1446.
109 M. C. Ariza-Tarazona, J. F. Villarreal-Chiu, J. M. Hernandez-Lopez, J. R. De la Rosa, V. Barbieri, C. Siligardi and E. I. Cedillo-Gonzalez, *J. Hazard. Mater.*, 2020, **395**, 122632.
110 W. Li, A. Elzatahry, D. Aldhayan and D. Zhao, *Chem. Soc. Rev.*, 2018, **47**, 8203–8237.
111 M. C. Ariza-Tarazona, J. F. Villarreal-Chiu, V. Barbieri, C. Siligardi and E. I. Cedillo-González, *Ceram. Int.*, 2019, **45**, 9618–9624.
112 W. R. L. N. Bandara, R. M. de Silva, K. M. N. de Silva, D. Dahanayake, S. Gunasekara and K. Thanabalasingam, *RSC Adv.*, 2017, **7**, 46155–46163.
113 T. Uekert, M. F. Kuehnel, D. W. Wakerley and E. Reisner, *Energy Environ. Sci.*, 2018, **11**, 2853–2857.
114 T. Kawai and T. Sakata, *Chem. Lett.*, 1981, **10**, 81–84.
115 T. Uekert, H. Kasap and E. Reisner, *J. Am. Chem. Soc.*, 2019, **141**, 15201–15210.
116 Y. Li, S. Wan, C. Lin, Y. Gao, Y. Lu, L. Wang and K. Zhang, *Sol. RRL*, 2020, 2000427.
117 C. Venkataramana, S. M. Botsa, P. Shyamala and R. Muralikrishna, *Chemosphere*, 2021, **265**, 129021.
118 R. Jiang, G. Lu, Z. Yan, J. Liu, D. Wu and Y. Wang, *J. Hazard. Mater.*, 2021, **405**, 124247.
119 Y. Yang, G. Zeng, D. Huang, C. Zhang, D. He, C. Zhou, W. Wang, W. Xiong, B. Song, H. Yi, S. Ye and X. Ren, *Small*, 2020, **16**, 2001634.
120 Y. Yang, X. Li, C. Zhou, W. Xiong, G. Zeng, D. Huang, C. Zhang, W. Wang, B. Song, X. Tang, X. Li and H. Guo, *Water Res.*, 2020, **184**, 116200.
121 Y. Yang, G. M. Zeng, D. L. Huang, C. Zhang, D. H. He, C. Y. Zhou, W. J. Wang, W. P. Xiong, X. P. Li, B. S. Li, W. Y. Dong and Y. Zhou, *Appl. Catal., B*, 2020, **272**, 118970.
122 J. Rivera-Utrilla, R. Ocampo-Pérez, J. D. Méndez-Díaz and M. Sánchez-Polo, *J. Environ. Manage.*, 2012, **109**, 164–178.
123 S. Net, R. Sempéré, A. Delmont, A. Paluselli and B. Ouddane, *Environ. Sci. Technol.*, 2015, **49**, 4019–4035.
124 S. Anandan, N. Pugazhenthiran, T. Lana-Villarreal, G.-J. Lee and J. Wu, *Chem. Eng. J.*, 2013, **231**, 182–189.
125 L. Jiang, X. Yuan, Y. Pan, J. Liang, G. Zeng, Z. Wu and H. Wang, *Appl. Catal., B*, 2017, **217**, 388–406.
126 C. Zhang, C. Lai, G. Zeng, D. Huang, L. Tang, C. Yang, Y. Zhou, L. Qin and M. Cheng, *Biosens. Bioelectron.*, 2016, **81**, 61–67.
127 X.-K. Wang, C. Wang, W.-Q. Jiang, W.-L. Guo and J.-G. Wang, *Chem. Eng. J.*, 2012, **189**, 288–294.
128 Y.-C. Nie, F. Yu, L.-C. Wang, Q.-J. Xing, X. Liu, Y. Pei, J.-P. Zou, W.-L. Dai, Y. Li and S. L. Suib, *Appl. Catal., B*, 2018, **227**, 312–321.
129 F. Ma, S. Zhang, X. Yang, W. Guo, Y. Guo and M. Huo, *Catal. Commun.*, 2012, **24**, 75–79.
130 G. He, J. Zhang, Y. Hu, Z. Bai and C. Wei, *Appl. Catal., B*, 2019, **250**, 301–312.
131 T. Ma, Y. Kimura, D. Tadaki, A. Hirano-Iwata and M. Niwano, *J. Electrochem. Soc.*, 2019, **166**, H842–H848.
132 K. Li, L. Yan, Z. Zeng, S. Luo, X. Luo, X. Liu, H. Guo and Y. Guo, *Appl. Catal., B*, 2014, **156**, 141–152.
133 L. Xu, X. Yang, Y. Guo, F. Ma, Y. Guo, X. Yuan and M. Huo, *J. Hazard. Mater.*, 2010, **178**, 1070–1077.
134 K. Li, X. Yang, Y. Guo, F. Ma, H. Li, L. Chen and Y. Guo, *Appl. Catal., B*, 2010, **99**, 364–375.
135 R. E. Engler, *Environ. Sci. Technol.*, 2012, **46**, 12302–12315.
136 Z. Noorimotlagh, I. Kazeminezhad, N. Jaafarzadeh, M. Ahmadi, Z. Ramezani and S. S. Martinez, *J. Hazard. Mater.*, 2018, **350**, 108–120.
137 C. Tang, X. Huang, H. Wang, H. Shi and G. Zhao, *J. Hazard. Mater.*, 2020, **382**, 121017.
138 K. Inumaru, M. Murashima, T. Kasahara and S. Yamanaka, *Appl. Catal., B*, 2004, **52**, 275–280.
139 S.-i. Naya, T. Nikawa, K. Kimura and H. Tada, *ACS Catal.*, 2013, **3**, 903–907.
140 F. Ye, H. Li, H. Yu, S. Chen and X. Quan, *Appl. Catal., B*, 2018, **227**, 258–265.
141 A. Babaei, A. Mesdaghiniai, N. J. Haghighi, R. Nabizadeh and A. Mahvi, *J. Hazard. Mater.*, 2011, **185**, 1273–1279.
142 O. Bechambi, W. Najjar and S. Sayadi, *J. Taiwan Inst. Chem. Eng.*, 2016, **60**, 496–501.
143 D. D. Seachrist, K. W. Bonk, S.-M. Ho, G. S. Prins, A. M. Soto and R. A. Keri, *Reprod. Toxicol.*, 2016, **59**, 167–182.
144 J. Im and F. E. Löffler, *Environ. Sci. Technol.*, 2016, **50**, 8403–8416.
145 S. Yüksel, N. Kabay and M. Yüksel, *J. Hazard. Mater.*, 2013, **263**, 307–310.

146 M. Zielińska, K. Bułkowska, A. Cydzik-Kwiatkowska, K. Bernat and I. Wojnowska-Baryła, *Int. J. Environ. Sci. Technol.*, 2016, **13**, 2239–2248.

147 S. Yang, F. I. Hai, L. D. Nghiem, L. N. Nguyen, F. Roddick and W. E. Price, *Int. Biodeterior. Biodegrad.*, 2013, **85**, 483–490.

148 M. Umar, F. Roddick, L. Fan and H. A. Aziz, *Chemosphere*, 2013, **90**, 2197–2207.

149 S. Q. Zhou, L. Li, Y. T. Wu, S. M. Zhu, N. Y. Zhu, L. J. Bu and D. D. Dionysiou, *Water Res.*, 2020, **178**, 115829.

150 T. Garoma, S. Matsumoto, Y. Wu and R. Klinger, *Ozone: Sci. Eng.*, 2010, **32**, 338–343.

151 A. Dupuis, V. Migeot, A. Cariot, M. Albouy-Llaty, B. Legube and S. Rabouan, *Environ. Sci. Pollut. Res.*, 2012, **19**, 4193–4205.

152 R. He, D. Xu, B. Cheng, J. Yu and W. Ho, *Nanoscale Horiz.*, 2018, **3**, 464–504.

153 S. Cao, P. Zhou and J. Yu, *Chin. J. Catal.*, 2014, **35**, 989–1007.

154 C. Yu, Z. Wu, R. Liu, D. D. Dionysiou, K. Yang, C. Wang and H. Liu, *Appl. Catal., B*, 2017, **209**, 1–11.

155 Y. Kanigaridou, A. Petala, Z. Frontistis, M. Antonopoulou, M. Solakidou, I. Konstantinou, Y. Deligiannakis, D. Mantzavinos and D. I. Kondarides, *Chem. Eng. J.*, 2017, **318**, 39–49.

156 L. Yu, X. Zhang, G. Li, Y. Cao, Y. Shao and D. Li, *Appl. Catal., B*, 2016, **187**, 301–309.

157 J. Li, X. Wu, Z. Wan, H. Chen and G. Zhang, *Appl. Catal., B*, 2019, **243**, 667–677.

158 Y. Zhang, L. Wang, F. Dong, Q. Chen, H. Jiang, M. Xu and J. Shi, *J. Colloid Interface Sci.*, 2019, **536**, 575–585.

159 M. Sun, S. Li, T. Yan, P. Ji, X. Zhao, K. Yuan, D. Wei and B. Du, *J. Hazard. Mater.*, 2017, **333**, 169–178.

160 X. Jin, L. Ye, H. Xie and G. Chen, *Coord. Chem. Rev.*, 2017, **349**, 84–101.

161 S. Luo, J. Xu, Z. Li, C. Liu, J. Chen, X. Min, M. Fang and Z. Huang, *Nanoscale*, 2017, **9**, 15484–15493.

162 S.-q. Guo, X.-h. Zhu, H.-j. Zhang, B.-c. Gu, W. Chen, L. Liu and P. J. J. Alvarez, *Environ. Sci. Technol.*, 2018, **52**, 6872–6880.

163 A. Kubacka, M. Fernandez-Garcia and G. Colon, *Chem. Rev.*, 2012, **112**, 1555–1614.

164 X.-J. Wen, C.-G. Niu, L. Zhang, C. Liang and G.-M. Zeng, *J. Catal.*, 2017, **356**, 283–299.

165 W. Li, S.-a. He, Z.-y. Su, W. Xu and X.-c. Wang, *Appl. Surf. Sci.*, 2019, **470**, 707–715.

166 Q. Hu, M. Ji, J. Di, B. Wang, J. Xia, Y. Zhao and H. Li, *J. Colloid Interface Sci.*, 2018, **519**, 263–272.

167 S. Gao, C. Guo, J. Lv, Q. Wang, Y. Zhang, S. Hou, J. Gao and J. Xu, *Chem. Eng. J.*, 2017, **307**, 1055–1065.

168 H. Huang, K. Xiao, T. Zhang, F. Dong and Y. Zhang, *Appl. Catal., B*, 2017, **203**, 879–888.

169 G. Wu, Y. Zhao, Y. Li, H. Ma and J. Zhao, *J. Colloid Interface Sci.*, 2018, **510**, 228–236.

170 C.-Y. Wang, X. Zhang, H.-B. Qiu, W.-K. Wang, G.-X. Huang, J. Jiang and H.-Q. Yu, *Appl. Catal., B*, 2017, **200**, 659–665.

171 R. Li, J. Liu, X. Zhang, Y. Wang, Y. Wang, C. Zhang, X. Zhang and C. Fan, *Chem. Eng. J.*, 2018, **339**, 42–50.

172 X. Liu, X. Xiong, S. Ding, Q. Jiang and J. Hu, *Catal. Sci. Technol.*, 2017, **7**, 3580–3590.

173 Z. Yi, J. Ye, N. Kikugawa, T. Kako, S. Ouyang, H. Stuart-Williams, H. Yang, J. Cao, W. Luo, Z. Li, Y. Liu and R. L. Withers, *Nat. Mater.*, 2010, **9**, 559–564.

174 X. Li, P. Xu, M. Chen, G. Zeng, D. Wang, F. Chen, W. Tang, C. Chen, C. Zhang and X. Tan, *Chem. Eng. J.*, 2019, **366**, 339–357.

175 T. Li, H. Wei, H. Jia, T. Xia, X. Guo, T. Wang and L. Zhu, *ACS Sustainable Chem. Eng.*, 2019, **7**, 4177–4185.

176 H. Guo, C.-G. Niu, X.-J. Wen, L. Zhang, C. Liang, X.-G. Zhang, D.-L. Guan, N. Tang and G.-M. Zeng, *J. Colloid Interface Sci.*, 2018, **513**, 852–865.

177 L. Liu, P. Hu, Y. Li, W. An, J. Lu and W. Cui, *Appl. Surf. Sci.*, 2019, **466**, 928–936.

178 C. Mu, Y. Zhang, W. Cui, Y. Liang and Y. Zhu, *Appl. Catal., B*, 2017, **212**, 41–49.

179 F. Chen, J. Zhao, W. An, J. Hu, Y. Liang and W. Cui, *RSC Adv.*, 2017, **7**, 39814–39823.

180 F. Chen, W. An, L. Liu, Y. Liang and W. Cui, *Appl. Catal., B*, 2017, **217**, 65–80.

181 J. Mei, D. Zhang, N. Li, M. Zhang, X. Gu, S. Miao, S. Cui and J. Yang, *J. Alloys Compd.*, 2018, **749**, 715–723.

182 M. Sun, Q. Zeng, X. Zhao, Y. Shao, P. Ji, C. Wang, T. Yan and B. Du, *J. Hazard. Mater.*, 2017, **339**, 9–21.

183 Y. Chen, P. Zhu, M. Duan, J. Li, Z. Ren and P. Wang, *Appl. Surf. Sci.*, 2019, **486**, 198–211.

184 S.-F. Yang, C.-G. Niu, D.-W. Huang, H. Zhang, C. Lianga and G.-M. Zeng, *Environ. Sci.: Nano*, 2017, **4**, 585–595.

185 F. Chen, H. Huang, C. Zeng, X. Du and Y. Zhang, *ACS Sustainable Chem. Eng.*, 2017, **5**, 7777–7791.

186 L. Zhang, Z. Wang, C. Hu and B. Shi, *J. Colloid Interface Sci.*, 2019, **553**, 598–605.

187 L. Pan, S. Cao, R. Liu, H. Chen, F. Jiang and X. Wang, *J. Colloid Interface Sci.*, 2019, **548**, 284–292.

188 Y. Chen, P. Wang, Y. Liang, M. Zhao, Y. Jiang, G. Wang, P. Zou, J. Zeng, Y. Zhang and Y. Wang, *J. Colloid Interface Sci.*, 2019, **536**, 389–398.

189 G. Mamba and A. K. Mishra, *Appl. Catal., B*, 2016, **198**, 347–377.

190 X.-H. Jiang, L.-C. Wang, F. Yu, Y.-C. Nie, Q.-J. Xing, X. Liu, Y. Pei, J.-P. Zou and W.-L. Dai, *ACS Sustainable Chem. Eng.*, 2018, **6**, 12695–12705.

191 Y. Wu, H. Wang, W. Tu, S. Wu, Y. Liu, Y. Z. Tan, H. Luo, X. Yuan and J. W. Chew, *Appl. Catal., B*, 2018, **229**, 181–191.

192 Y. Wang, H. Cai, F. Qian, Y. Li, J. Yu, X. Yang, M. Bao and X. Li, *J. Colloid Interface Sci.*, 2019, **533**, 47–58.

193 P. Qiu, C. Xu, H. Chen, F. Jiang, X. Wang, R. Lu and X. Zhang, *Appl. Catal., B*, 2017, **206**, 319–327.

194 J. Gu, H. Chen, F. Jiang and X. Wang, *J. Colloid Interface Sci.*, 2019, **540**, 97–106.

195 B. Liu, M. Qiao, Y. Wang, L. Wang, Y. Gong, T. Guo and X. Zhao, *Chemosphere*, 2017, **189**, 115–122.

196 Y. Li, Y. Fang, Z. Cao, N. Li, D. Chen, Q. Xu and J. Lu, *Appl. Catal., B*, 2019, **250**, 150–162.

197 Y. Gong, X. Zhao, H. Zhang, B. Yang, K. Xiao, T. Guo, J. Zhang, H. Shao, Y. Wang and G. Yu, *Appl. Catal., B*, 2018, **233**, 35–45.

198 C.-Y. Wang, Y.-J. Zhang, W.-K. Wang, D.-N. Pei, G.-X. Huang, J.-J. Chen, X. Zhang and H.-Q. Yu, *Appl. Catal., B*, 2018, **221**, 320–328.

199 J. Yang, D. Zheng, X. Xiao, X. Wu, X. Zuo and J. Nan, *Chem. Eng. J.*, 2019, **373**, 935–945.

200 M. Ji, J. Xia, J. Di, Y. Liu, R. Chen, Z. Chen, S. Yin and H. Li, *Chem. Eng. J.*, 2018, **331**, 355–363.

201 C. Zeng, Y. Hu and H. Huang, *ACS Sustainable Chem. Eng.*, 2017, **5**, 3897–3905.

202 J. Guo, Y.-z. Dai, X.-j. Chen, L.-l. Zhou and T.-h. Liu, *J. Alloys Compd.*, 2017, **696**, 226–233.

203 H. Guo, H.-Y. Niu, C. Liang, C.-G. Niu, D.-W. Huang, L. Zhang, N. Tang, Y. Yang, C.-Y. Feng and G.-M. Zeng, *J. Catal.*, 2019, **370**, 289–303.

204 L. Ju, P. Wu, Q. Yang, Z. Ahmed and N. Zhu, *Appl. Catal., B*, 2018, **224**, 159–174.

205 Y. Wang, X. Zhao, D. Cao, Y. Wang and Y. Zhu, *Appl. Catal., B*, 2017, **211**, 79–88.

206 S. Zhang, Y. Liu, P. Gu, R. Ma, T. Wen, G. Zhao, L. Li, Y. Ai, C. Hu and X. Wang, *Appl. Catal., B*, 2019, **248**, 1–10.

207 W.-D. Oh, L.-W. Lok, A. Veksha, A. Giannis and T.-T. Lim, *Chem. Eng. J.*, 2018, **333**, 739–749.

208 R. Ma, S. Zhang, L. Li, P. Gu, T. Wen, A. Khan, S. Li, B. Li, S. Wang and X. Wang, *ACS Sustainable Chem. Eng.*, 2019, **7**, 9699–9708.

209 X. Li, M. Cui, Y. Lee, J. Choi and J. Khim, *RSC Adv.*, 2019, **9**, 22153–22160.

210 E. M. Chua, J. Shimeta, D. Nugegoda, P. D. Morrison and B. O. Clarke, *Environ. Sci. Technol.*, 2014, **48**, 8127–8134.

211 M. Taheran, S. Komtchou, L. Lonappan, T. Najia, S. K. Brar, M. Cledon and P. Drogui, *Crit. Rev. Environ. Sci. Technol.*, 2017, **47**, 1107–1142.

212 G. Sheng, Y. Shao, W. Ye, C. Sun, C. Chen, J. C. Crittenden and C. Liu, *ACS Sustainable Chem. Eng.*, 2018, **6**, 6711–6717.

213 D. Zhou, Y. Wu, X. Feng, Y. Chen, Z. Wang, T. Tao and D. Wei, *Environ. Sci. Pollut. Res.*, 2014, **21**, 6228–6233.

214 D. Li, P. a. Peng, Z. Yu, W. Huang and Y. Zhong, *Water Res.*, 2016, **101**, 195–202.

215 L. Huang, S. B. Shah, H. Hu, P. Xu and H. Tang, *Front. Environ. Sci. Eng.*, 2020, **14**, 11.

216 X. Hou, M. Yu, A. Liu, Y. Li, T. Ruan, J. Liu, J. L. Schnoor and G. Jiang, *Environ. Pollut.*, 2018, **241**, 331–338.

217 W. Zhang, A. Li, Y. Pan, F. Wang, M. Li, Y. Liang, X. Yao, J. Song, M. Song and G. Jiang, *J. Hazard. Mater.*, 2021, **407**, 124859.

218 R. Wang, T. Tang, Y. Wei, D. Dang, K. Huang, X. Chen, H. Yin, X. Tao, Z. Lin, Z. Dang and G. Lu, *Environ. Int.*, 2019, **127**, 5–12.

219 M. Lei, N. Wang, S. Guo, L. Zhu, Y. Ding and H. Tang, *Chem. Eng. J.*, 2018, **345**, 586–593.

220 M. Lei, N. Wang, L. Zhu, Q. Zhou, G. Nie and H. Tang, *Appl. Catal., B*, 2016, **182**, 414–423.

221 Z. Hu, X. Wang, H. Dong, S. Li, X. Li and L. Li, *J. Hazard. Mater.*, 2017, **340**, 1–15.

222 M. Lei, N. Wang, L. Zhu and H. Tang, *Chemosphere*, 2016, **150**, 536–544.

223 M. Yan, G. Zeng, X. Li, C. Zhao, G. Yang, J. Gong, G. Chen, L. Tang and D. Huang, *New J. Chem.*, 2017, **41**, 4377–4389.

224 A. Huang, N. Wang, M. Lei, L. Zhu, Y. Zhang, Z. Lin, D. Yin and H. Tang, *Environ. Sci. Technol.*, 2013, **47**, 518–525.

225 M. Zhang, J. Lu, Y. He and P. C. Wilson, *Front. Environ. Sci. Eng.*, 2016, **10**, 229–235.

226 C. Sun, J. Zhao, H. Ji, W. Ma and C. Chen, *Chemosphere*, 2012, **89**, 420–425.

227 C. Sun, D. Zhao, C. Chen, W. Ma and J. Zhao, *Environ. Sci. Technol.*, 2009, **43**, 157–162.

228 Y. Lv, X. Cao, H. Jiang, W. Song, C. Chen and J. Zhao, *Appl. Catal., B*, 2016, **194**, 150–156.

229 S. Guo, L. Zhu, T. Majima, M. Lei and H. Tang, *Environ. Sci. Technol.*, 2019, **53**, 4433–4439.

230 Y.-Y. Shao, W.-D. Ye, C.-Y. Sun, C.-L. Liu and Q. Wang, *RSC Adv.*, 2017, **7**, 39089–39095.

231 L. Li, W. Chang, Y. Wang, H. Ji, C. Chen, W. Ma and J. Zhao, *Chem.–Eur. J.*, 2014, **20**, 11163–11170.

232 U. I. Gaya and A. H. Abdullah, *J. Photochem. Photobiol., C*, 2008, **9**, 1–12.

233 J. He, C. Lai, L. Qin, B. Li, S. Liu, L. Jiao, Y. Fu, D. Huang, L. Li, M. Zhang, X. Liu, H. Yi, L. Chen and Z. Li, *Chemosphere*, 2020, **256**, 127083.

234 N. Azri, W. Azelee, W. Abu Bakar and R. Ali, *J. Taiwan Inst. Chem. Eng.*, 2016, **62**, 283–296.

235 M. Lei, N. Wang, L. Zhu, C. Xie and H. Tang, *Chem. Eng. J.*, 2014, **241**, 207–215.

236 K. L. Chow, Y. B. Man, J. S. Zheng, Y. Liang, N. F. Y. Tam and M. H. Wong, *J. Environ. Sci.*, 2012, **24**, 1670–1678.

237 S. Arita, K. Yamaguchi, S. Motokucho and H. Nakatani, *Polym. Degrad. Stab.*, 2017, **143**, 130–135.

238 Q. Li, L. Wang, X. Fang, L. Zhang, J. Li and H. Xie, *Catalysts*, 2019, **9**, 189.

239 S. Horikoshi, T. Miura, M. Kajitani, N. Horikoshi and N. Serpone, *Appl. Catal., B*, 2008, **84**, 797–802.

240 Q. Chen, H. Liu, Y. Xin and X. Cheng, *Chem. Eng. J.*, 2014, **241**, 145–154.

241 N. Li, J. Zhang, C. Wang and H. Sun, *J. Mater. Sci.*, 2017, **52**, 6937–6949.

242 Y. Wei, Y. Gong, X. Zhao, Y. Wang, R. Duan, C. Chen, W. Song and J. Zhao, *Environ. Sci.: Nano*, 2019, **6**, 1585–1593.

243 C. Sun, C. Chen, W. Ma and J. Zhao, *Sci. China: Chem.*, 2012, **55**, 2532–2536.

244 Y.-Y. Shao, W.-D. Ye, C.-Y. Sun, C.-L. Liu, Q. Wang, C.-C. Chen, J.-Y. Gu and X.-Q. Chen, *RSC Adv.*, 2018, **8**, 10914–10921.

245 J. Xu, W. Meng, Y. Zhang, L. Li and C. Guo, *Appl. Catal., B*, 2011, **107**, 355–362.

246 W. Guo, Q. Qin, L. Geng, D. Wang, Y. Guo and Y. Yang, *J. Hazard. Mater.*, 2016, **308**, 374–385.

247 S. Gao, C. Guo, S. Hou, L. Wan, Q. Wang, J. Lv, Y. Zhang, J. Gao, W. Meng and J. Xu, *J. Hazard. Mater.*, 2017, **331**, 1–12.

248 Q. Qin, Y. Guo, D. Zhou, Y. Yang and Y. Guo, *Appl. Surf. Sci.*, 2016, **390**, 765–777.

249 C. Zhu, Y. Wang, Z. Jiang, A. Liu, Y. Pu, Q. Xian, W. Zou and C. Sun, *ACS Appl. Mater. Interfaces*, 2019, **11**, 13011–13021.

250 Y. Guo, L. Chen, F. Ma, S. Zhang, Y. Yang, X. Yuan and Y. Guo, *J. Hazard. Mater.*, 2011, **189**, 614–618.

251 G. Luo, X. Jiang, M. Li, Q. Shen, L. Zhang and H. Yu, *ACS Appl. Mater. Interfaces*, 2013, **5**, 2161–2168.

252 C. N. R. Rao, A. K. Sood, K. S. Subrahmanyam and A. Govindaraj, *Angew. Chem., Int. Ed.*, 2009, **48**, 7752–7777.

253 W. Chen, X. Niu and J. Wang, *J. Photochem. Photobiol., A*, 2018, **356**, 304–311.

254 C. Liang, L. Zhang, H. Guo, C.-G. Niu, X.-J. Wen, N. Tang, H.-Y. Liu, Y.-Y. Yang, B.-B. Shao and G.-M. Zeng, *Chem. Eng. J.*, 2019, **361**, 373–386.

255 Q. Xiang, J. Yu and M. Jaroniec, *Chem. Soc. Rev.*, 2012, **41**, 782–796.

256 J. Su, H. Yu, S. Chen, X. Quan and Q. Zhao, *Sep. Purif. Technol.*, 2012, **96**, 154–160.

257 Y. Tang, L. Dong, S. Mao, H. Gu, T. Malkoske and B. Chen, *ACS Appl. Energy Mater.*, 2018, **1**, 2698–2708.

258 X. Zhang, H. Zhang, Y. Xiang, S. Hao, Y. Zhang, R. Guo, X. Cheng, M. Xie, Q. Cheng and B. Li, *J. Hazard. Mater.*, 2018, **342**, 353–363.

259 M. Cao, P. Wang, Y. Ao, C. Wang, J. Hou and J. Qian, *Chem. Eng. J.*, 2015, **264**, 113–124.

260 E. B. Miller, E. M. Zahran, M. R. Knecht and L. G. Bachas, *Appl. Catal., B*, 2017, **213**, 147–154.

261 X. Wang, Z. Hu, K. Chen, H. Dong, S. Li, X. Li and L. Li, *Chemosphere*, 2019, **220**, 723–730.

262 Z. Jiang, W. Linghu, Y. Li and C. Sun, *Catal. Today*, 2014, **224**, 89–93.